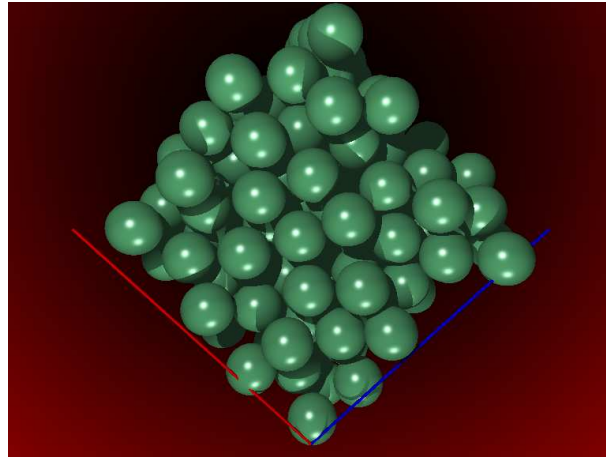


Brownian dynamics analysis of dense dispersions under shear



Dissertation

zur Erlangung des akademischen Grades des
Doktors der Naturwissenschaften (Dr.rer.nat.)
an der Universität Konstanz, im Fachbereich Physik,
am Lehrstuhl Prof. Dr. Matthias Fuchs,

vorgelegt von Erik Lange.

Tag der mündlichen Prüfung: 12. Februar 2009.

Referenten:

Prof. Dr. Matthias Fuchs,
Prof. Dr. Antonio Manuel Puertas.

Acknowledgements

Matthias Fuchs,
my colleagues in Konstanz,
Cristiano de Michele,
Antonio Puertas,
and many more that helped me
so much or
just that little bit:

thank you all,
... these have been good years.

Contents

Abstract	ii
Acknowledgements	iii
Contents	vi
Symbols — a brief guide	vii
1 Introduction	1
1.1 The problem of Brownian motion	1
1.2 Outline of chapters	2
2 Theoretical background	3
2.0.1 The Langevin description of a free particle	3
2.1 Algorithms for Brownian motion of hard spheres	6
2.1.1 Dealing with collisions	7
2.1.2 Finding a collision	10
2.1.3 The event-tree	11
2.1.4 Neighbour cells	13
2.2 The standard system	14
2.2.1 Into high densities	15
2.2.2 Avoiding crystallisation — the binary system	15
2.2.3 Numerical limits and overlaps	16
3 Soft spots of hard spheres	19
3.1 Simulation details	20
3.1.1 Soft spheres	21
3.2 Comparing soft and hard spheres	22
3.2.1 Mapping different potentials	22
3.2.2 Local structure	23
3.2.3 Dynamics	26
3.2.4 Forces and viscosity	29
3.3 Conclusions	32
4 Analytic methods to mine the data	33
4.1 Probing the structure	33
4.1.1 Radial distribution function	33
4.1.2 Static structure factor	35

4.2	Time dependent quantities	37
4.2.1	Mean squared displacement	37
4.2.2	Density-density correlation function	38
4.3	Brownian motion of hard spheres revisited	40
4.4	The stress tensor	41
4.4.1	Calculating potential forces for hard spheres	43
4.4.2	Potential forces under Brownian motion	45
4.4.3	Stress-stress correlation function	46
4.4.4	The limit $t \rightarrow 0$ of $C_{\sigma\sigma}$ for Brownian dynamics	47
4.5	Transport coefficients: The viscosity	48
4.5.1	Einstein relation for correlation functions	49
4.5.2	The limit $t \rightarrow 0$ of $C_{\sigma\sigma}$ for Newtonian dynamics	52
5	Dense colloidal systems under shear	55
5.1	Shear in the Langevin equation	55
5.2	Computational implications	57
5.2.1	Lees-Edwards boundary conditions	57
5.2.2	From snapshots to the real world	58
5.2.3	Structure factor under Lees-Edwards boundary conditions	60
5.2.4	Density-density correlation function under shear	61
5.3	Steady state	62
5.3.1	Switch on and waiting time	62
5.4	Anisotropy of the radial distribution function	63
5.4.1	Projection onto spherical harmonics	63
5.4.2	Comparing viscosities	68
5.5	Viscosity versus Peclet number	70
5.6	Towards the glass transition	73
5.7	Open questions	80
6	Conclusions	81
6.1	Zusammenfassung in Deutscher Sprache	83
	Bibliography	85

Brief guide to symbols

$\dot{\gamma}$	Shear rate in dimensions of inverse time.
η_0	Viscosity due to solvent given as $\frac{k_B T}{3\pi D_0 \sigma}$.
$g_{\dot{\gamma}}$	Distorted pair distribution function.
$\langle \dots \rangle$	Ensemble average over initial conditions.
ϕ	Packing fraction defined as $\frac{4}{3}\pi r^3 \frac{N}{L^3} = \frac{\pi \sigma^3}{6} \rho$.
ρ	Pure number density without any mass, that is $\frac{N}{L^3}$.
σ	Particle diameter, typically $\sigma = 1$.
σ_{xy}	Stress tensor, in particular the xy -component.
τ	Dimensionless parameter of time defined through $\tau \equiv t / \left(\sigma \sqrt{\frac{m}{3k_B T}} \right)$.
τ_B	Brownian time step defines the frequency of Brownian events.
$\hat{\mathbf{x}}$	Unit vector along the x-axis.
\mathbf{f}_s	Stochastic force in the Langevin equation.
ζ	Friction coefficient — has dimensions of inverse time only.
$C_{\rho\rho}$	Density-density correlation function.
$C_{\sigma\sigma}$	Stress-stress correlation function.
D	Diffusion coefficient — in general the long time diffusion coefficient.
D_0	Short time diffusion coefficient.
L	Assuming the simulation box is a cube, this is the side length.
N	Total number of particles.
P_e	Peclet number, dimensionless, relating shear and diffusion: $P_e = \frac{\dot{\gamma} \sigma^2}{4D_0}$.
r_{jk}	Relative position $r_{jk} = r_j - r_k$.
$v_{\dot{\gamma}}$	Shear velocity incurred by one box length: $v_{\dot{\gamma}} \equiv L \dot{\gamma}$.

... extremely minute particles of solid matter, whether obtained from organic or inorganic substances, when suspended in pure water, or in some other aqueous fluids, exhibit motions for which I am unable to account ...

Robert Brown



Introduction

1.1 The problem of Brownian motion

In the summer months of the year 1827, Robert Brown observed under his microscope pollen grains moving erratically in water. He referred to them as *active* molecules, which expresses tacitly what was the first line of investigation: namely, that the causes for such *activity* were to be sought inside the particles — not the solvent. He was careful, though, not to imply anything about them being alive.

Neither was the Scottish botanist Brown the first to observe or describe this phenomenon, nor did he really manage to explain it. Nevertheless, he was the first to investigate it carefully and publish about it [9]. Henceforth his name was connected with stochastic movement of microscale particles suspended in aqueous fluids — in fact, this type of random movement came to be known as *Brownian* motion.

The significance of Brownian motion is due to its unique position right at the interface between the macroscopic world of thermodynamics and the — then unknown — bustling microscopic picture of statistical mechanics. In the extreme case, Brownian motion may be visible to the naked eye, yet the impacts of the solvent molecules remain invisible even under the microscope. In this way our eyes do perfectly, what physicists have tried to achieve ever since: integrate out the effect of the solvent. This, in a nutshell, is what we are aiming for.

The motion of the combined system of colloidal particles plus solvent is in the best case¹ impossible, simply due to the sheer size of the numbers (of the order 10^{23}) involved.

It took until the beginning of 20th century before Einstein, Smoluchowski and Langevin developed the theoretical approaches for a single particle and Perrin performed the experiments confirming the theoretical results for the mean squared displacement. This solved the single particle problem. Yet, as soon as we want to deal with a potentially large numbers of interacting colloidal particles suspended in a solvent, we can write down the equation governing the time evolution of the probability distribution — but solving it is analytically impossible and we have to resort to numerical methods, such as computer simulations.

However, it is precisely these types of systems with large numbers of colloids subject to Brownian motion, that are abundant in the world around us and account for the wild variety of substances with incredibly different properties from foams to glasses, from milk to crystals.

A somewhat simplified system, that nevertheless exhibits a remarkably rich phase diagram, is exemplified by modelling colloids with hard spheres. In summary it is precisely

¹That is, sticking to classical physics.

such a simulation of Brownian hard spheres at high densities we want to develop. A number of solutions to this problem have been proposed over the last two decades — except none of them was free of fundamental flaws, until very recent propositions were advanced.

A logical extension of this program is to venture into the realm of non-equilibrium Statistical Physics. Our forays are limited to the simplest possible case: namely shear with a linear velocity profile.

1.2 Outline of chapters

Chapter 2 Develops an algorithm for Brownian motion based on displacements, starting from the Langevin equation. Arguments are sketched that make it plausible that the time evolution of the resulting probability distribution obeys the Smoluchowski equation. All major ingredients needed for an event driven simulation are touched on. We then develop the standard simulation boxes for low densities and techniques to gain access to packing fractions beyond freezing with a binary mixture.

Chapter 3 Results are presented from a comparison of soft and hard spheres. A scaling involving the densities and the respective freezing points is identified, that enables us to map a number of quantities, like the structure factor, long time diffusion, the stress-stress correlation function and the viscosity for soft and hard spheres. It turns out that this scaling is particularly successful near freezing and in the long time limit for the dynamical quantities.

Chapter 4 A variety of statistical methods are explained that allow us to extract information from the vast amount of data provided by the simulations. We also take a closer look at Brownian motion and its effect on dynamics, thus providing an indication of the level of the Brownian timescale τ_B required. The notion of interaction forces is developed for hard spheres and is exploited to calculate the stress tensor. This procedure is made plausible for our algorithm in the absence of real velocities. From the stress tensor we develop expressions for the stress-stress correlation function and show that it is compatible with theoretical results.

Chapter 5 We briefly return to the Langevin equation to incorporate shear into our algorithm. We then point out the consequences for the boundary conditions and what this entails for a number of methods we have developed so far. A second method is developed to calculate the viscosity, based on the distorted part of the pair distribution function. We use this to find the viscosities of a range of densities and shear rates in order to then compare them to published results. We propose the use of a binary mixture for this investigation at high densities. We investigate the region of the glass transition presenting a few results and give some outlook for future work.

2

Theoretical background

In his article, *Über die von der molekularkinetischen Theorie der Wärme geforderte Bewegung von in ruhenden Flüssigkeiten suspendierten Teilchen*¹ Albert Einstein described how *Kinetic Theory* regards a suspended particle [17] and derived a formula for the mean squared displacement of such a particle in one dimension:

$$\langle (r(t) - r(0))^2 \rangle = 2Dt. \quad (2.1)$$

Together with the work of Smoluchowski [51] and Langevin[34] this settled the theoretical description of the behaviour of a single Brownian particle more than 100 years ago. Yet, to this day, the same problem at higher densities knows only numerical solutions. One way of approaching this problem is provided by computer simulations and it is this path we intend to follow here: our aim here is to present a framework based in statistical physics that will allow us, loosely speaking, to coarse grain the microscopic picture in order to get as far back towards a thermodynamic view as possible. This is dictated by the limits of processing power and the fact that we, after all, are interested in the particles — not the solvent. For this reason it is convenient to ignore any hydrodynamic interactions other than the Brownian motion. This is often called the *free draining* model and arguably becomes increasingly more realistic at higher densities as the excluded volume interaction becomes dominant. This is the model we are aiming for — not least because of the existence of theories applicable to systems at high densities employing just this free draining approximation.

2.0.1 The Langevin description of a free particle

The equation of motion, that describes in a most intuitive fashion the Brownian movement of a particle in a solvent, was written down by Langevin:

$$m\dot{\mathbf{v}} = -m\zeta\mathbf{v} + \mathbf{F} + \mathbf{f}_s. \quad (2.2)$$

The velocities \mathbf{v} refer to the particle in question. Famously, this equation contains a random force \mathbf{f}_s that is to emulate the random kicks the particle suffers at the hands of the solvent. As a side effect, it is impossible to get any meaningful answer out of this equation unless one turns to statistical averages. The second force, \mathbf{F} , is deterministic in nature and may include gravity or any other external force. In the present discussion it will contain the particle interactions only — and we will feign their absence and defer their treatment until later (see section 2.1.1).

¹On the movement, required by the molecular-kinetic theory of heat, of particles suspended in a fluid at rest.

The first term on the right hand side, $m\zeta\mathbf{v}$, refers to the friction force. This is also due to the bath and as such it is essentially random. Naturally, any particle travelling at some velocity \mathbf{v} through the solvent receives more and stronger kicks on the face that points in the direction of motion. In an untold act of averaging, this systematic portion of the random motion has been collected into the friction force $m\zeta\mathbf{v}$. In light of these details, it is palatable that the random force is strictly symmetric and obeys,

$$\langle \mathbf{f}_s \rangle = 0,$$

as well as uncorrelated:

$$\langle \mathbf{f}_s(t)\mathbf{f}_s(0) \rangle = \mathbf{H} \delta(t) = 2k_B T m \zeta \delta(t). \quad (2.3)$$

In the most general case, this correlation comes in the form of a $d \times d$ -dimensional matrix \mathbf{H} which, in the current context, has the form of a diagonal matrix and will be represented by the constants shown on the far right. It is here that the fluctuation-dissipation theorem is seen at work connecting the fluctuations in the force to the dissipation via the friction coefficient, ζ , which has already had its cameo in equation (2.2).

In an exercise of premeditated ignorance we insist on coarse graining this description and find an equation of the displacements. For this purpose, we consider a free particle first — that is: no interactions for the time being. So the slightly redressed starting point for our journey towards an algorithm of Brownian motion is,

$$m\dot{\mathbf{v}} = -m\zeta\mathbf{v} + \mathbf{f}_s. \quad (2.4)$$

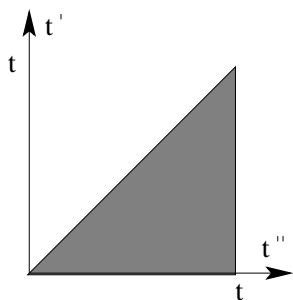
This stochastic differential equation can be solved — (formally) to give:

$$\mathbf{v}(t) = \mathbf{v}_0 e^{-\zeta t} + \frac{1}{m} \int_0^t dt' \mathbf{f}_s(t') e^{-\zeta(t-t')}. \quad (2.5)$$

It can be integrated yet once more to find an equation describing the displacement:

$$\int_0^t dt'' \mathbf{v}(t'') = \int_0^t dt'' \mathbf{v}_0 e^{-\zeta t''} + \int_0^t dt'' \frac{1}{m} \int_0^{t''} dt' \mathbf{f}_s(t') e^{-\zeta(t''-t')}.$$

We will briefly turn our attention to the double integral on the far right hand side, which needs to be treated to a change in the order of integration.



$$\begin{aligned} \int_0^t dt'' \frac{1}{m} \int_0^{t''} dt' \mathbf{f}_s(t') e^{-\zeta(t''-t')} &= \\ \frac{1}{m} \int_0^t dt' \mathbf{f}_s(t') \int_{t'}^t dt'' e^{-\zeta(t''-t')} &= \\ \frac{1}{m\zeta} \int_0^t dt' \mathbf{f}_s(t') \left(1 - e^{-\zeta(t-t')}\right). \end{aligned}$$

We can now join the pieces together and find an equation for the displacements:

$$\mathbf{r}(t) - \mathbf{r}_0 = \frac{\mathbf{v}_0}{\zeta} \left(1 - e^{-\zeta t}\right) + \frac{1}{m\zeta} \int_0^t dt' \mathbf{f}_s(t') \left(1 - e^{-\zeta(t-t')}\right) \quad (2.6)$$

And now for the coarse-graining. It is again the integral that is the focus of attention. We want to move to a time scale, τ_B , that has to balance two opposing requirements. On the

one hand, we want τ_B to be large in comparison to the time scale of the solvent. That is to say: τ_B contains a possibly large number of solvent kicks. On the other hand, τ_B is meant to be so small that $e^{-\zeta n\tau_B} \approx e^{-\zeta(n+1)\tau_B}$ can be considered as constant. More precisely: τ_B is small in comparison to the friction time scale, or $\tau_B \ll \frac{1}{\zeta}$.

On this time scale, we want to examine the integral in equation (2.6) again. Without loss of too much generality, we are able to limit our curiosity to integrals that we can split into n chunks of τ_B , such that $n\tau_B = t$:

$$\begin{aligned} & \frac{1}{m\zeta} \int_0^t dt' \mathbf{f}_s(t') \left(1 - e^{-\zeta(t-t')}\right) = \\ & \sum_{i=1}^n \frac{1}{m\zeta} \int_{(i-1)\tau_B}^{i\tau_B} dt' \mathbf{f}_s(t') \left(1 - e^{-\zeta(t-t')}\right). \end{aligned}$$

If we now stick to our guns and clamour for the exponential function to be a constant on the scale of τ_B , we can pull it advantageously out of the remaining integral.

$$\approx \sum_{i=1}^n \left(1 - e^{-\zeta(t - [i-\frac{1}{2}]\tau_B)}\right) \frac{1}{m\zeta} \int_{(i-1)\tau_B}^{i\tau_B} dt' \mathbf{f}_s(t'). \quad (2.7)$$

The central limit theorem assures us that any sum of Gauss-distributed random variables will be at least as Gaussian as any single one of them. In our case, this means that

$$\frac{1}{m\zeta} \int_{(i-1)\tau_B}^{i\tau_B} dt' \mathbf{f}_s(t') = \mathbf{R}_s, \quad (2.8)$$

with \mathbf{R}_s as yet another Gauss-distributed variable. In order to progress just that little bit further, we want to consider the *overdamped* case, where ζ becomes very large — in other words: the friction time scale becomes very short and the momentum relaxes on this very short time scale. In this regime, we can neglect the first term on the right hand side of equation (2.6), as \mathbf{v}_0/ζ is negligible compared to the diffusive displacement: A statement that can be read as saying that the memory of the momentum is erased completely by the time we get to the end of our Brownian time step, τ_B .

So we are essentially left with the results of equation (2.7), as well as those of equation (2.8), which leads to the equation of motion we are interested in:

$$\begin{aligned} \mathbf{r}(t) - \mathbf{r}_0 & \approx \sum_{i=1}^n \left(1 - e^{-\zeta(t - [i-\frac{1}{2}]\tau_B)}\right) \mathbf{R}_s \\ & = n\mathbf{R}_s. \end{aligned} \quad (2.9)$$

We now know that our displacement is governed by a normal distribution function with mean zero. But what the second moment of the distribution is remains to be answered using Chandrasekar's theorem [13]. It states that a stochastic variable,

$$\mathbf{x}(t) = \mathbf{a}(t) \int_0^t dt' \mathbf{b}(t-t') \cdot \mathbf{f}_s,$$

with a random force \mathbf{f}_s centred around zero, $\langle \mathbf{f}_s \rangle = 0$, and an autocorrelation $\langle \mathbf{f}_s(t) \mathbf{f}_s(0) \rangle = \mathbf{H}\delta(t)$ determined by the matrix \mathbf{H} , of dimension $d \times d$, will lead to a conditional probability density function of the following form:

$$P(\mathbf{x}, t | \mathbf{a}(0), t = 0) = \frac{1}{(2\pi)^{\frac{3}{2}} |\mathbf{M}|} \exp \left[-\frac{1}{2} (\mathbf{x} - \mathbf{b}(t)) \cdot \mathbf{M}^{-1} \cdot (\mathbf{x} - \mathbf{b}(t)) \right],$$

provided the matrix $\mathbf{x} = \mathbf{a}$ at time $t = 0$ and \mathbf{M} is defined as

$$M_{ij}(t) = \sum_{kl} \int_0^t dt' a_{ik}(t') H_{kl} a_{lj}(t').$$

On the diffusive time scale we have been considering so far, this means that the distribution function we sample is,

$$P(\mathbf{r}, t | \mathbf{r}(0), t = 0) = \frac{1}{(4\pi D_0 t)^{\frac{3}{2}}} \exp \left[-\frac{|\mathbf{r} - \mathbf{r}(0)|^2}{4D_0 t} \right]. \quad (2.10)$$

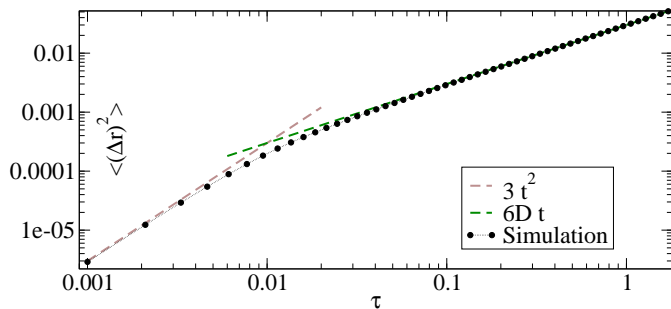


Figure 2.1. Mean squared displacement of a free particle.

for all practical purposes uncorrelated. The prefactor, $2k_B T m \zeta$, stems from the equipartition theorem and the idea that in equilibrium $\langle \mathbf{v}(t) \mathbf{v}(t) \rangle = k_B T / m$. This correlation can be evaluated explicitly (2.5) using the expression for $\mathbf{v}(t)$ [15] to give,

$$\lim_{t \rightarrow \infty} \langle \mathbf{v}(t) \mathbf{v}(t) \rangle = \lim_{t \rightarrow \infty} \mathbf{H} \frac{1}{2m^2 \zeta} \left(1 - e^{-2\zeta t} \right) = \mathbf{H} \frac{1}{2m^2 \zeta} \equiv k_B T / m.$$

As a connection between the correlation of the forces and the friction, it constitutes what it usually referred to as *fluctuation-dissipation* theorem. Even though the friction as such does not play a role in displacements, it is present in the algorithm even on the diffusive level, in as far as we have insisted on the fact that momentum is relaxed on the timescale τ_B and no trace of momentum memory is carried over to the next displacement.

To cast equation (2.9) as it stands into the form of an algorithm is straight forward. To this end we need only consider the case, $n = 1$, for this is what the computer would be interested in:

$$\mathbf{r}(\tau_B) = \mathbf{r}_0 + \mathbf{R}_s = \mathbf{r}_0 + \tau_B \mathbf{V}_s. \quad (2.11)$$

This will reproduce the trajectory of a free particle as exemplified in figure 2.1 by a system at very low density. The mean squared displacement shows two characteristic regimes: the ballistic flight on a timescale up to $\tau_B = 0.01$ and the diffusion for timescales larger than that. We can read off the diffusion coefficient, D , as given in the Einstein relation in equation (2.1) by determining the slope of the mean squared displacement at long times. Unfortunately all this is valid only for a single colloid where no other particles come into the picture. More than one particle spells trouble.

2.1 Algorithms for Brownian motion of hard spheres

A number of attempts have been made in the past decades to simulate multi-particle systems of hard spheres in a suspension starting from a single particle diffusion process. The crucial ingredient in any of these simulation schemes is the way they deal with resulting overlaps.

One solution to this conundrum is to apply Monte Carlo methods. This has been done — amongst others — by Cichocki and Hinsen [14]. The idea is to check any proposed move for overlaps, in which case the displacement is ignored. This method has above all the drawback that it will, with increasing density, calculate mainly void moves, which renders it almost impossible to apply to very high densities. In figure 2.2, all but one move would need to be rejected.

Another attempt is due to Heyes and Melrose [29], who try to resolve the fundamental problem of the Monte Carlo algorithm by not rejecting any failing move, but by correcting the overlap. Whenever a random displacement results in a violation of the boundary condition the offending sphere is withdrawn along the line of displacement until the overlap is cleared. This redresses the shape of the distribution function. In fact, it does so in an unwanted fashion, as the contact value is favoured in an unnatural way. The result is that the structure of such a fluid fails to portray that of a real fluid. This shortcoming is reflected for example by the radial distribution function that exposes the contact value as too high and with it everything that depends on it, as for example, the pressure.

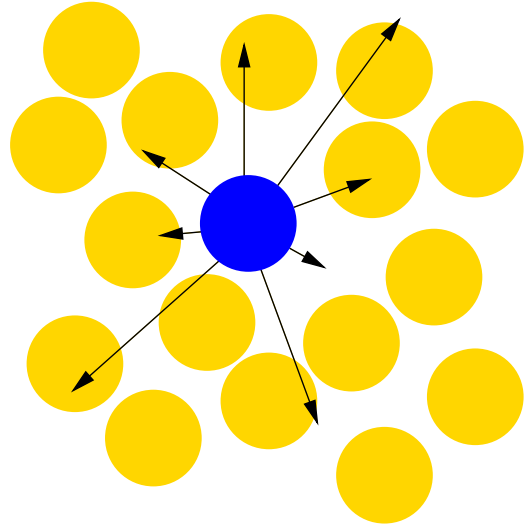


Figure 2.2. Trial moves in a dense medium.

This blemish has been addressed by Strating [52]. In this method, the overlaps are not only corrected but at the same time the displacement size is also conserved. To this end, a velocity is calculated from the displacement divided by the time interval. With this velocity, elastic collisions between the overlapping particles are simulated.

We will motivate these choices and end up with an simulation scheme that is a very close relative of Strating’s idea and is known as De Michele’s algorithm [48].

2.1.1 Dealing with collisions

The most convenient way to introduce interaction forces would be to return to equation (2.2), where a force \mathbf{F} is included. This term may contain the interaction forces. Further progress is hindered by the fact that this addition turns the Langevin equation into a non-linear stochastic differential equation. In particular any attempt to discretise this type of equation² fails due to the singular nature of the hard sphere interaction.

There exists an entirely different theoretical approach to this type of problem, starting from probability densities and their rates of change. This leads in general to a multivariate *Fokker-Planck* equation [54] for velocities and positions. In particular, Brownian motion with interactions results in what is termed *Kramer’s equation*. In the overdamped limit, Kramer’s equation evolves on two timescales and it is tempting to eliminate the *fast* variables in favour of a description containing only the *slow* variables. Out of these considerations

²The standard route to Brownian dynamics simulations takes precisely such an equation and discretises it including its continuous interaction potentials of the colloids.

arises the *Smoluchowski* equation.

$$\frac{\partial}{\partial t} P^N(t) = D_0 \sum_i^N \frac{\partial}{\partial \mathbf{r}_i} \cdot \left(\frac{\partial}{\partial \mathbf{r}_i} - \frac{1}{k_B T} \mathbf{F} \right) P^N. \quad (2.12)$$

Equation (2.12) turns trivially into the diffusion equation when $\mathbf{F} = 0$ and, as such, the Gauss distribution is not entirely unexpectedly a solution of the single particle Smoluchowski equation. In other words: a single free particle does what we already know it should do from the Langevin equation: it diffuses. In a cursory manner, this indicates how the Langevin and the Smoluchowski equations are connected. The Langevin equation is the suitable instrument to answer the most pressing question on the level of the simulation — namely: What does particle i do next? A large number of such trajectories conspire to a distribution function. The time evolution of this probability density function is described by the Smoluchowski equation.

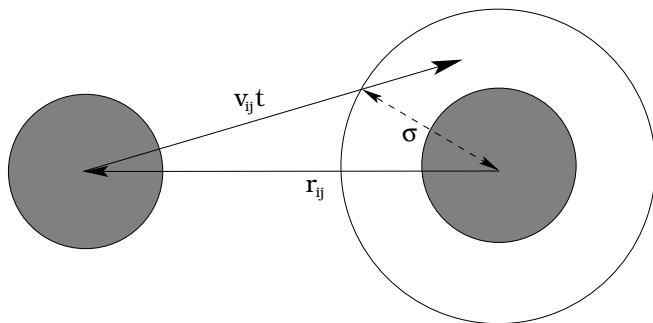


Figure 2.3. *Two body collision in relative coordinates.*

Scala [48] to legitimise a way of incorporating collisions into the Langevin equation.

We start with two particles in close vicinity. The hard sphere interaction manifests itself primarily as the boundary condition of *no overlap* for each one of the two particles. This behaviour is conveniently summed up by the statement that the probability flux across the boundary is zero. In relative coordinates, the condition of no overlap may be interpreted as that of a point particle facing a correspondingly larger no-go area (figure 2.3).

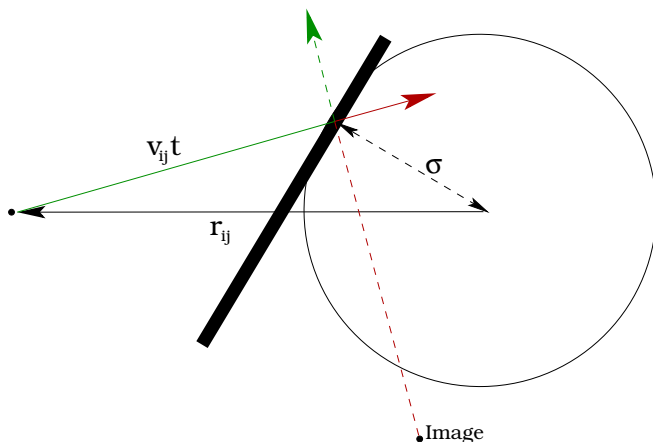


Figure 2.4. *A collision can be described by judiciously selecting trajectory parts from hard sphere and image (not to scale as $\Delta \mathbf{r} \ll \sigma$ is not obeyed).*

It is therefore vital that the displacement is small compared to the particle diameter: $\Delta \mathbf{r} \ll \sigma$.

Naturally it is then the Smoluchowski equation that one turns to when it comes to assessing whether our algorithm is producing sensible results. But, alas, the multi-particle Smoluchowski equation remains intractable analytically. The closest we can get to solving it is the case of two particles. This fact has been exploited by Antonio

In this picture, two key ideas become important: At the point of contact, where in our case the elastic collision takes place, the point particle is oblivious to the fact that it is colliding with the curved surface of a large sphere. In other words: the point of contact has no curvature and may for the purpose of the discussion of any one collision be replaced by a wall. For several collisions, as they might occur during any displacement, we are crucially dependent on the curva-

This way the geometry of the collision is greatly simplified, as sketched in figure 2.4. The particle on the left follows a straight path to the point of contact ($\mathbf{v}_{ij}t$). The collision can now be seen as a simple reflection on the wall indicated. The reflected path coincides with the undisturbed straight trajectory of a physical mirror image from the collision point onwards (green dashed line).

The second key observation builds up on this in the sense that it tells us how to deal with the probability density function in the interaction-region. The elastic collision with a wall has the effect that whatever probability flux there was into the wall has to be reversed into the region in front of the wall. This might be envisaged by placing an image particle as if mirrored by the wall such that the fluxes across the boundary cancel — an idea that is illustrated in figure 2.5. The sum of the probability distributions of particle and image (black and blue lines respectively) is coloured in grey and shows how the probability of finding the colloid near the wall is enhanced. Whichever way one prefers to look at it, the result is that the probability distribution is skewed to accommodate the reflected flux. This mirrored flux is another way of saying: the size of the displacement is conserved for the point particle. This can be achieved by replacing the displacement on the time scale τ_B by a velocity as indicated in equation (2.11) such that $\mathbf{R}_s = \tau_B \mathbf{V}_s$. With these respective *pseudovelocities* an elastic collision is performed. This corresponds to choosing the particle trajectory up to the collision point and taking that of the image (dashed arrow in figure 2.4) away from it to find the final position.

This interpretation can be tested against the result from the two-particle Smoluchowski equation as has been done by Scala et al [48] with favourable results.

It emerges therefore that the algorithm is capable of reflecting the theoretical results, provided the time scale τ_B is set with care. This *Brownian time step* τ_B , after which new displacements are drawn from the distribution, has to be small enough to ensure that the algorithm works on the level of binary collisions. Within this limit, the multi-particle problem disintegrates into a number of two body situations, and, in addition, the dynamics is correct as well. It is therefore vital to keep an eye on the *Brownian time step* τ_B . We will return to that in section 4.3.

We have now found a way to implement two body collisions in a meaningful way into the algorithm. The recipe to simulate more than one particle can thus be summarised as follows:

- We have now found a way to implement two body collisions in a meaningful way into the algorithm. The recipe to simulate more than one particle can thus be summarised as follows:

- Draw a random displacement from a Gaussian distribution.
- Check for overlaps.
- Process overlaps as elastic collisions invoking a *pseudovelocity*.

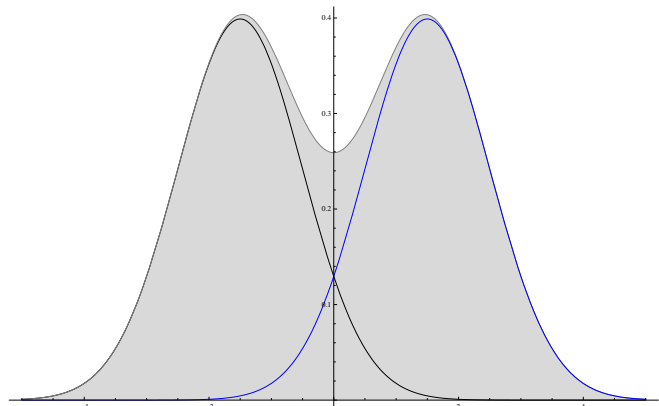


Figure 2.5. Particle- and image-distribution add up to the reflected distribution (grey). The wall is marked by the vertical axis.

In practise we start with the pseudovelocity \mathbf{V}_s drawn from a Gaussian distribution, which is equivalent to a displacement as long as the Brownian time step τ_B is fixed. With this velocity the particle propagates freely unless it encounters another particle until the next random pseudovelocity is drawn. In short: this is Newtonian dynamics with a *hyperactive* thermostat — together with the added peculiarity that Newtonian dynamics employs pseudovelocities that do not necessarily reflect the true velocity of the specific particle. The algorithm can be written down as a discrete equation of the following form:

$$\mathbf{v}_i(t + dt) = \mathbf{v}_i(t) + \sum_{n=n_t} (\mathbf{G}_{k_B T}^s - \mathbf{v}_i(n\tau_B)) + \sum_{coll} \Delta \mathbf{v}_{ij}(t_{ij}). \quad (2.13)$$

Again: the pseudovelocities \mathbf{v} are used for convenience and merely represent the displacement under the provision that a τ_B is fixed. While equation (2.13) is straightforward for a dt involving either one collision or a Brownian time step, the processes become more intricate as soon as several of these events have to be ordered in time. It must be noted that the appearance of $\mathbf{v}_i(n\tau_B)$ as well as $\mathbf{v}_{ij}(t_{ij})$ introduces a recursive character into the equation in those cases. The algorithm however operates on the level of single events.

For the simplest case equation (2.13) states: the velocity of particle i at some time-span, dt , later is determined by two possible types of events — Brownian time steps and collisions.

A Brownian time step is a regularly recurrent affair. Every τ_B , velocities are drawn from a Gaussian distribution $G_{k_B T}^s$, with a second moment depending on $k_B T$. It is important to note that any velocity the particle had at that point in time is annulled. In other words: whatever is drawn from the Gaussian distribution is then the current velocity. In line with the Langevin equation, the random kicks are not resolved in full detail — much rather this Brownian event is to be interpreted as a resultant force due to some already coarse-grained number of solvent kicks.

The idea that the velocity is zero whenever we draw a new one from the Gaussian distribution stems from the interpretation of $\tau_B \mathbf{v} = \Delta \mathbf{r}$ as a random displacement and the underlying desire to simulate displacements according to a multi-particle Smoluchowski equation. We have seen that the displacement does not depend on the previous displacement and that means neither magnitude nor direction of the velocity are carried over.

The second term on the right denotes the change of direction and velocity due to collisions. In the case of elastic collisions, this is a function of the relative coordinates and time — $\Delta v_{ij} = \Delta v_{ij}(t, \mathbf{r}_i - \mathbf{r}_j, \mathbf{v}_i - \mathbf{v}_j) = \Delta v_{ij}(t, \mathbf{r}_{ij}, \mathbf{v}_{ij})$. The main difficulty, however, lies in becoming aware of all the collisions that need to be processed.

2.1.2 Finding a collision

A crucial job of the algorithm is finding collisions. Let's assume we have two particles at positions \mathbf{r}_1 and \mathbf{r}_2 , as well as the respective velocities \mathbf{v}_1 and \mathbf{v}_2 . In this case, the question whether a collision will occur is then answered by,

$$|\mathbf{r}_1 + \mathbf{v}_1 t - (\mathbf{r}_2 + \mathbf{v}_2 t)| = l,$$

where l is the minimum separation of the particles (that is the sum of their radii — in most cases $l = 1$). In relative coordinates $\mathbf{r} \equiv \mathbf{r}_1 - \mathbf{r}_2$ and $\mathbf{v} \equiv \mathbf{v}_1 - \mathbf{v}_2$, this is simply asking: does a point particle at \mathbf{r} touch a sphere of radius l around the origin at any time?

The equation

$$|\mathbf{r} + \mathbf{v}t| = l,$$

has solutions

$$t = - \left(\mathbf{r} \cdot \mathbf{v} \pm \sqrt{(\mathbf{r} \cdot \mathbf{v})^2 - v^2 (r^2 - l^2)} \right) v^{-2}.$$

We can narrow down the number of solutions by insisting on $\mathbf{r} \cdot \mathbf{v} < 0$ and $(\mathbf{r} \cdot \mathbf{v})^2 - v^2 (r^2 - l^2) > 0$.

The first condition explicitly requires the two particles to approach each other, while the latter excludes solutions in which the particles approach each other but nevertheless do not collide. The condition can be rewritten as

$$\begin{aligned} (\mathbf{r} \cdot \mathbf{v})^2 &> v^2 (r^2 - l^2), \\ r^2 \cos^2 \theta &> r^2 - l^2, \\ (1 - \cos^2 \theta) &< \frac{l^2}{r^2}, \\ \sin^2 \theta &< \frac{l^2}{r^2}, \\ \sin \alpha &< \frac{l}{r}, \end{aligned}$$

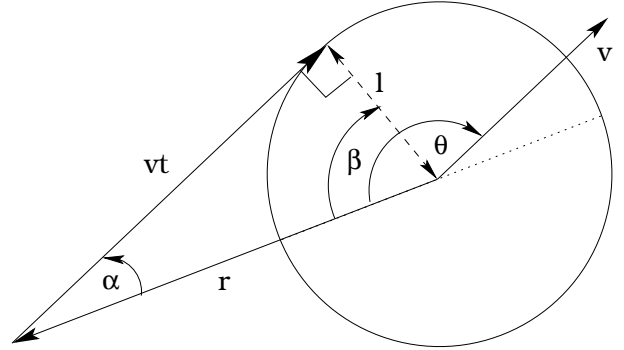


Figure 2.6. Collision of two particles in relative coordinates. Note that $\frac{\pi}{2} < \theta < \frac{3\pi}{2}$ is a necessary condition for a collision unless particles overlap to start with.

which is precisely the condition of α being less than the contact angle (see figure 2.6).

Having excluded these, we are still left with two solutions — of which the earlier one (that is subtracting the square root) is the one we are interested in.

The second solution describes when the point particle would leave the far side of the particle, having travelled through the interior. Should this return a negative time value, then an overlap has occurred. This can be seen as follows:

$$\begin{aligned} \underbrace{-\mathbf{r} \cdot \mathbf{v}}_{+ve} - \underbrace{\sqrt{(\mathbf{r} \cdot \mathbf{v})^2 - v^2 (r^2 - l^2)}}_{+ve} &< 0 \\ -\mathbf{r} \cdot \mathbf{v} &< \sqrt{(\mathbf{r} \cdot \mathbf{v})^2 - v^2 (r^2 - l^2)} \\ r^2 v^2 \cos^2 \theta &< r^2 v^2 \cos^2 \theta - v^2 r^2 + v^2 l^2 \\ r &< l. \end{aligned}$$

This is an important and, as it were, complementary check on the system during run time. Even though it is only sensitive to overlaps in which both particles approach each other — this is precisely the class of overlaps indicating serious problems (for more on this see section 2.2.3).

2.1.3 The event-tree

On contact, hard spheres are subject to infinite forces. This is true for the collision of two colloids, as well as for interactions with the bath. The trajectory of a Brownian particle is said to be nowhere differentiable. This rules out the standard scheme of Molecular

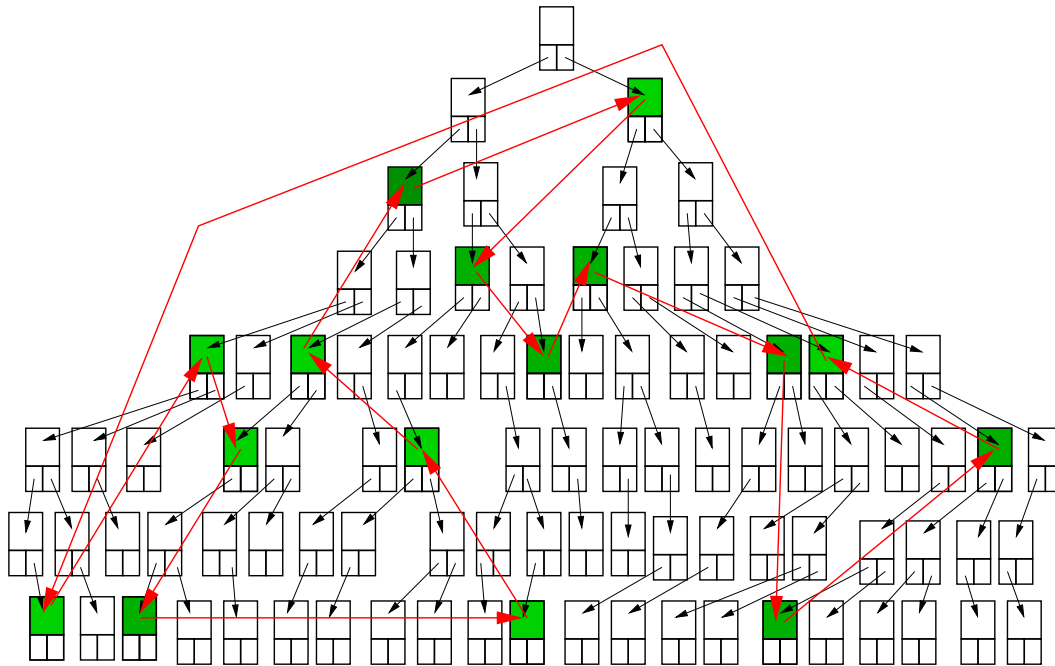


Figure 2.7. Each Box represents an event. The nature of a binary tree dictates that at each leaf there are at most two choices. The leftmost leaf represents — for no other reason than by definition — the next event to be processed. The event tree holds a vast amount of information — most of it redundant. So in order to find all events related to one particle (green) all of them are linked together in a circular (red).

dynamics. A suitable way of dealing with such a discontinuous potential is an event-driven algorithm [43].

The method relies on the fact that in between collisions a particle moves undisturbed and in a straight line. It is therefore advantageous to process only changes to the straight trajectory when they occur and move the particle from the position of one such event to the next. A consequence of this approach is the absence of fixed time steps. This is the basic feature of an event-driven algorithm: it does not evolve with a fixed time step. On the contrary: time propagation is determined by the events in the simulation.

Conversely, this means that the algorithm has to deal with finding and sorting the events. Events comprise anything that has to be processed in the course of a simulation run. In general this will include:

- collision (particle event).
- leaving and entering box according to periodic boundary conditions (particle event).
- cell crossings³ keeping track of the position (particle event).
- Brownian time steps choosing new random velocities for all particles (particle event).
- saving time steps for writing data to file (administrative event).
- terminating the simulation at the end (administrative event).

³This will be explained in section 2.1.4

This presents a standard problem in sorting, which we opted to solve with a binary tree — the so called *event-tree*. Each event has a time associated with it that is used as the defining characteristic when it comes to finding a position in the event-tree. In a binary tree two choices branch off from each leaf. In our case, these branches correspond to choices in the time ordering: all earlier times are towards the left, any events later in time to the right. Inserting a new event starts at the root (in figure 2.7 at the top) and from there takes a path through the leaves determined by the choices at each branch. This has to be repeated until an empty leaf is found, where the new event will be placed.

Now that the event-tree is filled, it is about time to process one of the events. The most pressing business would be placed at the leftmost position of the tree — that literally means going left at every branch until we reach the end of the line. Any one leaf will contain all information needed to process the correct event. For the event driven simulation this is not excessive: essentially we need the time value, and two integer numbers representing either two particles or one particle number and a code betraying what ought to be done with that one particle.

Having dealt with the event, another difficulty presents itself: cleaning up. In general, if something happens to the pseudovelocity of one particle, any other particle event involving this particle will be obsolete. For this purpose, a structure within the event-tree is introduced that connects all events associated with one colloid. All these events should now be removed from the tree. We think this method is useful, as rejuvenating the tree will keep searching times short. This may be of particular interest in Newtonian Dynamics.

In Brownian dynamics, τ_B defines a species of event-horizon beyond which no particle event matters. The only events that exist independent of τ_B are administrative events. This peculiarity is due to the fact that at the Brownian time step all pseudovelocities change. So no particle event is worth keeping beyond τ_B . This mechanism keeps the tree nicely pruned.

This has the somewhat surprising side effect that, under certain circumstances, Brownian dynamics can be faster than Newtonian dynamics. In this case, it might be worthwhile to ponder further ways to optimise and trim the tree-structure for the Newtonian dynamics. We are, however, mainly interested in Brownian dynamics.

2.1.4 Neighbour cells

Performance is of great concern. One way of reducing the order of the algorithm is by cutting the number of pairs that are checked for possible collisions. As it stands so far, we would check of the order of N^2 pairs of particles for collisions. A time consuming business,

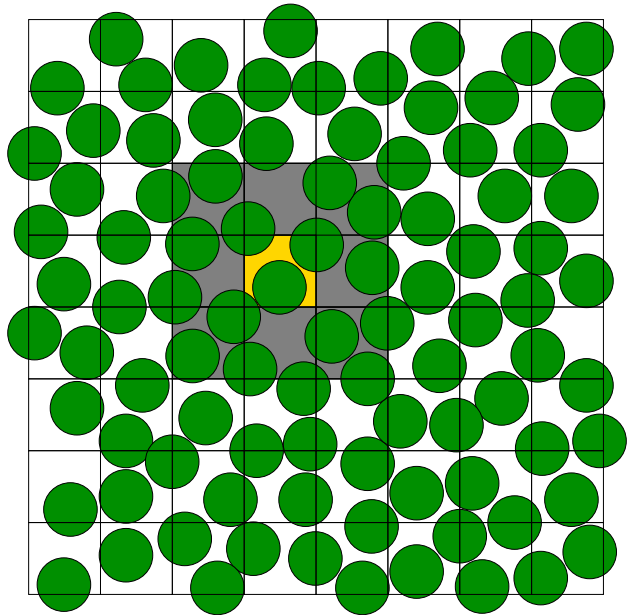


Figure 2.8. Searching only neighbouring cells for collisions reduces unnecessary calculations.

as taking a square root is involved when calculating the collision time. The way out is to introduce neighbour lists or neighbour cells. Both ideas aim to reduce the number of possible collision partners by observing that opponents have to be near to be promising candidates for a collision.

We adopt the idea of neighbour cells. It requires some effort to keep track of the cell each of the particles belongs to, but is rewarded with the immense advantage of only the neighbouring cells needing to be considered, when searching for possible future collisions. This is sketched in figure 2.8, where the particle in the yellow cell can collide only with spheres from one of the grey cells around it.

The saving is greatest when the number of collision checks is reduced to a minimum. This is achieved by tuning the size of the cell to the smallest possible size that still fits one sphere completely inside⁴. In this manner, the number of collisions to be calculated reduces to $\mathcal{O}(N)$.

2.2 The standard system

As we zoom out from the collisions to the neighbours this might be the point to add a brief comment on the bigger picture: typically our system would comprise of the order $N = 1000$ particles. We also adopted the commonplace periodic boundary conditions to reduce the effects of the edges of the cubic simulation box.

In order to start a simulation the particles are placed on a simple cubic lattice. Velocities are then drawn at random from a Gaussian distribution to let the system evolve towards equilibrium. All further simulations are run from such an equilibrated configuration.

The standard deviation of the velocity determines the temperature of hard spheres: $\langle v^2 \rangle = \frac{3}{m}k_B T$. Inherently Newtonian dynamics does not show any dependence on temperature. Temperature leads to a different timescale, but does not change the dynamics qualitatively.

In Brownian motion a time scale τ_B is introduced on which the hyperactive thermostat operates. But we have already seen that τ_B comes with strings attached. That means, having picked the packing fraction ϕ one might still be able to choose $k_B T$ freely, but then the Brownian time scale τ_B follows from the *hyper* in hyperactive, or, to put it in a more somber fashion: τ_B is determined by the requirement to simulate *Brownian* dynamics⁵.

The reality is that we would have $k_B T = 1$ for convenience, leaving the density as the only entirely free parameter in Brownian dynamics simulations.

In all our simulations, the particle diameter σ determines the length scale and the particle mass m the unit of mass. With these conventions, the time is given in units of $t \equiv t' / \left(\sigma \sqrt{\frac{m}{3k_B T}} \right)$ unless otherwise stated⁶.

⁴This is a typical source of error when using a binary or polydisperse system with different sized particles and usually results in producing plenty of overlaps.

⁵For a more quantitative discussion see section 4.3.

⁶This is the case in chapter 3 where we adopt the timescale convenient for the comparison with soft spheres.

2.2.1 Into high densities

A dimensionless measure of the density of a system is the *packing fraction*, which gives the ratio of the volume of the collisions, as compared to the total volume of the system. It is defined as

$$\phi = \frac{4}{3}\pi r^3 \frac{N}{V} = \frac{\pi\sigma^3}{6}\rho.$$

With *high* densities we refer to a system at packing fractions beyond the freezing point. The freezing point for hard spheres has been found [5] to be at $\phi = 0.494$. And this brings us straight to the heart of the matter. We want to discuss mainly two difficulties here:

- How do we set up a system with packing fractions higher than simple cubic ($\phi \approx 0.52$)?
- What can be done to avoid crystallisation at high densities?

Beyond freezing

In order to get to densities higher than $\phi \approx 0.52$ one might want to use a different starting configuration. We have, however, begun with the simple cubic which has the advantage of being quick and easy to set up. In addition, it is not the type of crystal hard spheres want to arrange themselves in, which means that the hard spheres will have to rearrange and, in the course of this, melt into the fluid state for densities low enough. The downside is, of course, that it takes a while to melt the simple cubic crystal.

To get to packing fractions beyond the simple cubic configuration, we employ the following recipe: We take a system at an unproblematic density (that is $\phi < 0.50$) and then calculate to what size particles have to be inflated in order to reach the desired packing fraction. We then employ a special simulation run that swells all particles gently as they jostle around the box according to the space they have around them. We never swell the size in such a manner that particles touch due to this procedure, but limit our expansion to a fraction of the free path around one particle (light blue in figure 2.9), in order to ensure mobility.

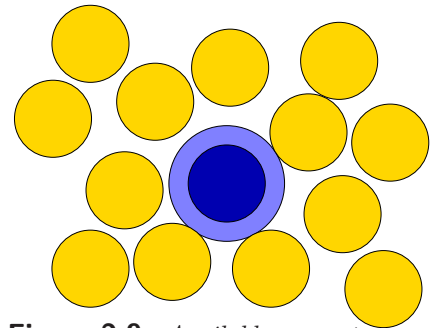


Figure 2.9. Available space to increase the size of one sphere.

When all particles have reached the assigned radius, the whole system is rescaled to return to the familiar setting with the diameter as unit length scale $\sigma = 1$. The overall effect of this procedure is nothing other than of shrinking the box while keeping the particle size fixed.

When all particles have reached the assigned radius, the whole system is rescaled to return to the familiar setting with the diameter as unit length scale $\sigma = 1$. The overall effect of this procedure is nothing other than of shrinking the box while keeping the particle size fixed.

In this manner we can get to random close packing at $\phi \approx 0.64$ — but not beyond.

2.2.2 Avoiding crystallisation — the binary system

Arranging high density systems presents immediately the next problem: crystallisation. A monodisperse hard sphere system will always crystallise when it has a packing fraction above the critical density. Nevertheless, this is not an instantaneous process and there might well be a period of time during which one would be observing a system somewhere between a liquid at high densities and a crystal — manifestly out of equilibrium.

The way to achieve high densities without crystallisation is to use a moderately polydisperse or — as in our case — binary system. There is a whole plethora of distinct crystals in binary mixture that are induced by different proportions of size and number. It is therefore not much of a surprise when a randomly chosen binary system displays signs of ordering. We have therefore adopted a system previously tested [20], which has the following properties:

- The size ratio, defined as the diameter of the big particle over the diameter of the small, gives $\frac{\sigma_b}{\sigma_s} = 1.20482$.
- The number ratio, defined as the number of big particles over the total number of particles, is $\frac{N_b}{N} = 0.4933$.

The swelling procedure carries over in exactly the same manner as described above, with the sole difference that now two species of particles develop with different radii. The length scale is rescaled to the diameter of the larger particles.

2.2.3 Numerical limits and overlaps

The numerical accuracy of computers is limited. This has a number of direct consequences that play a role in our simulations, amongst which we find:

- In collisions, both particles are brought in contact⁷. With limited numerical accuracy both are either not quite at contact or already overlapping — always.
- Insufficient precision in the time variable disturbs the time ordering.

These are the two ingredients that spell trouble in various combinations of events with a similar mechanism.

The first point alone is not of much concern. It introduces a numerical error into the trajectories, but it does not interfere with subsequent functioning of the algorithm. As the error is not systematic, it adds a certain degree of randomness to the overall evolution of the phasepoint, which might even be welcomed in a Brownian dynamics simulation.

In an event driven algorithm, a collision will trigger the following processes. Say the collision was detected and is now the next event to be dealt with then the particles are moved to their contact position — inevitably with slight numerical errors. Let us assume, for the sake of argument, that both overlap as illustrated in figure 2.10. Once in contact, the new pseudovelocities are calculated according to the recipe for elastic collisions. This is depicted by the arrows (\mathbf{v}_1 and \mathbf{v}_2) in figure 2.10. At this point, all particle events concerning any one of these two spheres will be deleted as the pseudovelocity has changed. As a consequence, new potential collisions must be found.

An obvious candidate is the collision both suffer when they disentangle in a very short time. This obvious collision has been discarded by the setup of the searching routine where we demanded that $\mathbf{r} \cdot \mathbf{v} < 0$ in relative coordinates, which translates into: look only for collisions when both particles move towards each other (see section 2.1.2).

⁷This is done by multiplying with a Δt that is necessarily inaccurate — in the worst case increasingly so.

But it is a combination of both points above that causes some disruption. When a Brownian time step has nearly the same time tag⁸ as any particle event, it is vital to make sure the particle event gets processed before the all devouring Brownian time step. A match with a collision might provide a suitable example. Whenever the Brownian time step is executed first, the collision is lost — which is usually correct, as the velocities have changed.

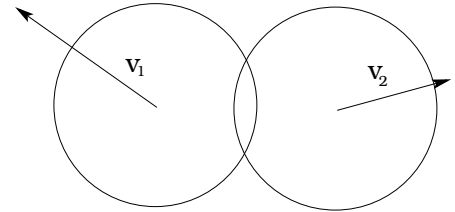


Figure 2.10. *Two-body collision.*

The crux of the matter is that both particles might in fact overlap due to the numerical inaccuracies and then we have the situation illustrated in figure 2.11 for the two right hand particles (\mathbf{v}_2 and \mathbf{v}_3). To the searching routine it now appears as if the only correct collision has already happened in the past and the next — but incorrect — collision will occur when both extricate themselves, having passed through each other.

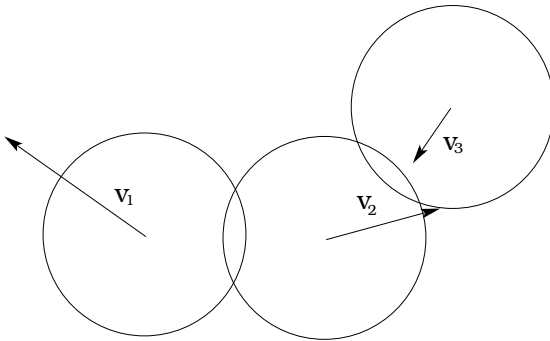


Figure 2.11. *Triple collision about to go wrong.*

Worse still: through a similar thought experiments it is possible to shown that this can – and does — occur for the combination of two simultaneous collision (as illustrated in figure 2.11).

Fact is that these events take place and do so with increasing frequency as the digits after the decimal point of the time coordinate dwindle away at larger and larger time values⁹.

The physically correct solution to this problem is to schedule a collision event as soon as such an overlap is detected. So to speak, it is helping the lost collision to a second chance by some judicious intervention. These corrections grow cumbersome in the limit of long times and/or high densities and put natural limits on the length of single simulation runs: times of the order 10^6 units are the ceiling.

The solution to this problem is to reset the time periodically. With a typical resolution of up to 14 digits behind the decimal point, the coincidence of two events is sufficiently rare and can be handled as described.

⁸The time difference is simply smaller than both particles need to disengage.

⁹This is yet another version of the infamous problem of subtracting two big numbers from one another where the resulting difference is small. It is precisely such a Δt we deal with here.

3

Soft spots of hard spheres

Monodisperse spherical particles with short range repulsions show a simple phase diagram, with only one fluid at low density and one crystal phase at high density and a first order transition in between [44]. The paradigmatic case is the system of hard spheres (HS), where the interaction potential is infinite, whenever particles overlap and zero elsewhere and therefore there is no energy scale in it. In hard spheres, the crystallisation transition was first recognised by Adler and Wainwright [5] and has the freezing and melting points at volume fractions $\phi_f = 0.494$ and $\phi_m = 0.545$, respectively [45]. Additionally, a good approximation for the equation of state for hard sphere fluids was given by Carnahan and Starling using the virial expansion [12], tested experimentally using sedimentation of screened charged colloids [39]. For slightly soft spheres (SS), where interpenetration is not yet an issue, the phase diagram changes quantitatively, shifting the fluid-solid coexistence and introducing temperature as a new variable (the energy scale is set by the potential and temperature is coupled to the volume fraction). Inverse-power potentials ($V(r) \sim r^{-n}$) have been widely used to model soft spheres with the phase diagram being studied as a function of the softness by simulations [2, 3] and theories [11, 46]. Because of the qualitative similarity of the phase diagram of soft spheres with that of hard spheres, a mapping of the former to the latter has also been tried by means of effective diameters [6, 25, 26]. However, an interesting pathology arises in hard spheres which is absent in soft spheres: the elastic modulus for large frequencies diverges in hard spheres [27, 35, 55].

Experimentally, different colloidal systems have been used to model hard spheres, such as silica [53] or latex particles [39, 42], or collapsed microgel particles [31]. Because the hard sphere interaction is an idealisation of quasi-rigid spheres, these systems are usually referred to as "nearly hard spheres" and the question of their softness arises naturally [10]. In most cases, additionally, a (generally thin) polymer layer is adsorbed onto the particles to provide steric stability, which increases the softness of the particles [10]. Furthermore, experiments with really soft particles, such as swollen microgels [50] or star polymers [56], can show new phases due to interpenetration, but also phase diagrams qualitatively similar to the hard spheres one for the harder-particle limit. However, the short range interaction is not directly accessible experimentally [10] and exact knowledge of the true softness of the particle is missing. It is therefore important to know which properties depend on the softness of the particle and if there is a simple scaling for different systems with different softness.

Recent simulations of inverse power potentials have shown that the transport coefficients depend strongly on particle softness, while the hard spheres limit is reached for large values of n ($n > 72$) [28]. It has been shown that the time-correlation functions (and transport coefficients) can be approximately scaled using the exponent n [16, 40], but neither the scal-

ing is perfect nor the exponent is known experimentally. On the other hand, the transport coefficients behave quasi-linearly, with the inverse packing fraction for different softness, which can indicate that the key parameter for mapping the systems is the free volume, although a detailed analysis of the parameters shows inconsistencies (for instance, the free volume vanishes at different density for every transport coefficient) [28]. It is desirable to find a means of simply mapping from soft particles to hard spheres, if such a thing exists, that can be applied to experimental systems.

The freezing point, on the other hand, can be identified with several well-known criteria [47], independently of the interaction potential, such as the Hansen-Verlet criterion, which uses the height of the neighbour peak in the structure factor [24] and a dynamical one proposed by Löwen and co-workers, based on the decrease of the long time diffusion coefficient [36]. Therefore, in this work, we propose to use the density at the freezing point to scale the results. Using computer simulations, we show that the structural and dynamical quantities of interest in systems with inverse-power potentials can be rationalised when plotted against the scaled density, $\rho/\rho_{\text{freezing}}$, for large density. The long range structure is almost identical for systems with equal $\rho/\rho_{\text{freezing}}$, but differences appear at short distances due to the different interaction potentials. The pressure, which shows a rather complicated trend when studied at constant density, increases monotonously with the softness at constant $\rho/\rho_{\text{freezing}}$. The diffusion coefficient and viscosity can be collapsed for $n \geq 18$, including hard spheres, and the time correlation functions only show differences at short times, giving different shear moduli at large frequencies. Our conclusion is therefore that the relative density to the freezing transition is the key parameter governing the structure and dynamics of the system, for large enough n and density. This poses a simple criterion that can be useful for experiments.

3.1 Simulation details

We simulate different monodisperse systems: hard spheres and soft spheres with different "softness". Whereas the interaction potential is continuous for soft spheres, it is not for hard spheres with all the consequences spelled out in chapter 2. This project has been developed in collaboration with Jose B. Caballero and Antonio M. Puertas¹ [?], who have done the simulations for the soft spheres.

For this comparison we use the simulations mainly in the mode of Newtonian dynamics, but we have also performed some Brownian dynamics or damped Newtonian dynamics to make direct contact with experimental colloids. For hard spheres, we generally employ the standard system (as defined in section 2.2) at different densities. The only modification is the timescale, which in this chapter will be in units of $\tau = t / \left(\sigma \sqrt{\frac{m}{k_B T}} \right)$, to be consistent with the timescale of the soft sphere simulations.

The Brownian dynamics also corresponds to the standard system, with a Brownian time step $\tau_B = 0.017$ in the new units.

¹Both from the University of Almeria, Spain

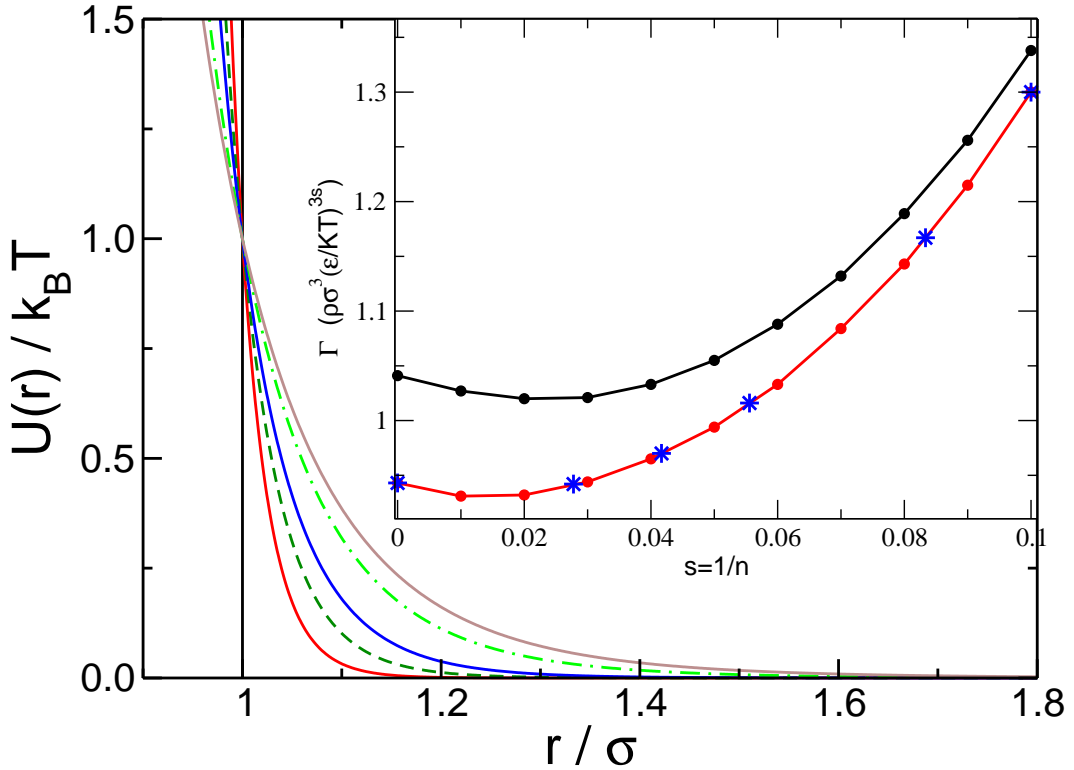


Figure 3.1. Pair interaction potentials used in this work, with decreasing n (increasing softness) from below: $n = 36, 24, 18, 12$ and 10 , and hard sphere. Note the long range of the repulsion for the lowest n . The inset shows the freezing and melting lines in terms of Γ [2]. The stars indicate state points checked in simulations.

3.1.1 Soft spheres

For soft spheres we use a continuous repulsive potential:

$$U_{sc}(r) = \epsilon \left(\frac{r}{\sigma} \right)^{-n} \quad (3.1)$$

where ϵ sets the energy scale and $1/n$ is the *softness* of the potential. In this work, we change n from $n = 10$ to $n = 36$, which provides a wide enough range to show clear effects of the softness of the potential and the crossover to *effective* hard spheres. Figure 3.1 presents the interaction potentials for $n = 36, 24, 18, 12$ and 10 and the hard core repulsion. Note that as n decreases (the softness increases), the potential has a longer range and for $n = 10$, the interaction energy is negligible only for distances above $r \approx 2\sigma$.

Since the interaction potential is soft, the particle volume cannot be unambiguously defined and thus the volume fraction is not a convenient control parameter for these systems, although it is commonly used in experiments. Instead, states featuring potentials with different softness can be compared using the *effective density* defined by the parameter $\Gamma = \rho\sigma^3(\epsilon/k_B T)^{3/n}$, where ρ is the number density. In this work, the temperature is fixed to $k_B T = \epsilon = 1$ and variations in Γ are caused by changes in the number density exclusively.

Conventional molecular dynamics is performed, integrating Newton's equations of motion with velocity rescaling to maintain constant temperature. The time step for the integration is $\delta t = 0.002$, in standard units of $\sigma\sqrt{m/\epsilon}$. All potentials have been truncated for $V < 10^{-3}$.

n	$s = 1/n$	Γ_{freezing}
∞	0	0.943
36	0.0277778	0.942
24	0.0416667	0.970
18	0.0555556	1.016
12	0.0833333	1.167
10	0.10	1.300

Table 3.1: Tabulated data of the equilibrium phase diagram from Agrawal and Kofke [2].

Damped Newtonian dynamics have been performed also, introducing friction and fluctuation (Brownian) forces. For particle j , the equation of motion is now:

$$m\ddot{\mathbf{r}}_j = \sum_i \mathbf{F}_{ij} - \gamma\dot{\mathbf{r}}_j + \mathbf{f}_j \quad (3.2)$$

where \mathbf{F}_{ij} is the interaction force between particles i and j , γ is the friction coefficient with the solvent and \mathbf{f}_j is the Brownian force. The fluctuating and viscous terms are related by the fluctuation dissipation theorem: $\langle \mathbf{f}_j(t')\mathbf{f}_i(t) \rangle = 6k_B T \gamma \delta_{ij} \delta(t - t')$. In this work, $\gamma = 20$, which gives strong damping, with the equations of motion being integrated using the algorithm developed by Heun [38], with a time step $\delta t = 0.0005$.

3.2 Comparing soft and hard spheres

Agrawal and Kofke used Gibbs-Duhem integration to compute the solid-fluid phase boundary for soft spheres modelled with inverse-power potentials, starting from the FCC-fluid coexistence in hard spheres [2]. Their results for the freezing transition are presented in Table I (and in the inset to figure 3.1) for different values of n and the hard spheres system. Note that freezing density does not evolve monotonously with the potential softness (at constant temperature $k_B T = \epsilon$, $\Gamma = \rho\sigma^3$): upon decreasing n from infinite (increasing softness starting from hard spheres), Γ_{freezing} first decreases and then increases for $n < 36$.

Figure 3.2 presents the pressure in the fluid phase up to the freezing point for different values of n . Whereas at low density the pressure is almost independent of the softness, important differences are noticed at high density, close to freezing. In particular, every system has a different pressure at fixed density, or at its own freezing point. Also, at low density (not shown in the figure), the pressure increases weakly with the softness, whereas it decreases at high densities.

3.2.1 Mapping different potentials

Contrary to other works, we will not try to rationalise the complex picture presented in figure 3.2 with the so-called *effective diameter* [6, 26], mapping the pressure to the hard-sphere one, or other theoretical approximations [46], but will show that a convincing scaling of the data can be performed using the freezing density, showing that the hard sphere limit can be reached within this scaling, for n as low as $n \approx 24$. In the upper panel of figure 3.3

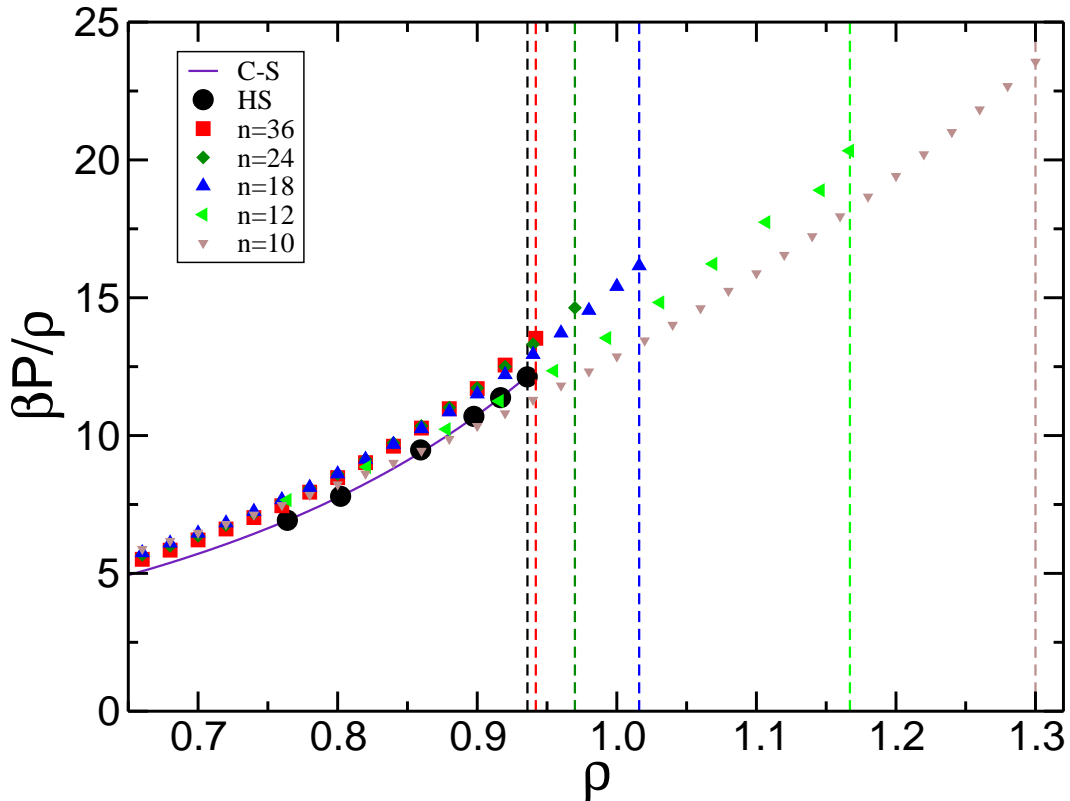


Figure 3.2. Pressure of the different systems studied here, as labelled, and Carnahan-Starling equation (magenta line). The vertical dashed lines indicate the freezing densities from Agrawal and Kofke [2].

we present the pressure as a function of the scaled Γ . A monotonous trend in the behaviour of pressure and potential softness is now evident at all shown densities.

In the lower panel, the pressure has been scaled with the value at freezing, showing almost perfect collapse of the data for $n \geq 18$. The inset presents the scaling factor and the ratio of the second virial coefficient to the hard sphere value, as a function of the potential softness. These two quantities disagree, showing that a mapping based on the second virial coefficient would not find such a good scaling, concluding that soft spheres behave as hard ones only for very large values of n . The a priori surprising finding emerges, that a scaling of soft spheres onto hard ones works better at high densities, where the closeness to freezing provides a common scaling variable, which collapses the data much better than the second virial coefficient would.

The scaling observed in figure 3.3, in contrast with the complex situation observed in figure 3.2, indicates that the relevant length scale for thermodynamic properties is not σ , but the average particle separation, $\Gamma^{-1/3} = \rho^{-1/3}/\sigma$.

3.2.2 Local structure

This can be observed in the structure of the system, which can be scaled for different states and systems when $\rho^{-1/3}$ is used as the unit of distance. In figure 3.4, the pair distribution function is presented for the freezing density at every softness. The inset shows the raw data with distance measured in units of σ , where the maxima are shifted to lower distances

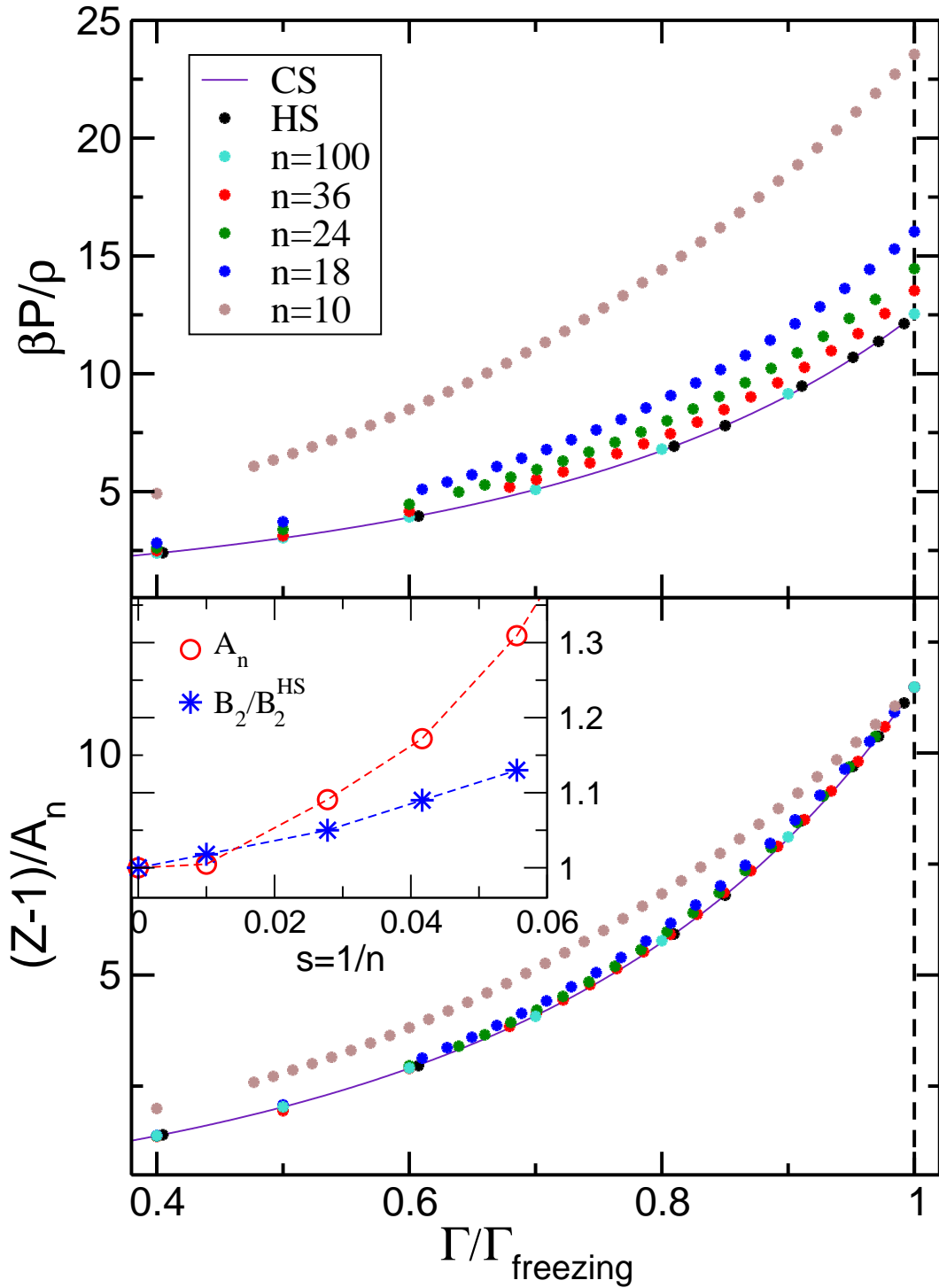


Figure 3.3. Upper panel: Pressure as a function of the scaled density for different potential softness, as labelled, and Carnahan-Starling equation (magenta line). Lower panel: Scaled pressure vs. scaled density for the same values of n . The inset shows the scaling factor for the pressure (red circles) and the ratio of second virial coefficients to the hard sphere system (blue asterisks) for different n .

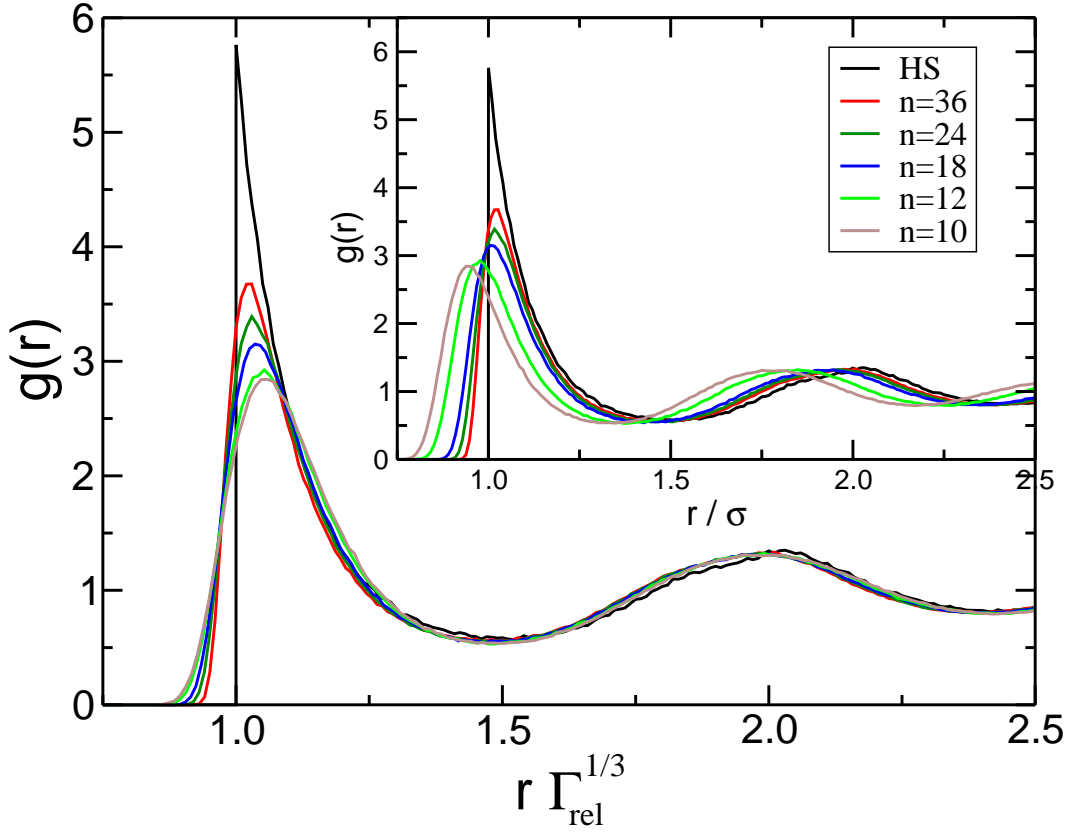


Figure 3.4. Pair distribution function of the soft and hard spheres at freezing (see table I), for different softness: from top to bottom in the nearest neighbour peak HS, $n = 36$, $n = 24$, $n = 18$, $n = 12$ and $n = 10$. The inset shows the raw distribution as a function of the average distance measured in units of σ , and the main panel in units of $\rho^{-1/3}$ (the hard sphere system has been left unchanged).

for higher n , and the main panel presents $g(r)$ with the distance scaled with the mean interparticle distance, where scaling has been achieved for all peaks (in order to keep the first neighbour peak in hard spheres at $r = \sigma$, distances have been scaled not simply by $\Gamma^{-1/3}$, but by $\Gamma_{\text{rel}}^{-1/3} = (\Gamma/\Gamma^{\text{HS}})^{-1/3}$, where Γ^{HS} denotes the hard sphere value of Γ at freezing). Differences in the local structure are still observed in the first neighbour peak, caused by the differences in the potential softness, and these are responsible for the differences observed in the pressure (figure 3.3 – upper panel).

The relevance of the interparticle distance in contrast to σ for structural properties, can also be shown using the structure factor, which is more accessible experimentally than the pair distribution function. Figure 3.5 presents the structure, $S(q)$, as a function of the wave vector scaled with the inverse separation distance $\rho^{1/3}$ at freezing for different potential softness. The inset shows the neighbour peak in more detail, where the differences in the local structure are noticed. As expected from the Hansen-Verlet criterion [24], the height of the peak is around 2.85 in all cases. This shows that all systems in the range of softness studied have similar liquid structure (except locally) at their freezing points and that the scaling factor is the mean interparticle distance, thus establishing the density that must be used to match the thermodynamic quantities in systems with different softnesses.

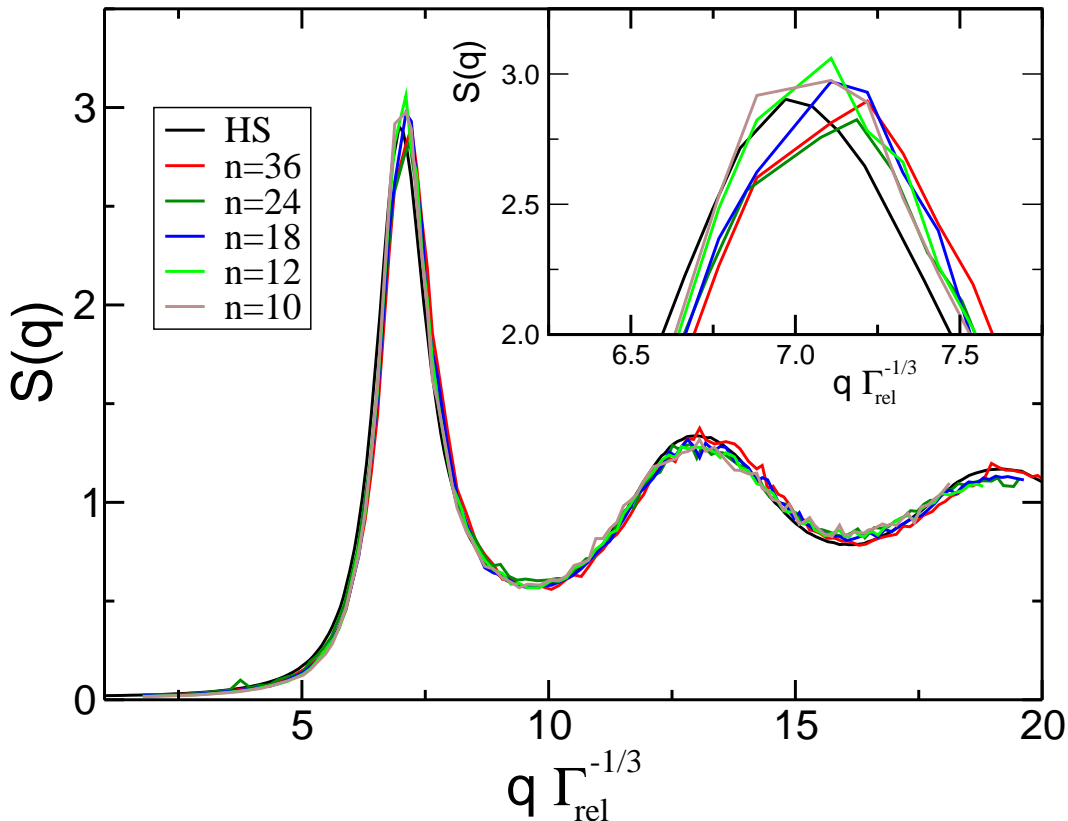


Figure 3.5. Structure factor of the soft and hard spheres at freezing (see table I), with the same colour code as figure 3.4. The wave vector has been scaled with the inverse average distance $\rho^{1/3}$ (the hard sphere $S(q)$ has been left unchanged). The inset shows the neighbour peak in detail.

3.2.3 Dynamics

We move now to the study of dynamic quantities, particularly the transport coefficients (diffusion coefficient and the shear viscosity) and the autocorrelation functions involved in their calculations. The diffusion coefficient, D , can be obtained via the Green-Kubo relation from the velocity autocorrelation function, or from the long time slope of the mean squared displacement[25], $\langle \delta r^2 \rangle$:

$$D = \int_0^\infty C_v(t) dt = \lim_{t \rightarrow \infty} \frac{\langle \delta r^2(t) \rangle}{6t} \quad (3.3)$$

where $C_v(t) = 1/3 \langle \mathbf{v}_i(t) \cdot \mathbf{v}_i(0) \rangle$, while $\delta \mathbf{r} = \mathbf{r}(t) - \mathbf{r}(0)$ and the brackets indicate ensemble and time-origin averaging. The velocity autocorrelation function is presented in figure 3.6 (upper panel), for soft spheres with Newtonian dynamics (ND) and damped Newtonian dynamics (dND) at the freezing point for every system. $C_v(t)$ decays faster for damped dynamics, due to the random forces and friction with the solvent, resulting in a diffusion coefficient lower than what pure Newtonian dynamics yields. (The presence of backwards motion indicates that the Brownian forces are not strong enough to provoke the decorrelation of velocities before collisions occur). Because the local environment of the particles is different for the different systems, the $C_v(t)$ functions do not coincide in the decay and at the backscattering minimum, which is deeper for softer potentials. These differences

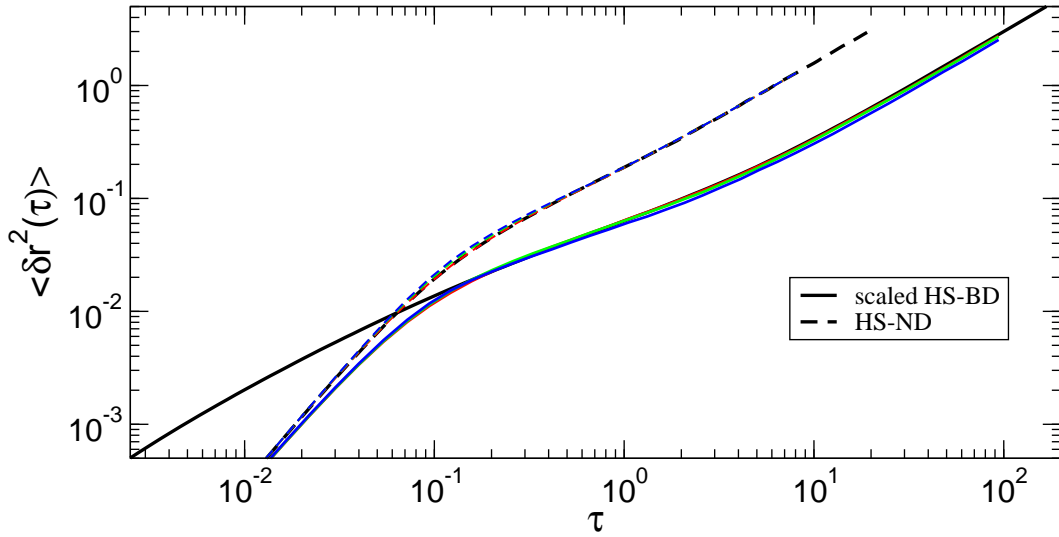


Figure 3.6. The mean squared displacement for different dynamics: dashed lines show Newtonian while solid lines depict the Brownian and damped dynamics. The solid set of curves has been used to find a mapping of the timescales between damped and Brownian dynamics by insisting on the long time diffusion to be equal — for this reason the hard spheres have been scaled by a factor $\tau_D = 0.1132$ on the time axis.

however concur to give equal diffusion coefficients for different particle softness, as shown below in figure 3.7.

The mean squared displacement (MSD) is plotted in the lower panel of the figure for soft spheres with ND and dND and for hard spheres with ND and Brownian dynamics (BD). Due to the Brownian forces (in dND), or kicks (in Brownian dynamics), the MSD grows slower for dND or BD than for ND. (The short time dynamics for hard spheres with BD is controlled by the arbitrary time interval between Brownian kicks, τ_B , and the MSD in this case has been shifted in time to give the same long time self diffusion coefficient). Note that the MSD with the same microscopic dynamics collapse independently of n (except for hard spheres with BD), even though the density is rather different. The velocity autocorrelation functions did not collapse because this function focuses on the microscopic dynamics where the local structure is sampled, although the final diffusion coefficient is identical for all potentials. The scaling in MSD and the concomitant agreement of diffusion coefficients, indicates again that the relevant quantity for this transport coefficient is the distance to freezing, instead of the density.

The diffusion coefficient from the long time limit of the MSD with ND for the different potentials is presented in figure 3.7 as a function of the density (upper panel) and as a function of $\Gamma/\Gamma_{\text{freezing}}$ (lower panel). The raw data shows differences due to the softness of the potential up to $n = 36$ (upper panel) in agreement with previous results [28], although the value of the diffusion coefficient at the freezing point is very similar in all cases, as expected from the dynamic criterion for freezing proposed by Löwen et al. [36]². When the diffusion coefficient is plotted against $\Gamma/\Gamma_{\text{freezing}}$, a convincing collapse of the data is found for $n \geq 24$, with small deviations for $n = 18$ (lower panel). The same scaling that was used to rationalise the structural and thermodynamic properties is successful in the collapse of

²Note, however, that a short-time diffusion coefficient cannot be defined for ND.

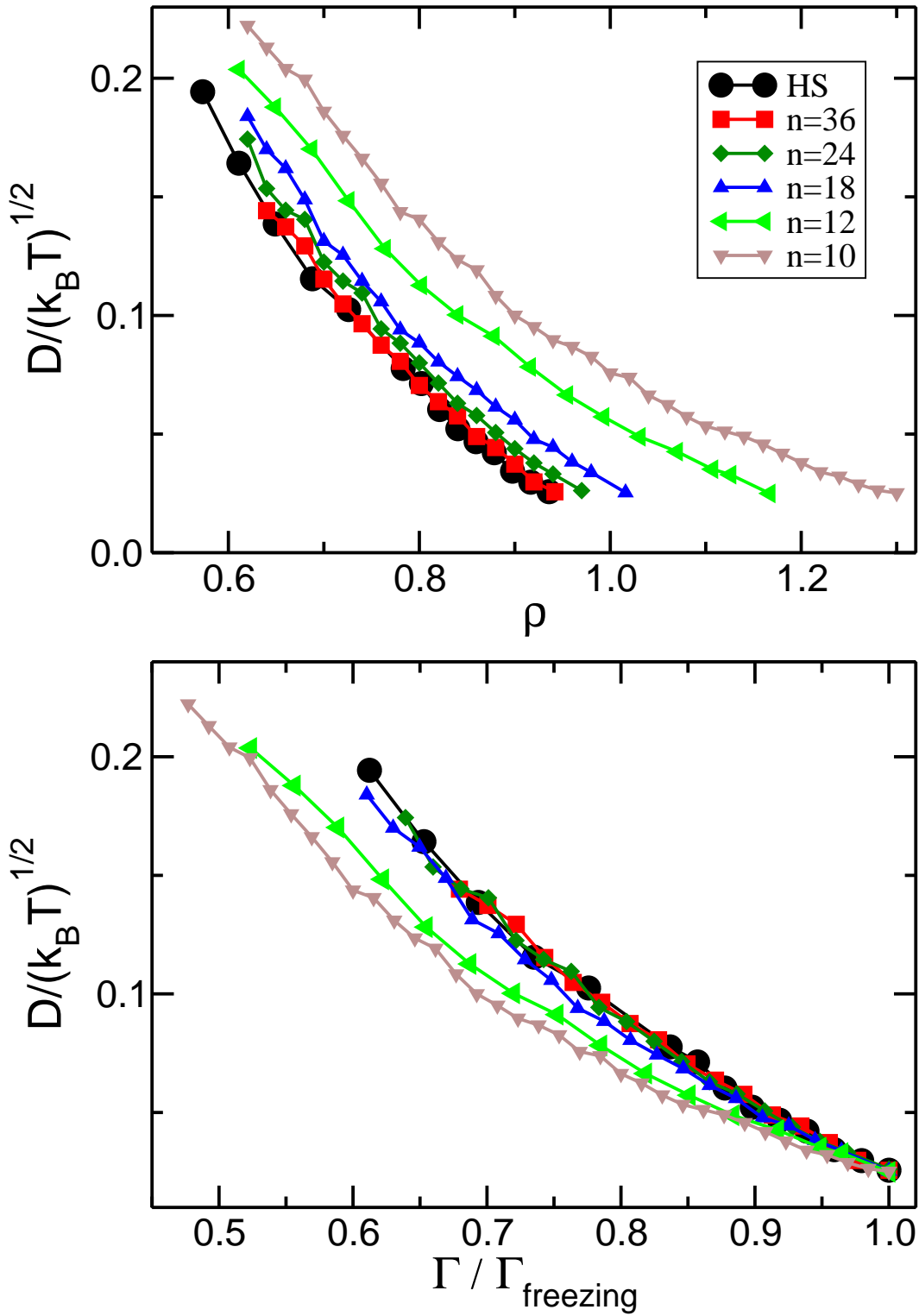


Figure 3.7. Diffusion coefficient for increasing density approaching the freezing transition for soft spheres with different softness and hard spheres, as a function of the density, ρ (upper panel) and the scaled density, $\Gamma/\Gamma_{\text{freezing}}$ (lower panel). From top to bottom in the upper panel (bottom to top in the lower one): $n = 10$, $n = 12$, $n = 18$, $n = 24$, $n = 36$ and hard spheres.

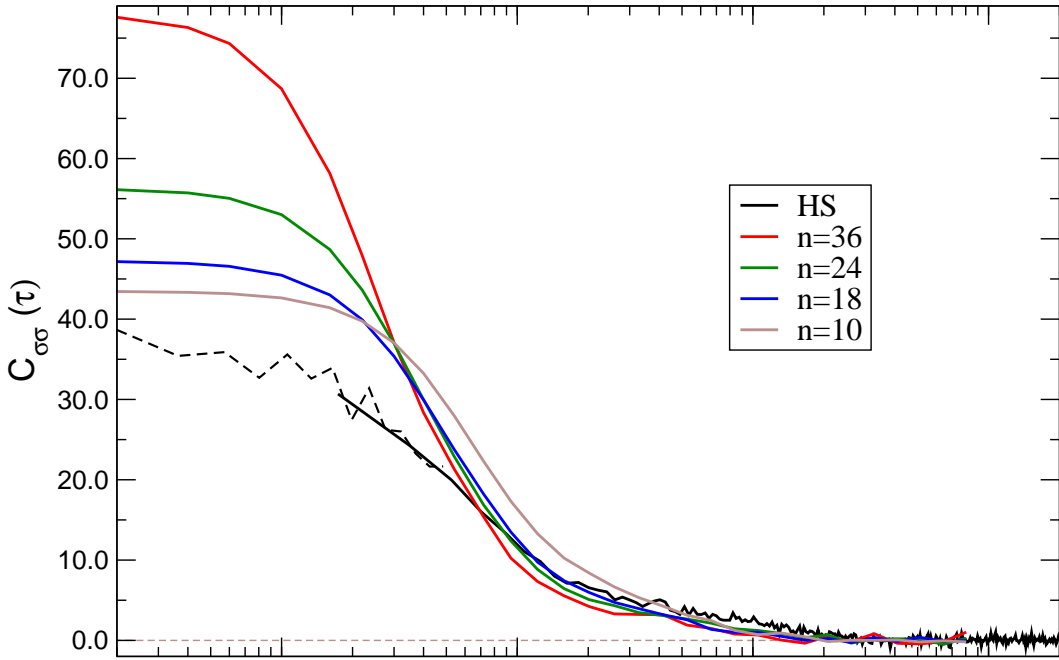


Figure 3.8. Stress correlation function at the freezing density for different potential softness with Newtonian dynamics. Dashed black line refers to simulations with $\tau_\sigma = 0.0017$ to probe shorter correlation times.

the diffusion coefficient. Similar collapse of the diffusion coefficient can be found using the BD or dND as short time dynamics.

3.2.4 Forces and viscosity

In a bid to probe the underlying forces we now turn to the viscosity of the system. The theoretical background on stresses in a hard sphere system is described in sections 4.4 and onwards. At this point it may suffice to quote the results. As a quantity collecting a good deal of the intricacies of the interparticle forces, we want to study the viscosity as calculated from the stress autocorrelation function, $C_{\sigma\sigma}(t)$. In general, the stress tensor is given as:

$$\sigma_{xy} = \frac{1}{V} \left(\sum_i m (v_i)_x (v_i)_y + \sum_{ij} (F_{ij})_x (r_{ij})_y \right). \quad (3.4)$$

where $(v_i)_x$ is the x -component of the velocity of particle i and $(F_{ij})_x$ is the x -component of the interaction force between particles i and j . $\langle \dots \rangle$ indicates an average over initial conditions. For hard spheres, however, the interaction potential is not differentiable, but the force can be found using the exchange of momentum between colliding particles[5, 21]. To this end one needs to average the change of momentum $(F_{ij})_x = m (\Delta v_{ij})_x \delta(t, t_{ij})$ during a brief time interval τ_σ , where the δ -function refers to the instantaneous change of momentum, which leads to

$$\sigma_{xy} = \frac{1}{V} \left\langle \sum_{i=1}^N m (v_i)_x (v_i)_y + \frac{1}{\tau_\sigma} \sum_{coll} (\Delta v_{ij})_x (r_{ij})_y \right\rangle, \quad (3.5)$$

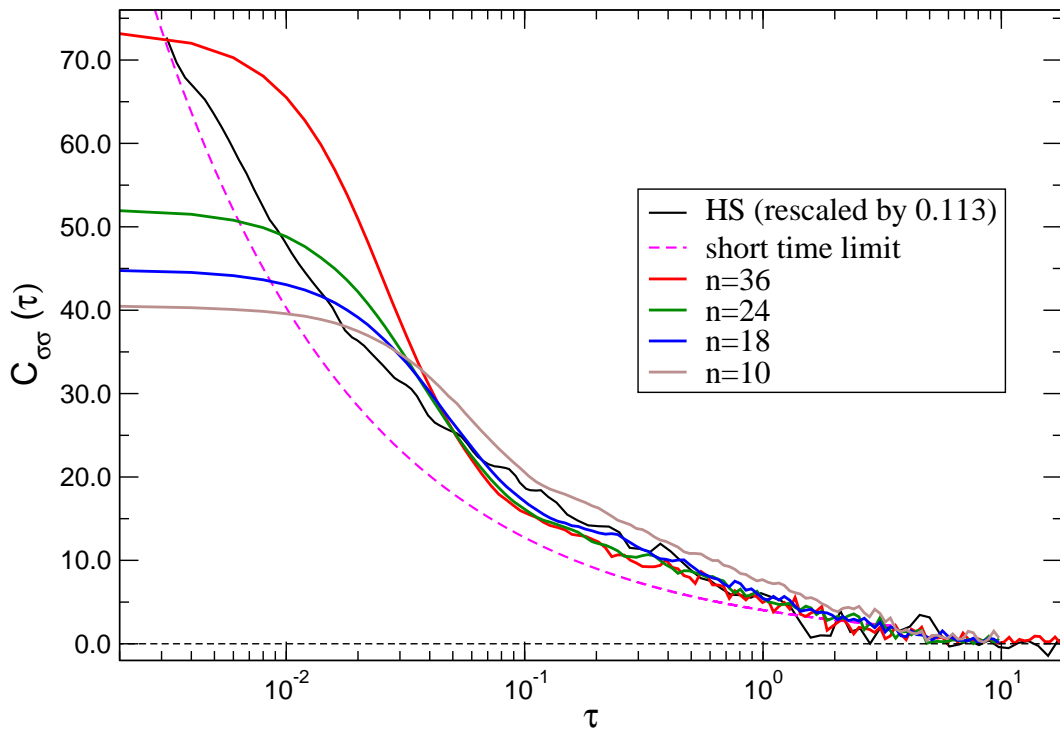


Figure 3.9. Stress correlation function at the freezing density for different potential softness with Brownian dynamics.

where the second summation now refers to all collisions within the time interval τ_σ . Unless otherwise stated $\tau_\sigma = 0.017$.

The stress correlation function, $C_{\sigma\sigma}(t) = 1/3 \sum_{x < z} \langle \sigma_{xy}(t) \sigma_{xy}(0) \rangle$, is presented in figure 3.9 for the hard and soft spheres with different softness at their freezing points, using Newtonian and Brownian or damped dynamics.

In both microscopic dynamics, differences are noticed in the correlation function at short time, in particular hard spheres show for Brownian as well as Newtonian dynamics their respective pathologies (see sections 4.4.4 and 4.5.2).

Nevertheless, hard and soft spheres collapse within the noise level at longer times (compared to the microscopic time scale) for $n \geq 24$. The curve for hard spheres with BD has been scaled in time by the same factor as the MSD (see figure 3.6, lower panel), and the collapse with soft spheres is observed for $\tau > 10^{-1}$, as in the MSD case.

The short time divergence of the hard spheres correlation function can be observed in figure 4.13.

The viscosity, long time plateaus in figure 4.15, are presented in figure 3.10 for hard and soft spheres with microscopic ND, as a function of $\Gamma/\Gamma_{\text{freezing}}$. The error bars are the standard deviation of the averaging.

Due to the noise of the data, the collapse is not as impressive as for previous quantities. Deviations are only noted beyond the noise level at high density, close to Γ_{freezing} , for $n = 10$. These results are compatible with the previous ones, in showing that the appropriate scaling of the thermodynamic quantities and transport coefficients is obtained when Γ is referred to its value at freezing, although definite proof is only obtained for previous quantities. We have included it here, because of its relevance to experiments in colloid science.

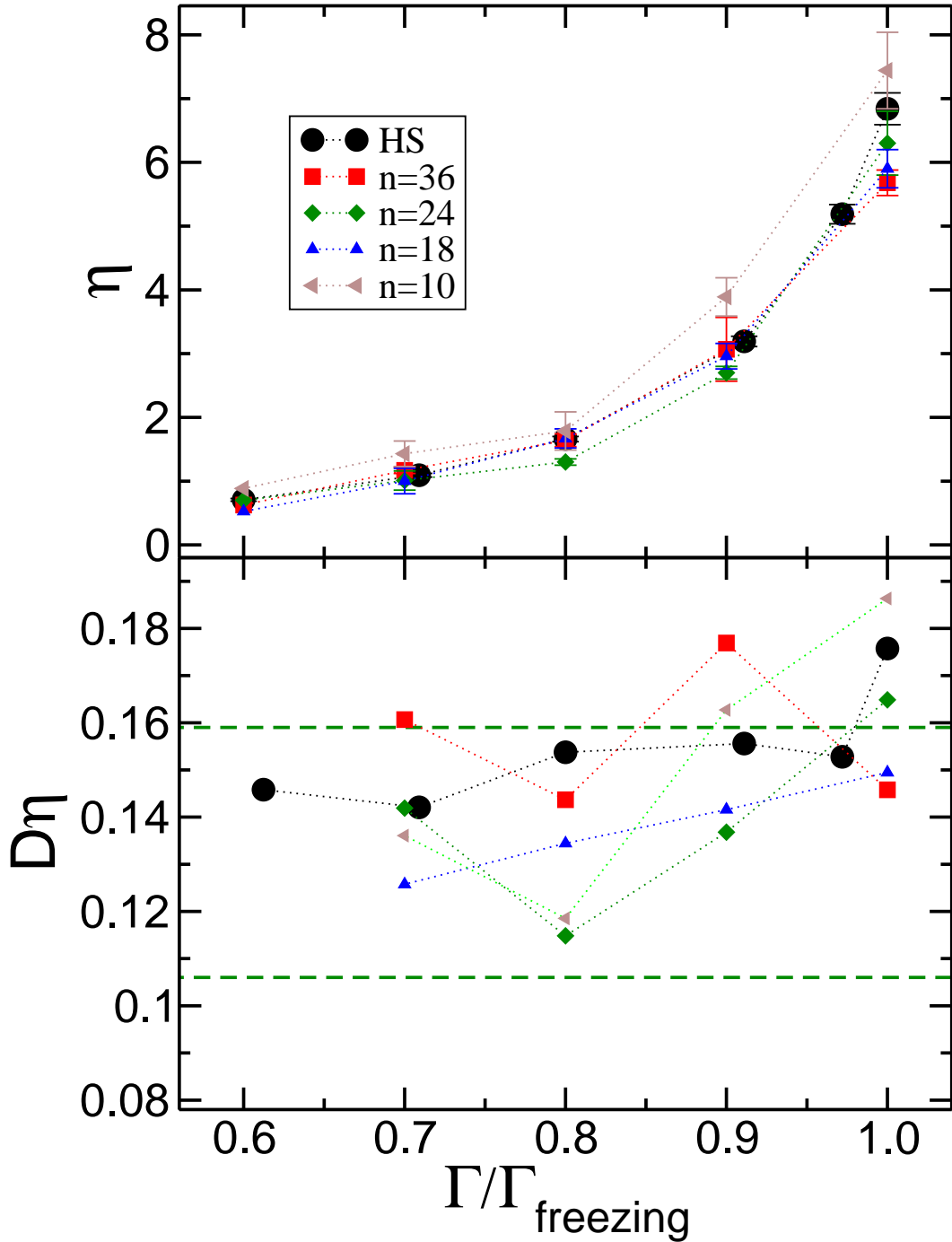


Figure 3.10. Viscosity of hard and soft spheres from the long time slope of the integrated stress, with microscopic ND (upper panel). Different potential softness is studied: black points, hard spheres; red ones, $n = 36$; green ones, $n = 24$; blue ones, $n = 18$; orange ones, $n = 10$. The lower panel shows the Stokes-Einstein relation $D\eta$, with the same colour code and the dashed green thick lines mark the slip value $1/(2\pi)$ (upper line) and stick value $1/(3\pi)$ (lower line).

The lower panel of the figure shows the product $D\eta$, which would be constant according to the Stokes-Einstein relation. Surprisingly, as this relation — derived from continuum fluid mechanics — need not apply to the present situation of the motion of a particle surrounded by a fluid of identical particles, within the noise level, this product is indeed constant and coincides with the theoretical value of Stokes' law for a sphere with a slippery surface $D\eta = (2\pi\sigma)^{-1}$ for $n = 36$.

3.3 Conclusions

We have considered in this section the structural and transport properties of hard and soft spheres of varying softness using simulations with different microscopic dynamics. The pressure and the transport coefficients can be rescaled onto the hard spheres values at high density when studied as a function of the density normalised to the freezing point for every system for $n \geq 18$, although they typically show non-monotonous behaviour for increasing density (or volume fraction), irrespective of the microscopic dynamics. Concomitantly, distances must be measured in units of the interparticle distance and all systems have the same long range structure at their freezing points. Differences due to the different softness are appreciable only in the local environment of the particles and at short times in the velocity and stress autocorrelation functions. The latter is particularly interesting since its value at zero-time depends on the particle softness and diverges for hard spheres. The analytical prediction at short times for the stress autocorrelation function of hard spheres and the initial δ -contribution to the viscosity have been verified quantitatively with our simulations. As expected, differences in the correlation functions are also noticeable depending on the microscopic dynamics used, although the final values of the transport coefficients are unaffected.

These results show that the key parameter for dense systems of hard and soft spheres is not the density, but the relative distance to the freezing point (which itself shows a non-monotonous behaviour with the softness of the potential) [33]. This can be of special interest for experimentalists, where a low softness cannot be ruled out, in particular in systems covered with surfactant layers, or in cases where the determination of the colloid density poses a major problem. Importantly, and perhaps at first counter intuitively, our simulations show that the mapping of a fluid of soft spheres onto one consisting of hard spheres becomes progressively better at higher densities and closer to freezing. This supports the idea, going back to van der Waals, that the local packing of a dense fluid is dominated by the rapidly varying repulsion which can successfully be modelled using hard spheres [6]. In these cases, our results indicate that the relevant quantity necessary for comparing different systems is not the bare density, but its ratio to the freezing density. In passing, we also note that this scaling is much simpler and more effective than other attempts to map the structure and dynamics of soft spheres onto those of hard spheres, based on effective hard-core diameters (insofar as the particle is not extremely soft, i.e. $n \geq 18$).

4

Analytic methods to mine the data

In this chapter we want to discuss what to do with all the data. Essentially what we have are sets of position coordinates of all particles at different points in times. The density on the time scale can be varied — and does vary hugely. There are, in fact, two fundamentally different approaches: on the one side the linear time scale that has a fixed time interval after which a configuration is saved. On the other hand, one can employ a logarithmic scale that has a varying time step. This is particularly useful when large timescales are probed and not all detail is needed.

Most of the analysis is done from the saved data sets. However, there are notable exceptions. For example, the stress tensor — we will deal with in section 4.4 — is calculated *on the fly* as we need more information about the simulation than is contained in snapshots.

4.1 Probing the structure

When we talk about the microscopic structure of a material, what we are concerned with are the physical positions of particles relative to each other. This emphasises immediately two vital ingredients for this discussion: we are dealing with averages, preferably ensemble averages and we are looking at more than one particle. Before we define the simplest such quantity, namely the *pair distribution function*, it is useful to define the concept of a local density.

$$\rho'(\mathbf{r}) = \sum_j \delta(\mathbf{r}, \mathbf{r}_j). \quad (4.1)$$

The ensemble average of this quantity, $\langle \rho \rangle$, takes on the meaning one is accustomed to, with values between one and zero. In a homogeneous material it is in fact equivalent to the average density N/V of the entire system. Neither of these definitions is particularly practical nor do they make much sense in the context of simulations with a number of particles of the order $N \approx 1000$, through the awkward fact that we almost never would find any particle just at the position \mathbf{r} . We have to resort to a slightly modified concept of what local means, which involves some small volume V around the position \mathbf{r} . So what we really mean when we talk of a local density is the preaveraged quantity:

$$\rho(\mathbf{r}) = \frac{1}{V} \int_V dV \sum_j \delta(\mathbf{r}, \mathbf{r}_j). \quad (4.2)$$

4.1.1 Radial distribution function

Also referred to as the *pair distribution function* or *pair correlation function*, it is a very sensitive measure of the local structure. It gives the relative probability of finding another

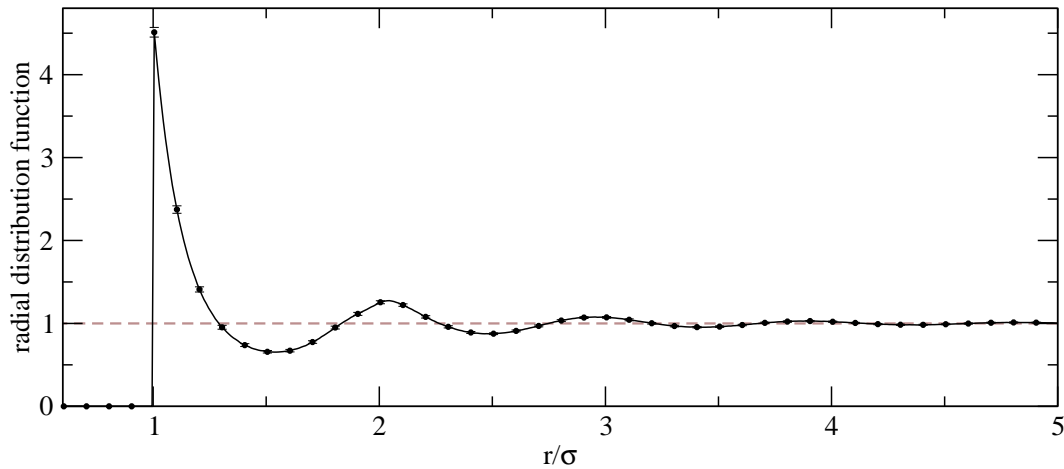


Figure 4.1. Radial distribution function of an isotropic system with Brownian motion at a packing fraction of $\phi = 0.450$. Characteristically the local order at close range decays to a structureless average density (normalised to one) at larger distances: this is the hallmark of amorphous matter.

particle at the distance r , given one particle is located at the origin. The definition follows directly from the pair correlation function:

$$\begin{aligned}
 \frac{1}{N} \int d\mathbf{r}' \langle \rho'(\mathbf{r}' + \mathbf{r}) \rho'(\mathbf{r}') \rangle &= \frac{1}{N} \int d\mathbf{r}' \left\langle \sum_j \delta(\mathbf{r}' + \mathbf{r}, \mathbf{r}_j) \sum_k \delta(\mathbf{r}', \mathbf{r}_k) \right\rangle, \\
 &= \frac{1}{N} \left\langle \sum_{jk} \delta(\mathbf{r}_k + \mathbf{r}, \mathbf{r}_j) \right\rangle, \\
 &= \frac{1}{N} \left\langle \sum_{j \neq k} \delta(\mathbf{r}, \mathbf{r}_{jk}) \right\rangle + \delta(\mathbf{r}, \mathbf{0}), \\
 &= \rho g(\mathbf{r}) + \delta(\mathbf{r}, \mathbf{0}).
 \end{aligned}$$

The angled brackets refer to the ensemble average, while $r_{jk} = r_j - r_k$. From this follows the definition of what is to be regarded as the pair distribution function:

$$g(\mathbf{r}) = \frac{1}{N\rho} \sum_{j \neq k} \delta(\mathbf{r}, \mathbf{r}_{jk}). \quad (4.3)$$

Again the number of particles usually is not big enough at one specific position to be able to determine such a local quantity well. The next step to improve the statistics is then to define a small volume around \mathbf{r} in which we consider $g(\mathbf{r})$ to be constant.

$$g(\mathbf{r}) = \frac{1}{V} \int dV \frac{1}{N\rho} \sum_{j \neq k} \delta(\mathbf{r}, \mathbf{r}_{jk}) = \frac{1}{NV\rho} \sum_{j \neq k} \int dV \delta(\mathbf{r}, \mathbf{r}_{jk}). \quad (4.4)$$

If symmetries are present in the fluid, one can exploit this by extending the volume as far as the symmetry would stretch. An example is the isotropy of the equilibrium fluid, where one can go a step further and actually gather all statistics from a spherical shell of some preferably small width. In this context the name *radial* distribution function has its merit.

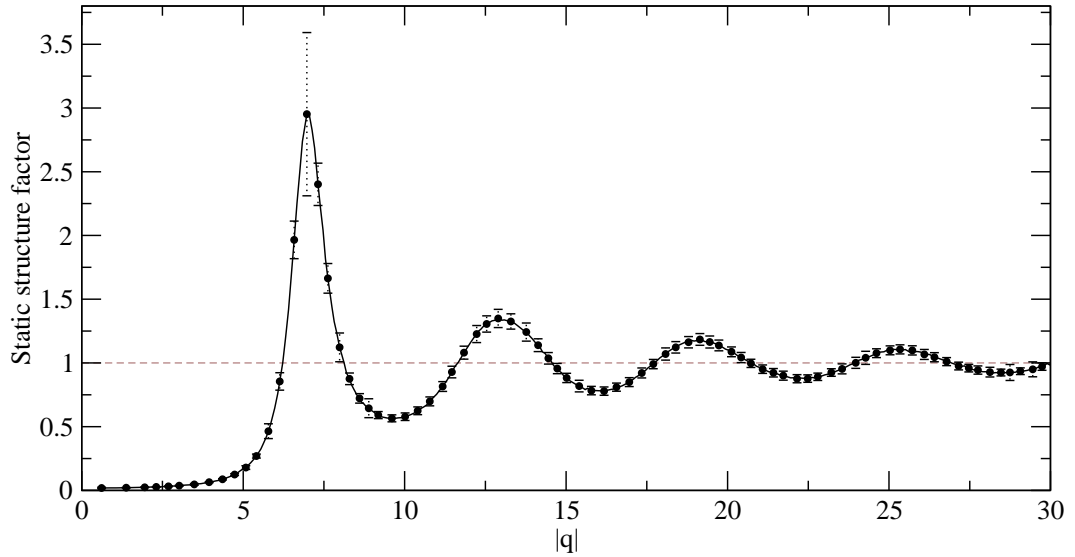


Figure 4.2. *Static structure factor of an isotropic fluid system with Brownian motion at a packing fraction of $\phi = 0.494$. Again, the fact that no long range order is present is reflected by the flattening out of the curve to an average value of one. The height of the first peak indicates the approach to freezing according to the Hansen-Verlet criterion [24]. Error bars show the standard deviation due to averaging over 500 sets.*

4.1.2 Static structure factor

By definition the static structure factor is related to the pair distribution function by the Fourier transform. One way of avoiding the pitfalls of the Fourier Transform is to apply it directly to the densities [25].

$$\rho(\mathbf{q}) = \int d\mathbf{r} e^{-i\mathbf{q}\cdot\mathbf{r}} \rho(\mathbf{r}) = \sum_j e^{-i\mathbf{q}\cdot\mathbf{r}_j}.$$

This leads directly to the definition of the static structure factor:

$$S(\mathbf{q}) = \frac{1}{N} \langle \rho(\mathbf{q}) \rho(-\mathbf{q}) \rangle, \quad (4.5)$$

$$= \left\langle \sum_{jk} \exp[i\mathbf{q}\cdot(\mathbf{r}_j - \mathbf{r}_k)] \right\rangle, \quad (4.6)$$

$$= 1 + (2\pi)^3 \rho \delta(\mathbf{q}, \mathbf{0}) + \int d\mathbf{r} e^{-i\mathbf{q}\cdot\mathbf{r}} (g(\mathbf{r}) - 1).$$

Notably the last line acquires additional terms and due to the fact that neither $g(\mathbf{r})$ nor $S(\mathbf{q})$ decay to zero, some care has to be taken when applying the Fourier transform to them. In any case, the additional δ -function will not be accessible to us as we have physical constraints on the smallest possible size of the q -vector: $q = 2\pi/L$, with L describing the physical length of the simulation box.

It is, however, equation (4.5) that we want to take a closer look at, with the computational aspects in mind. We can immediately see that equation (4.5) can be rewritten as

$$S(\mathbf{q}) = \frac{1}{N} \langle \rho(\mathbf{q}) \rho(-\mathbf{q}) \rangle = \frac{1}{N} \langle |\rho(\mathbf{q})|^2 \rangle. \quad (4.7)$$

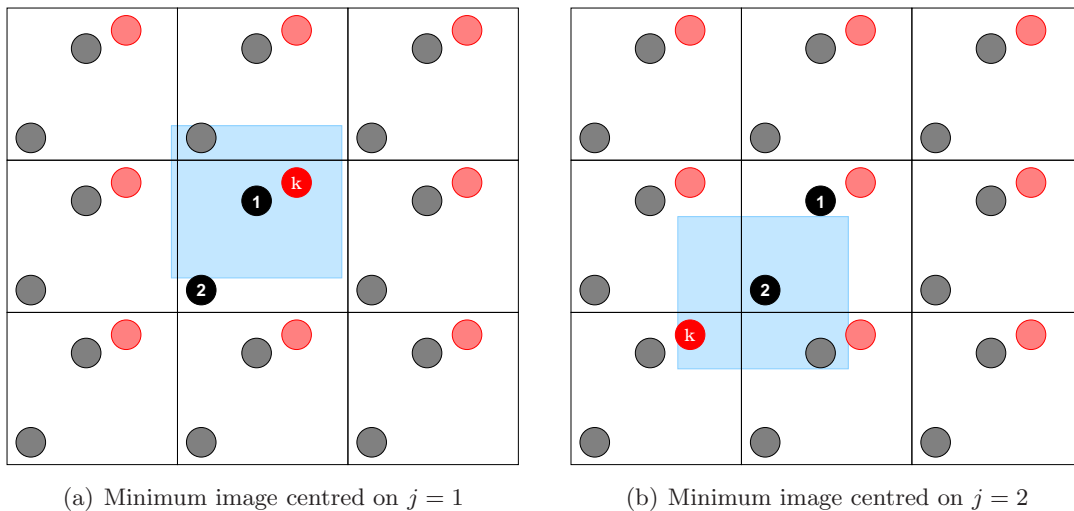


Figure 4.3. *The minimum image moves around different periodic copies of the original box, according to which particle it is centred on. In the process, the absolute coordinates of particle k depend on the position of particle j .*

As a consequence of this, the double sum has been contracted into the square of a single sum — a considerable saving when it comes to computing. A further computer-friendly modification is to rewrite the exponential function in terms of trigonometric functions, such that

$$\begin{aligned} \frac{1}{N} \langle |\rho(\mathbf{q})|^2 \rangle &= \frac{1}{N} \left\langle \left| \sum_j e^{-i\mathbf{q} \cdot \mathbf{r}_j} \right|^2 \right\rangle, \\ &= \frac{1}{N} \left\langle \left[\sum_j \cos(\mathbf{q} \cdot \mathbf{r}_j) \right]^2 + \left[\sum_j \sin(\mathbf{q} \cdot \mathbf{r}_j) \right]^2 \right\rangle. \end{aligned}$$

For future reference, it is worth noting that all this computational trickery hinges crucially on the assumption that the first step, as indicated in equation (4.7), is valid. Namely, this is the assertion that

$$\sum_j e^{-i\mathbf{q} \cdot \mathbf{r}_j} = \sum_k e^{-i\mathbf{q} \cdot \mathbf{r}_k}. \quad (4.8)$$

While this is obviously a true statement for a real system, the use of periodic boundary conditions in the simulation means that \mathbf{r}_k depends on \mathbf{r}_j and, as a result, both sums do not necessarily encase identical spatial coordinates. This is illustrated in figure 4.3, where the absolute coordinates of particle k are taken from different periodic images according to which minimum image is used. Which minimum image applies is in turn determined by the position of particle j . In this sense, the first sum over j may be distinct from the second over k in equation (4.8).

What comes to the rescue of the ordinary periodic boundary conditions, is the fact that the grid length is $q = 2\pi/L$ in any one direction. This convention enables the Fourier transform to take care of the minimum image automatically, as $r_k = nL + \Delta r_{min}$, where Δr_{min} denotes the shortest distance to any one of the image points as required by the

minimum image and n is an integer. In terms of the Fourier transform, this means

$$\begin{aligned} \exp\left(-i\frac{2\pi}{L}r_k\right) &= \exp\left(-i\frac{2\pi}{L}(nL + \Delta r_{min})\right), \\ &= \exp(-in2\pi) \exp\left(-i\frac{2\pi}{L}\Delta r_{min}\right), \\ &= \exp\left(-i\frac{2\pi}{L}\Delta r_{min}\right). \end{aligned}$$

This allows us to use the *wrong* coordinates that feature equal sums, without incurring a numerical error, but permitting us to take advantage of the reduction of the double sum to the square of the single sum. The reason for dwelling on this is that it becomes crucially important under shear (see section 5.2.3).

4.2 Time dependent quantities

The radial distribution and, likewise, its Fourier transformed cousin are capable of making the local structure visible. In equilibrium, this structure certainly fluctuates, but on average has a well defined form and does not depend on time in any way. Unless we go to non equilibrium there is no incentive to introduce time as a variable in any such quantity — on the contrary we exploit the fact that there is no time dependence to improve our statistics.

But even in equilibrium there are measures that naturally depend on time. One such quantity is the *mean squared displacement*.

4.2.1 Mean squared displacement

Physically, the square root of this function answers the question: how far does one particle get away from its original position in some time t . It is important to realise that the distance is a strictly positive quantity and can, in the worst case only, be zero. We have seen an example of this function in figure 2.1, where it is immediately clear that such a plot betrays a great deal about the way a particle typically moves within the system — in short: it probes the *dynamics*.

Theoretically, there is no more to it than what is already given away in equation (2.1), which reads thus for a three dimensional system,

$$\langle \Delta r(t)^2 \rangle = \langle (\mathbf{r}(t) - \mathbf{r}(0))^2 \rangle. \quad (4.9)$$

A difficulty in calculating the mean squared displacement arises from the application of periodic boundary conditions. At its heart lies the fact that our simulation box is a peculiar construction that conserves the number of particles, although the colloids float in and out of the box freely. Since the displacements are what we are concerned with, we are forced to consider positions (and strictly speaking that means colloids) beyond the limits of our simulation box. It becomes clear then that we can only calculate the distance one particular colloid has travelled from where it was at time t_0 in figure 4.5, to where it is at t_1 , if we know for which image to calculate the distance Δr . This simply requires keeping track of the number of times a particle has left or entered the box.

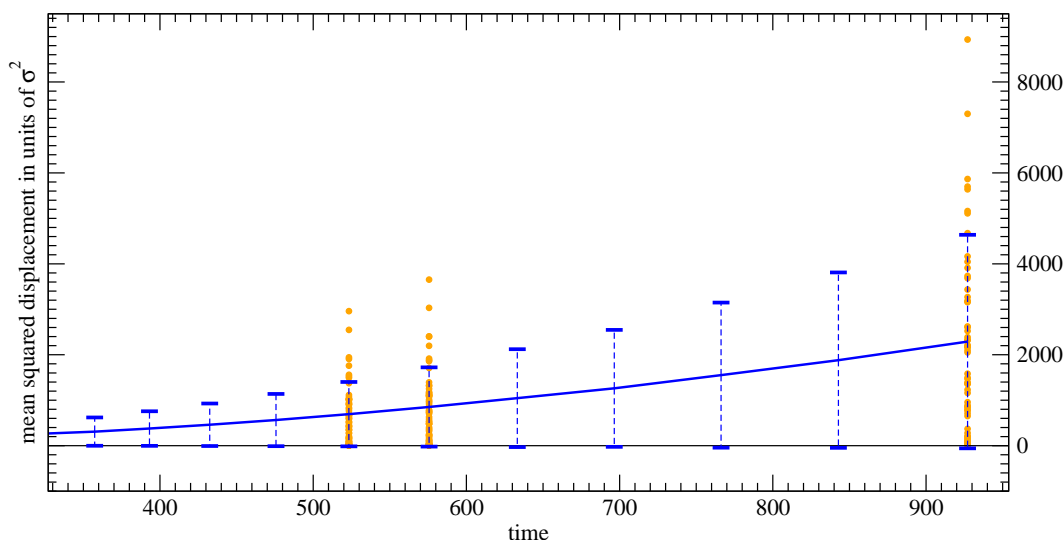


Figure 4.4. On the level of individual trajectories the spread of outcomes is large: some have literally not moved at all, while others have travelled more than twice as far as the typical means squared displacement would suggest (orange dots). This is also reflected in the standard deviation (error bars). The system plotted is a standard binary mix at a packing fraction of $\phi = 0.52$ with only 64 particles.

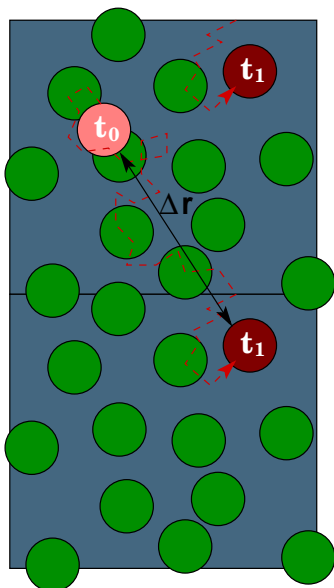


Figure 4.5. Displacements may go beyond the box.

This is particularly bothersome when shear is introduced. We deal with this in section 5.2.2.

The mean squared displacement is also a good example of a function that is amenable to the use of a logarithmic timescale. Clearly we are not interested in the same level of detail along the entire mean squared displacement as presented in figure 2.1. A logarithmic time scale reduces significantly the amount of data to be handled.

Where we, on the other hand, can not be stingy is when it comes to statistics. On the level of individual paths, the performance of colloids is extremely varied. This is illustrated in figure 4.4 where we see the mean squared displacement at an advanced stage where diffusion already commands a dominant role. Nevertheless, there are particles that virtually have not moved, or others that have managed to travel more than twice as far as the average. This spread is made visible by the orange dots marking the actual values of the different displacements. This is also reflected in the error bars giving the average deviation.

Being a single particle quantity, every one of the particles in the simulation serves as a sample and the mean squared displacement converges relatively quickly to a stable curve.

4.2.2 Density-density correlation function

Another example of such a statistics friendly function is the incoherent part of the density-density correlation function. This is in stark contrast to the coherent part, which requires all particles for a single result — and is a prime example of a *collective* quantity. From the

outset this makes it much harder to attain a decent amount of statistics.

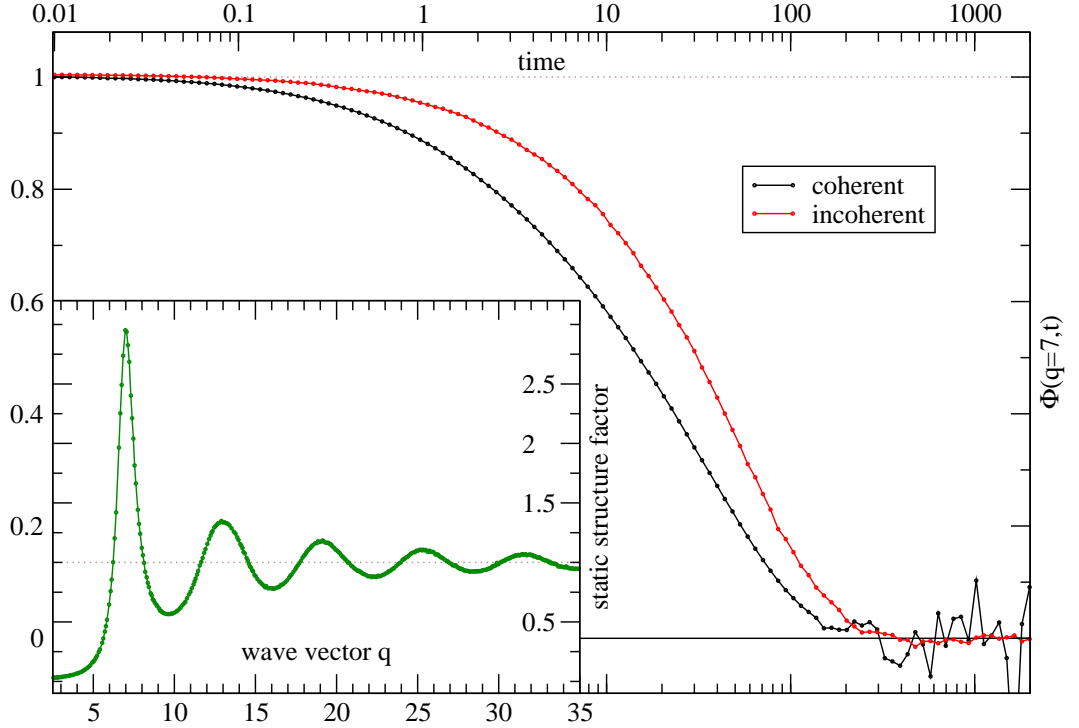


Figure 4.6. Coherent and incoherent parts of the dynamic structure factor. Clearly visible here are the different qualities in terms of statistical smoothness due to the distinct character of both curves. Depicted is a standard system at $\phi = 0.494$, with $\tau_B = 0.01$ at $q = 7$ corresponding to the first peak of the static structure factor $S(q)$ for this system. The inset shows the $S(q)$ for this system. The coherent part is normalised by the static structure factor.

The theory follows from an extension of the definition of the static structure factor as given in equation (4.5): we introduce the additional dimension of time.

$$C_{\rho\rho}(\mathbf{q}, t) = \frac{1}{N} \langle \rho(\mathbf{q}, t) \rho(-\mathbf{q}, 0) \rangle. \quad (4.10)$$

The wave vector \mathbf{q} is now confined to a subscript to indicate the common practise for examining the density-density correlation function $C_{\rho\rho}(\mathbf{q}, t)$ as a simple function of time at one particular value of \mathbf{q} , which makes the name *dynamic* structure factor a plausible choice. Expanding the expression using the definition of the density (equation (4.1)), we find

$$C_{\rho\rho}(\mathbf{q}, t) = \frac{1}{N} \left\langle \sum_j \exp[-i(\mathbf{q} \cdot \mathbf{r}_j(t))] \sum_k \exp[i(\mathbf{q} \cdot \mathbf{r}_k(0))] \right\rangle, \quad (4.11)$$

which naturally falls into two parts. On the one hand when $j = k$, we have the *incoherent* or *self* part of the dynamic structure factor, while all other terms with $j \neq k$ are summarised under the label *coherent* or *distinct*.

$$C_{\rho\rho}(\mathbf{q}, t) = \frac{1}{N} \left\langle \sum_j \exp[-i(\mathbf{q} \cdot (\mathbf{r}_j(t) - \mathbf{r}_j(0)))] + \sum_{j \neq k} \exp[i(\mathbf{q} \cdot (\mathbf{r}_j(t) - \mathbf{r}_k(0)))] \right\rangle. \quad (4.12)$$

As the limit of $t \rightarrow 0$ in the incoherent part takes us back to the definition of the static structure factor, we can normalise the correlation function by the value of $S(q)$ at the chosen value of q .

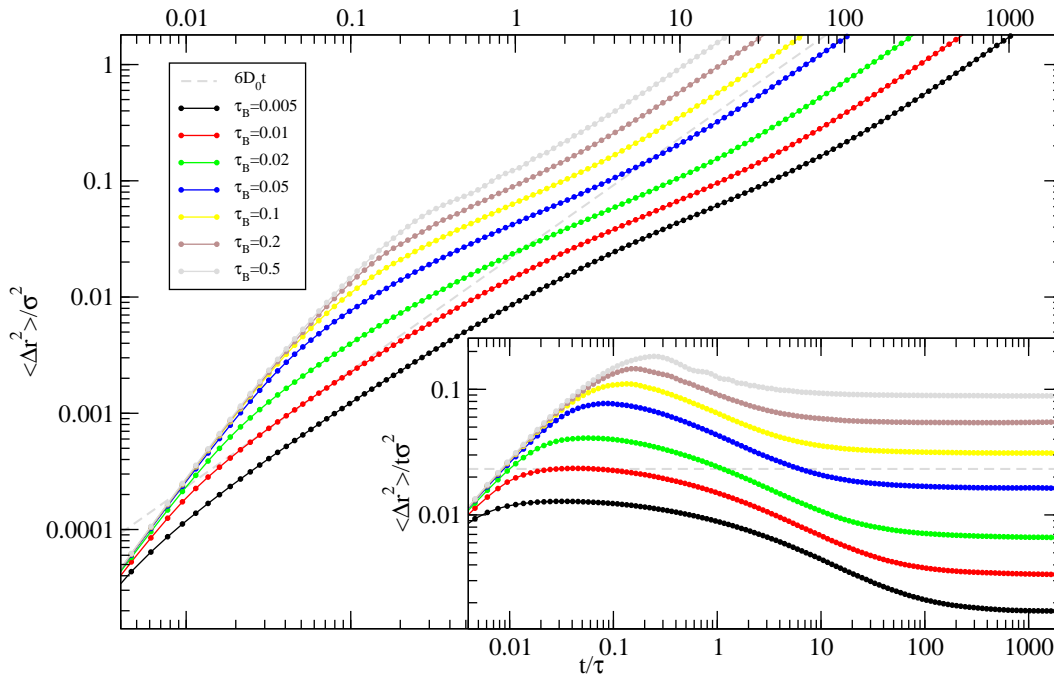


Figure 4.7. *The influence of τ_B on the mean squared displacement. The system of 1000 particles close to freezing displays how the diffusion due to Brownian motion can almost disappear in the randomisation due to the inter-particle collisions. The grey dashed line indicates what diffusion ought to look like for what we chose to be the standard system, with $\tau_B = 0.01$. For the inset, the same data has been divided by time to show more clearly the separation of the two different types of diffusion.*

4.3 Brownian motion of hard spheres revisited

We must return to the topic of Brownian motion at this point in order to discuss the defining parameter τ_B . When we introduced the algorithm we saw, that this parameter tunes the level of Brownian motion. We have not so far addressed the question of what level might be considered appropriate. From the historical origin of Brownian motion we obtain the vital clue: the salient feature of such erratically driven movement is that it leads on average to diffusion. For the limit $t \rightarrow \infty^1$, the Langevin equation of single particle gives

$$\langle (\mathbf{r}(t) - \mathbf{r}(0))^2 \rangle \approx \frac{6k_B T}{3\pi\eta_0\sigma} t = 6D_0 t. \quad (4.13)$$

In order to call the dynamics Brownian, τ_B should take a value that makes diffusion the dominant mode of movement. As the only other parameter in the simulation is the packing fraction ϕ , it is, crudely speaking, a question of weighing τ_B against ϕ . The packing fraction determines the average free path of the particle between collisions. The aim would be to set the Brownian time step, τ_B , to such a level that diffusion is already apparent between collisions. At the other extreme the performance of the code is keeping us from driving τ_B to zero.

All this can be observed in the mean squared displacement (figure 4.7). At very short times ballistic motion is visible. Then the Brownian motion sets in. Since our Brownian

¹Technically of course I don't need the time to extend to infinity, but $t \gg m/\zeta$ is enough. ζ is the friction coefficient found in the Langevin Equation

kicks are a concerted action, the transition to diffusive motion comes in waves. These waves are visible at the timescale of τ_B , but as we go to longer times the effect is washed out and we are left with the desired diffusive motion. In figure 4.8, the mean squared displacement of the standard system at freezing illustrates this.

As in our system the short time diffusion coefficient, D_0 , is equivalent to the single particle self diffusion and we can directly connect D_0 to τ_B . In order to show this we need to go to large times compared to τ_B . For convenience let us assume that $t = n\tau_B$, with n some large integer and note

$$(r(t) - r(0)) = \Delta r(t) = \int_0^t dt v(t) = \sum_i^n v_i(t)\tau_B.$$

We can now use this and the observation that $\langle v_i v_j \rangle = 0$ to calculate the mean squared displacement.

$$\begin{aligned} \langle (\Delta r(t))^2 \rangle &= \left\langle \left(\sum_i^n v_i(t)\tau_B \right)^2 \right\rangle, \\ &= \tau_B^2 \sum_i^n \langle v_i^2(t) \rangle = \tau_B^2 \sum_i^n 3k_B T, \\ 6D_0 n\tau_B &= 3n\tau_B^2 k_B T, \quad \Leftrightarrow \\ D_0 &= \frac{\tau_B k_B T}{2} \end{aligned} \tag{4.14}$$

This relationship is useful to determine whether the Brownian motion is *Brownian* enough. Figure 4.9 elucidates what happens when collisions interfere in what appears to be short time diffusion. As an example: at $\tau_B = 0.1$ (red), the system of figure 4.9 still appears to show two distinct diffusive regimes. However, their separation is already diminished, as can be seen in the inset — too many collisions contaminate what seems to be short time diffusion.

This ties in with what we discussed in section 2.1, where we found that the algorithm works best within the limit where the random displacement is small compared to the mean free path. It was within that limit that the multi-particle problem dissolved into a string of binary collisions, with the added benefit that we know how to handle these correctly. Up to freezing, we found $\tau_B = 0.01$ to be a good compromise between performance and Brownianness.

4.4 The stress tensor

The derivation of microscopic expressions for the forces appearing in macroscopic (and mostly phenomenological) equations of hydrodynamics has been described by Irving and

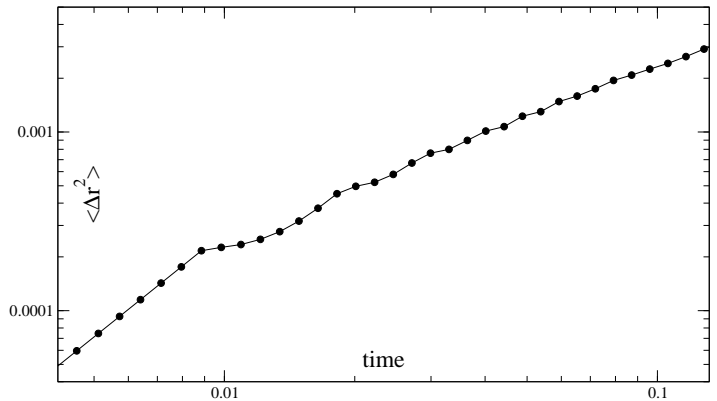


Figure 4.8. Mean squared displacement: Transition from ballistic to diffusive motion.

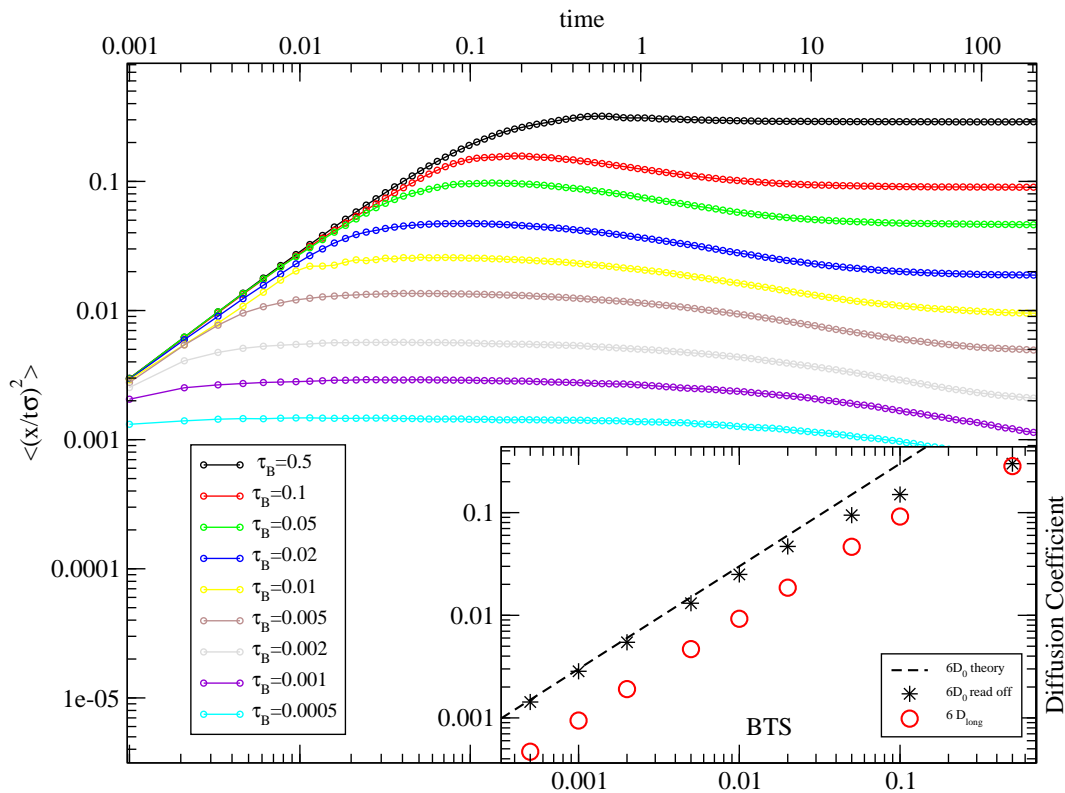


Figure 4.9. At a packing fraction of $\phi = 0.395$, the standard system illustrates the fact that it becomes increasingly difficult to read off an accurate value for the diffusion coefficient as τ_B becomes large. Here the mean squared displacement has been divided by time to show the two levels of diffusion more clearly. The first and upper level corresponds to the short time diffusion, while the later and lower levels mark the long time diffusion. The inset shows both plateau values, as well as the theoretical result for short time diffusion (dashed line).

Kirkwood [30]. The basic idea is to compare the continuity equation for momentum flux,

$$\frac{\partial}{\partial t}(\rho \mathbf{u}) + \nabla(\rho \mathbf{u} \mathbf{u}) = \nabla \sigma + \frac{\mathbf{F}_{\text{ex}}}{V},$$

with the outcome of treatment on the discrete particle level employing statistical mechanics. Here \mathbf{u} is the local fluid velocity, defined as:

$$\mathbf{u}(\mathbf{r}) = \left\langle \frac{1}{\rho(\mathbf{r})} \sum_i \mathbf{v}_i \delta(\mathbf{r}, \mathbf{r}_i) \right\rangle, \quad (4.15)$$

where ρ is the number density. Following this procedure, it is possible to identify the stress tensor as having the form,

$$\sigma_{xy} = \frac{1}{V} \left(\sum_i m (v_i - u_i)_x (v_i - u_i)_y + \sum_{ij} (F_{ij})_x (r_{ij})_y \right). \quad (4.16)$$

This expression relies on the truncation of a Taylor expansion under the assumption that the pair-distribution function only varies slowly in the box. In the case of a fluid in equilibrium, this is certainly true and, quite conveniently, the local fluid velocity $\mathbf{u} = 0$. The first term

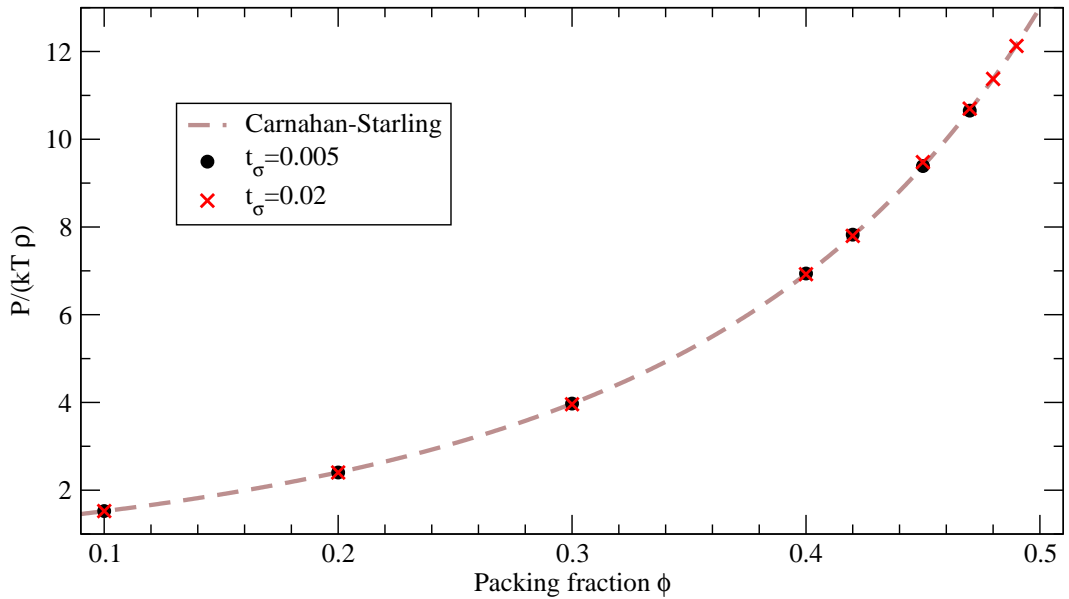


Figure 4.10. Comparing the mean of the diagonal entries of the stress tensor with the Carnahan-Starling result for the pressure. The time window τ_σ — during which the collisions have been averaged to give the potential part of the stress tensor — does not influence the value of the pressure easily.

on the right is referred to as the *kinetic* term. The diagonal entries are determined by the kinetic energy and reflect the pressure. In the isotropic case of the fluid in equilibrium we can compare this to well established theoretical results by Carnahan and Starling [12] (see figure 4.10).

The off-diagonal entries are on average zero. On the whole, the kinetic term is therefore proportional to $k_B T$ and, as a constant, of no further interest.

More interesting and dominant in the case of fluids is the second sum. It is due to the interaction of the colloids and generally referred to as *potential* term.

4.4.1 Calculating potential forces for hard spheres

As it were, the key observations are already written down in equation (4.16). It might be worth noting that we have tacitly introduced σ_{xy} as a non-local quantity. While this is certainly not generally true, it is a sensible idea in the systems we will investigate. In equilibrium a fluid should be blatantly isotropic, but under shear the stress tensor might inform you that it does matter in which direction you look — but at least it does not matter where you do so. Within the simulation box, a small volume should experience the same stress at any position². And by extension any small sample is just as good as the whole simulation box. To hone the point: instead of dealing with a small volume, one might as well take the whole lot. This is helpful in gathering whatever meagre statistics there is to be had. And, possibly stretching the point a bit, the average over the volume takes the role of the ensemble average.

That said, let us return to the minute volume and the idea of the momentum flux in order to understand what the potential term describes. In this picture we are led to think

² Provided, of course, it is orientated the same way.

about forces of particles across a given surface (see figure 4.11). While it is intuitively clear what this means when a potential can be used to calculate the force $\mathbf{F} = -\frac{\partial}{\partial \mathbf{r}}V(r)$, the case of hard spheres demands a more elaborate treatment — the consequences of which will be the subject of a number of pages to come.

In the case of a continuous potential, two particles feel a force mediated by some field at any place and time. The fact that hard spheres notice nothing of their neighbours does not mean that there is no force: in an elastic collision, repulsive forces manifest themselves vigorously — in fact the forces are infinite.

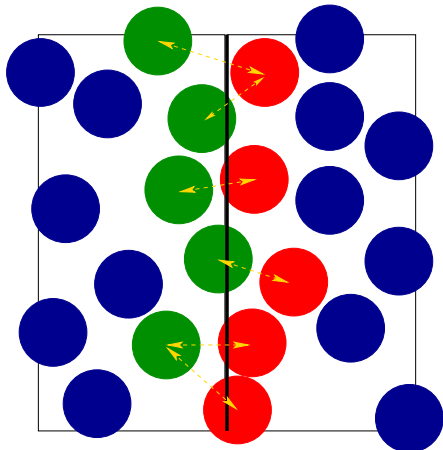


Figure 4.11. *Hard sphere forces across a boundary are due to collisions.*

over³, one can not expect to find a collision happening at one particular point in time: one has to define a small time window, τ_σ , over which to average. Hence, what we really mean when we write $\sigma_{xy}(t)$ is,

$$\sigma_{xy}^{\tau_\sigma}(t) = \frac{1}{V} \left(\sum_i m (v_i(t))_x (v_i(t))_y + \frac{1}{\tau_\sigma} \int_{-\tau_\sigma}^0 \sum_{ij} (F_{ij})_x (r_{ij})_y \right).$$

The first sum is still the kinetic part and poses no problem for calculation at any given instant in time⁴. The second term on the left hand side now carries an additional integral over a time interval, τ_σ .

One way of motivating the transition from forces \mathbf{F}_{ij} to the change in momentum may be to introduce the Dirac delta function to account for the infinite forces on collision,

$$\mathbf{F}_{ij} = m \Delta \mathbf{v}_{ij} \delta(t, t_{ij}),$$

where t_{ij} refers to the collision time of colloids i and j . Concentrating solely on the potential term, we find,

$$\begin{aligned} \frac{1}{\tau_\sigma} \int_{-\tau_\sigma}^0 \sum_{ij} (F_{ij})_x (r_{ij})_y &= \frac{1}{\tau_\sigma} \sum_{ij} \int_{-\tau_\sigma}^0 m (\Delta v_{ij})_x \delta(t, t_{ij}) (r_{ij})_y, \\ &= \frac{1}{\tau_\sigma} \sum_{coll}^{\tau_\sigma} m (\Delta v_{ij})_x (r_{ij})_y. \end{aligned}$$

³Compare to the definition of the local velocity in equation (4.15)

⁴Admittedly this is not quite true, as velocities in our algorithm are by and large unphysical. As it happens their average is necessarily correct, though.

To streamline the notation a bit we have contracted the integral and sum of the first line into a single sum, $\sum_{coll}^{\tau_\sigma}$, over all collisions within the time span, τ_σ . This is true, as by definition $\delta(t, t_{ij})$ is zero, whenever the pair ij does not suffer a collision. So the final expression for the stress tensor is:

$$\sigma_{xy}^{\tau_\sigma}(t) = \frac{1}{V} \left(\sum_i m (v_i(t))_x (v_i(t))_y + \frac{1}{\tau_\sigma} \sum_{coll}^{\tau_\sigma} m (\Delta v_{ij})_x (r_{ij})_y \right). \quad (4.17)$$

4.4.2 Potential forces under Brownian motion

The entire argument now hinges upon the idea that we can calculate the forces via the change in momentum. While this is — given some additional averaging — perfectly reasonable for Newtonian Dynamics, it is not clear how to justify this procedure for the case of Brownian dynamics. The problem is buried in the fact that our interpretation of the algorithm insists on displacing particles using what we termed *pseudo-velocity*. This unphysical velocity is simply used to propel the particle to the right place and does not claim to reflect the true velocity of the particles at all times.

Foss and Brady [21] suggested that the displacements due to correcting overlaps can be equated to the inter-particle forces. In our case, these are the collisions.

Figure 4.12 schematically shows the distribution of displacements of a particle facing a second particle on the right. For a free particle, the white Gaussian curve centred at the position of the colloid would describe the probability distribution. The fact that no overlap is allowed is reflected in the red section of the curve.

The area is equivalent to the region that the particle is deprived of exploring — made visible as an orange mirror image. Pondering figure 4.12, we see that the portion of displacements we are concerned with here is what is coloured in red. This is precisely the fraction of movements, having terminated where they are, due to a collision. The claim was that the dynamics is correct only when τ_B is small enough to cause, at most, one collision between Brownian events — hence, the conclusion that one (and only one) collision occurred is reasonable. From the theoretical point of view, it might appear difficult to distinguish which displacements ended at some position due to a collision, as opposed to pure Brownian motion. In other words: one can not distinguish from the final position how the particle got there, that is, whether it belongs to the red fraction or the white (and orange) section. In simulations this information is provided gratuitously.

So we must return to the collisions to calculate the force. It remains to be answered what the change in momentum is. Since we are not dealing with true velocities, the change of momentum cannot be correct either. While this is certainly true on the level of an individual particle, the hand waving claim at this point is, that on average the velocities are correct. Immutably, the ensemble average has to be fixed. And it is therefore a good

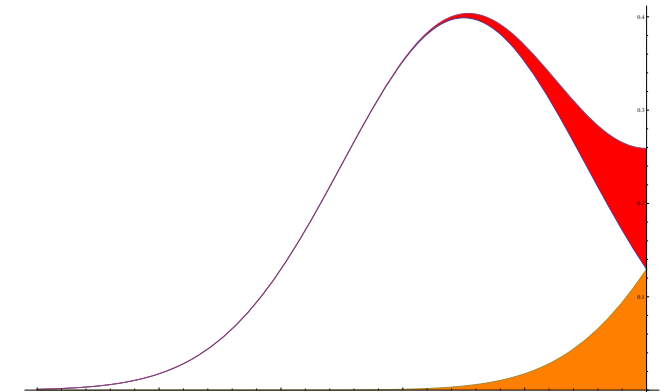


Figure 4.12. Displacement distribution on collision: In orange the forbidden tail, in red where it adds on.

guess to grant the particle a token velocity according to what the bath prescribes — and for this purpose the velocity drawn every τ_B is as good as any other.

To summarise: we will consider collisions only, as this reflects the red fraction of figure 4.12 and claim that, on average, the velocities are correct.

4.4.3 Stress-stress correlation function

Time averaged stress-stress correlation function

As pointed out in the previous section, we are dealing with a stress tensor not *at* time t , but averaged over a small period of time τ_σ up to t . In this sense, our stress tensor may be referred to more precisely as:

$$\langle \sigma_{xy}(t) \rangle_{\tau_\sigma} = \frac{1}{\tau_\sigma} \int_{-\tau_\sigma}^0 dt' \sigma(t+t') \quad (4.18)$$

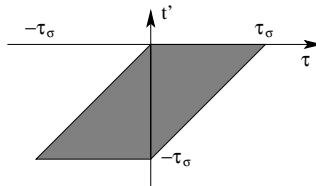
One might suspect that this has consequences for the correlation function as well. In fact our correlation function now looks like:

$$\begin{aligned} C_{\sigma\sigma}^{\tau_\sigma}(t) &= \frac{V}{k_B T} \left\langle \langle \sigma_{xy}(t) \rangle_{\tau_\sigma} \langle \sigma_{xy}(0) \rangle_{\tau_\sigma} \right\rangle, \\ &= \frac{V}{k_B T \tau_\sigma^2} \left\langle \frac{1}{\tau_\sigma} \int_{-\tau_\sigma}^0 dt' \sigma(t+t') \frac{1}{\tau_\sigma} \int_{-\tau_\sigma}^0 dt'' \sigma(t'') \right\rangle, \\ &= \frac{V}{k_B T \tau_\sigma^2} \int_{-\tau_\sigma}^0 dt' \int_{-\tau_\sigma}^0 dt'' \langle \sigma(t+t') \sigma(t'') \rangle. \end{aligned}$$

Employing time translational invariance we find,

$$\langle \sigma(t+t') \sigma(t'') \rangle = \langle \sigma(t+t'-t'') \sigma(0) \rangle$$

and introduce the variable $\tau = t' - t''$ to write,



$$\begin{aligned} C_{\sigma\sigma}^{\tau_\sigma}(t) &= \frac{V}{k_B T \tau_\sigma^2} \int_{-\tau_\sigma}^0 dt' \int_{t'}^{t'+\tau_\sigma} d\tau \langle \sigma(t+\tau) \sigma(0) \rangle \\ &= \frac{1}{\tau_\sigma^2} \int_{-\tau_\sigma}^0 dt' \int_{t'}^{t'+\tau_\sigma} d\tau C_{\sigma\sigma}(t+\tau). \end{aligned}$$

In order to progress, we need to change the order of integration.

$$\begin{aligned} C_{\sigma\sigma}^{\tau_\sigma}(t) &= \frac{1}{\tau_\sigma^2} \left(\int_{-\tau_\sigma}^0 d\tau C_{\sigma\sigma}(t+\tau) \int_{-\tau_\sigma}^{\tau} dt' + \int_0^{\tau_\sigma} d\tau C_{\sigma\sigma}(t+\tau) \int_{\tau-\tau_\sigma}^0 dt' \right) \\ &= \frac{1}{\tau_\sigma^2} \left(\int_{-\tau_\sigma}^0 d\tau C_{\sigma\sigma}(t+\tau) (\tau_\sigma + \tau) + \int_0^{\tau_\sigma} d\tau C_{\sigma\sigma}(t+\tau) (\tau_\sigma - \tau) \right) \\ &= \frac{1}{\tau_\sigma^2} \left(\int_{-\tau_\sigma}^0 d\tau C_{\sigma\sigma}(t+\tau) \tau - \int_0^{\tau_\sigma} d\tau C_{\sigma\sigma}(t+\tau) \tau + \tau_\sigma \int_{-\tau_\sigma}^{\tau_\sigma} d\tau C_{\sigma\sigma} \right) \quad (4.19) \end{aligned}$$

Unfortunately, $C_{\sigma\sigma}(t+\tau)$ is not symmetrical in τ and we have to introduce the function $C_{\sigma\sigma}(t+\tau)$ at this point.

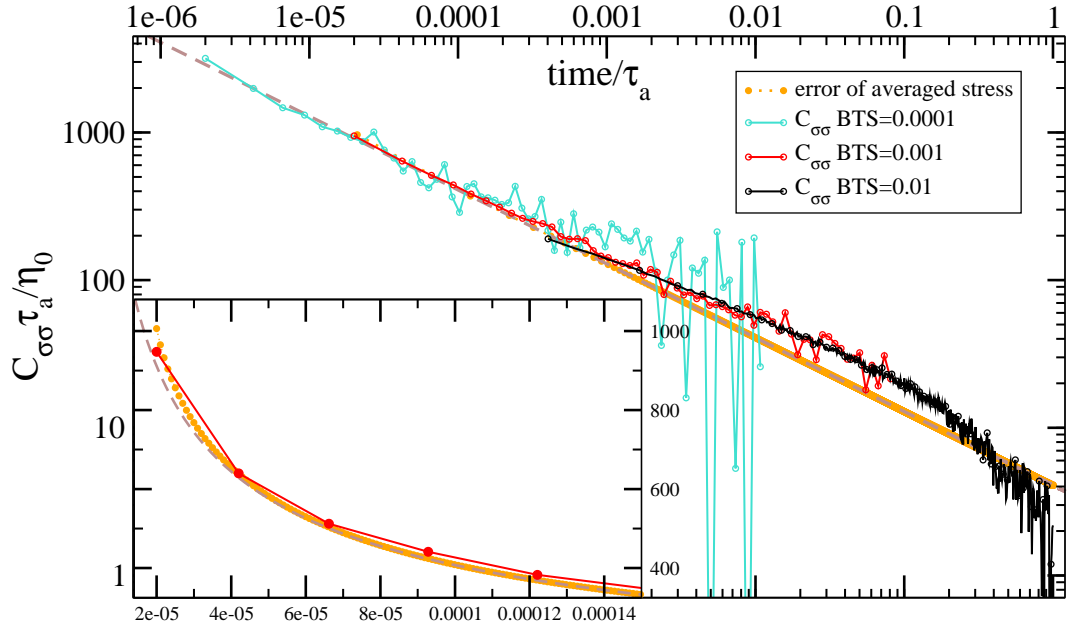


Figure 4.13. The stress-stress correlation function of a system at the freezing point: $\phi = 0.494$, $\sigma = 1$, $k_B T = 1$, $\frac{\tau_a}{\eta_0} = \frac{3}{4}\pi \approx 2.3562$. With $\tau_B = 0.01$ and $D_0 = 0.005$, we find $\tau_a = 50$ or, alternatively, with $\tau_B = 0.001$ $D_0 = 0.0005$ and $\tau_a = 500$. All this applied to equation (4.20) gives an asymptote of the form $\lim_{t \rightarrow 0} \frac{\tau_a}{\eta_0} C_{\sigma\sigma}(t) \approx 8.1484 \frac{1}{\sqrt{\tau}}$. For very small times the data agrees well with theory. Note however, that for $\tau_B = 0.01$ the limits imposed by the requirements for averaging the stress tensor do not allow us to attain to correlation times small enough to show the divergence. Only a more Brownian system displays the limiting behaviour clearly. The deviation may be explained with the process of averaging, as shown in equation (4.21), and visualised by the dotted orange line for a system with $\tau_\sigma = 0.001$.

4.4.4 The limit $t \rightarrow 0$ of $C_{\sigma\sigma}$ for Brownian dynamics

Lionberger and Russel[35] have shown that for hard spheres with Brownian motion and no hydrodynamic interactions in the limit of high frequencies, the stress-stress correlation function diverges as $\sqrt{\omega}$. Their result is,

$$\frac{\sigma^3 G'_\infty}{k_B T} = \sqrt{\frac{\sigma^2 \omega}{D_0}} \frac{24\phi^2}{5\pi} g(\sigma),$$

where the modulus $G'(t)$ corresponds exactly to $C_{\sigma\sigma}(t)$. $G'(\omega)$ is defined as

$$G(\omega) = \omega \int_0^\infty dt G(t) \sin(t\omega)$$

and has to be transformed back to a function of time. To this end it is useful to observe

$$G(\omega) = \omega \int_0^\infty dt \frac{\sin(t\omega)}{\sqrt{t}} = \sqrt{\frac{\pi}{2}} \sqrt{\omega}.$$

With this we can write down the expression for the limit $t \rightarrow 0$:

$$\lim_{t \rightarrow 0} C_{\sigma\sigma}(t) = \frac{k_B T}{\sigma^3} \sqrt{\frac{\sigma^2}{D_0}} \frac{24\phi^2}{5\pi} g(\sigma) \sqrt{\frac{2}{\pi}} \frac{1}{\sqrt{t}},$$

Written down in a dimensionless form borrowed from Nägele [37] we find,

$$\lim_{t \rightarrow 0} \frac{\tau_a}{\eta_0} C_{\sigma\sigma}(t) = \frac{18}{5} \phi^2 g(\sigma) \sqrt{\frac{2}{\pi}} \frac{1}{\sqrt{\tau}} = \alpha \frac{1}{\sqrt{\tau}}, \quad (4.20)$$

where $\tau_a \equiv \frac{\sigma^2}{4D_0}$, $\eta_0 \equiv \frac{k_B T}{3\pi D_0 \sigma}$ and $\tau \equiv t/\tau_a$. This equation describes now the diverging behaviour of the stress-stress correlation function as it approaches $t = 0$. Being an exact result, this gives an asymptote to which any simulation result should attain in the appropriate time range. The comparatively simple functional form of equation (4.20) allows us to take up equation (4.19) again. We now need to address the integrals,

$$\begin{aligned} \alpha \int_{-\tau_\sigma}^0 d\tau \frac{\tau}{\sqrt{t+\tau}} &= \frac{2\alpha}{3} \left(-2t\sqrt{t} + 2t\sqrt{t-\tau_\sigma} + \tau_\sigma\sqrt{t-\tau_\sigma} \right), \\ \alpha \int_0^{\tau_\sigma} d\tau \frac{\tau}{\sqrt{t+\tau}} &= \frac{2\alpha}{3} \left(2t\sqrt{t} - 2t\sqrt{t+\tau_\sigma} + \tau_\sigma\sqrt{t+\tau_\sigma} \right) \quad \text{and} \\ \alpha\tau_\sigma \int_{-\tau_\sigma}^{\tau_\sigma} d\tau \frac{1}{\sqrt{t+\tau}} &= \alpha\tau_\sigma \left(\sqrt{t+\tau_\sigma} - \tau_\sigma\sqrt{t-\tau_\sigma} \right). \end{aligned}$$

These can be added together according to equation (4.19) and conveniently regrouped to give:

$$\lim_{t \rightarrow 0} C_{\sigma\sigma}^{\tau_\sigma}(t) = \frac{4\alpha}{3\tau_\sigma^2} \left[-2t^{\frac{3}{2}} + (t+\tau_\sigma)^{\frac{3}{2}} + (t-\tau_\sigma)^{\frac{3}{2}} \right] \quad (4.21)$$

To show that this is indeed very close to our original function $C_{\sigma\sigma}$, we note that we are only interested in times $t > \tau_\sigma$ — as we will not be able to calculate the correlation function for times smaller than τ_σ . No harm is done when we furthermore insist that $t > 0$, as well as $\tau_\sigma > 0$. We can then rewrite $(t \pm \tau_\sigma)^{\frac{3}{2}}$ as $(1 \pm \frac{\tau_\sigma}{t})^{\frac{3}{2}} t^{\frac{3}{2}}$ and expand $\frac{\tau_\sigma}{t}$ around zero:

$$\left(1 \pm \frac{\tau_\sigma}{t}\right)^{\frac{3}{2}} t^{\frac{3}{2}} \approx \left(1 \pm \frac{3\tau_\sigma}{2t} + \frac{3\tau_\sigma^2}{8t^2} \pm \frac{\tau_\sigma^3}{16t^3} + \frac{3\tau_\sigma^4}{128t^4} \pm \mathcal{O}\left[\left(\frac{\tau_\sigma}{t}\right)^5\right]\right) t^{\frac{3}{2}}.$$

Inserting into equation (4.21) the zeroth and all odd orders are cancelled. The second order terms return exactly the function $C_{\sigma\sigma}$ and the first correction is of the order of $(\frac{\tau_\sigma}{t})^4$:

$$\lim_{t \gg \tau_\sigma} C_{\sigma\sigma}^{\tau_\sigma}(t) \approx \frac{\alpha}{\sqrt{t}} + \frac{\tau_\sigma^4}{16t^4} t^{\frac{3}{2}} + \mathcal{O}\left[\left(\frac{\tau_\sigma}{t}\right)^5 t^{\frac{3}{2}}\right] \quad (4.22)$$

We can conclude that our smudged out stress tensor does not significantly alter the value of the stress-stress correlation function, as long as we are looking at times $t \gg \tau_\sigma$. It might even be said that it explains some of the deviation from the theoretical curve (see orange curve in figure 4.13)

In Newtonian dynamics the limit of $t \rightarrow 0$ for the correlation function has different properties (see section 4.5.2), that are best demonstrated once the viscosity has been introduced in the next section.

4.5 Transport coefficients: The viscosity

Green-Kubo relations provide a means to calculate the transport coefficients, that appear in the hydrodynamic equations, from a microscopic level[7]. We exploit this relationship to calculate the viscosity of a system and show how this is implemented in our simulation by drawing analogies to the diffusion coefficient.

4.5.1 Einstein relation for correlation functions

The problem at hand is very akin to what we have inadvertently used when we extracted the diffusion coefficient from the mean squared displacement. So let us remind ourselves how we ought to think about the relation of the diffusion coefficient, mean squared displacement and the velocity-velocity autocorrelation function.

We start with the velocity-velocity autocorrelation function.

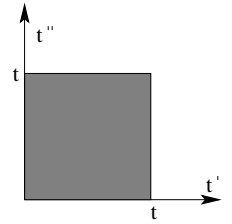
$$C_{vv} = \int_0^\infty dt \langle v(t)v(0) \rangle.$$

The key to the diffusion coefficient is nothing more than simple integration:

$$\int_0^t dt v(t) = r(t) - r(0).$$

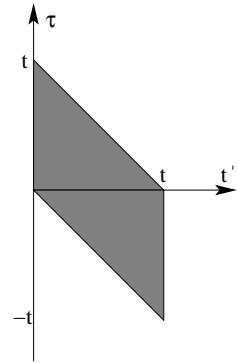
Having said that we can pursue what is a standard derivation to make the connection between the diffusion coefficient and the mean squared displacement clearer.

$$\begin{aligned} \langle (r(t) - r(0))^2 \rangle &= \int_0^t dt' \int_0^t dt'' \langle v(t')v(t'') \rangle, \\ &= \int_0^t dt' \int_0^t dt'' \langle v(t'' - t')v(0) \rangle, \quad \text{let } \tau \equiv t'' - t', \\ &= \int_0^t dt' \int_{-t'}^{t-t'} d\tau \langle v(\tau)v(0) \rangle. \end{aligned}$$



All we need to do now is change the order of integration with some care (see figures), to find,

$$\begin{aligned} &= \int_{-t}^0 d\tau \langle v(\tau)v(0) \rangle \int_\tau^t dt' + \int_0^t d\tau \langle v(\tau)v(0) \rangle \int_0^{t-\tau} dt', \\ &= \int_0^t d\tau \langle v(\tau)v(0) \rangle [t - \tau + t - \tau], \\ &= 2t \int_0^t d\tau \langle v(\tau)v(0) \rangle \left[1 - \frac{\tau}{t}\right], \end{aligned}$$



Considering the limit of $t \rightarrow \infty$, or at least $t \gg \tau$, we finally get,

$$\langle (r(t) - r(0))^2 \rangle = 2t \int_0^t d\tau \langle v(\tau)v(0) \rangle = 2tD.$$

This is known as the *Einstein relation*, connecting the mean squared displacement with the long time diffusion coefficient D .

In this frame of mind, we now tackle a very similar problem — namely the *viscosity*. Again, in the linear response regime, there exists a Green-Kubo relation for this transport coefficient.

$$\eta = \frac{V}{k_B T} \int_0^\infty dt C_{\sigma\sigma} = \frac{V}{k_B T} \int_0^\infty dt \langle \sigma_{xy}(t)\sigma_{xy}(0) \rangle.$$

As the stress tensor,

$$\sigma_{xy}^{\tau\sigma}(t) = \frac{1}{V} \left(\sum_i m (v_i(t))_x (v_i(t))_y + \frac{1}{\tau_\sigma} \sum_{\text{coll}}^{\tau_\sigma} m (\Delta v_{ij})_x (r_{ij})_y \right),$$

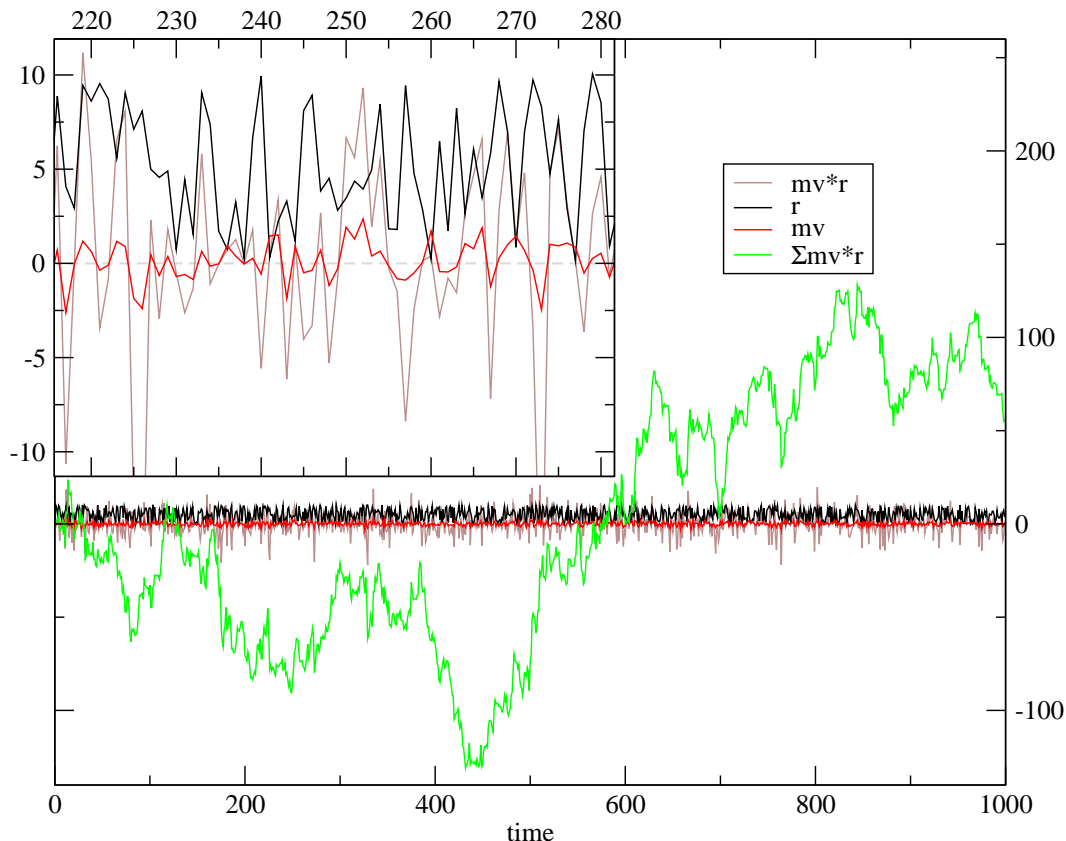


Figure 4.14. The components of $q_{xy} = \frac{1}{V} \sum_i m (v_i)_x (r_i)_y$ as a function of time. The position coordinates are shown as a black line, with their values limited by the box size. In red, the momentum is shown to vary around zero. The product of both (grey) has no choice other than to do the same and so, ultimately, does the sum — but on a longer time scale. The variance of q_{xy} is a constant unless one uses the extended coordinates.

it is easy to find a $q_{xy} = \frac{1}{V} \sum_i m (v_i)_x (r_i)_y$ such that $\dot{q} = \sigma$. That said, it would be very tempting to follow the mathematics through to arrive at some sort of *Einstein relation* of the form,

$$2t\eta = \frac{V}{k_B T} \left\langle (q_{xy}(t) - q_{xy}(0))^2 \right\rangle. \quad (4.23)$$

Computationally, this is a remarkable step as it reduces a resource consuming double sum to a single sum. Unfortunately, this route has to be abandoned due to the difficulties with the boundary conditions. It is not clear what \sum_i in this context really means, as some particles will move out of the box and particles that previously were outside the box will move into the box in any given time span. On the other hand, it is vital that the extended coordinates are used, as otherwise the quantity will be a constant (see figure 4.14).

Instead we now follow a different path suggested by Alder, Wainwright and Gass [4]. In contrast to the previous example, we resort to direct integration this time — in particular,

$$\frac{V}{k_B T} \left\langle (q_{xy}(t) - q_{xy}(0))^2 \right\rangle = \frac{V}{k_B T} \left\langle \left(\int_0^t dt' \dot{q}_{xy}(t') \right)^2 \right\rangle.$$

The point here is to integrate in a discrete — but accurate — fashion.

$$\frac{V}{k_B T} \int_0^t dt' \dot{q}_{xy}(t') = \sum_{coll} \left(m \frac{1}{V} \sum_i (v_i)_x (v_i)_y \right) \Delta t_c + \sum_{coll} (\Delta v_{ij})_x (r_{ij})_y. \quad (4.24)$$

\sum_{coll} means we sum over the collisions. The first sum being the kinetic part is, on average, zero in the off diagonal entries and will be disregarded. The second term describes the dominant part due to the velocity change whenever two particles collide.

This carries over unchanged, when Brownian motion is added, as all velocity changes due to solvent collisions do not enter this formula. Any change due to Brownian motion are therefore an effect of the alteration of the actual dynamics. A two body system may serve as a simple example to illustrate what might be expected when considering Brownian motion in the context of stresses. In Newtonian dynamics the case is clear cut: two particles collide once, or never. In contrast, the system with Brownian motion might register any number of collisions depending on the timescale of τ_B .

We refer to this technique of calculating the viscosity η as the *integral method* and introduce for convenience and ease of notation, a new function

$$\Delta A(t) = \frac{1}{3} \sum_{x < y} \int_0^t dt' \dot{\sigma}_{xy}(t').$$

We can therefore sum up the integral method in the following equation:

$$\eta = \frac{V}{k_B T} \int_0^\infty dt C_{\sigma\sigma}(t) = \frac{V}{2k_B T} \lim_{t \rightarrow \infty} \frac{1}{t} \langle \Delta A(t)^2 \rangle. \quad (4.25)$$

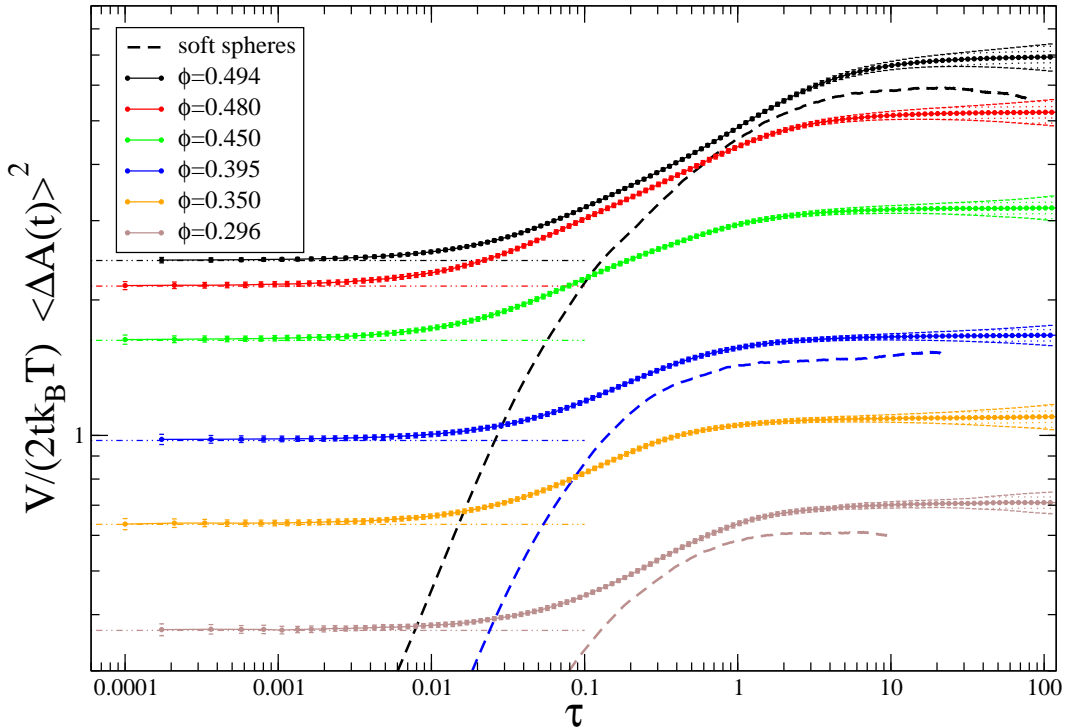


Figure 4.15. The integral method is capable of probing the limit $t \rightarrow 0$ of $C_{\sigma\sigma}$ and makes the delta contribution at the origin, η_δ , visible. The theoretical values of η_δ are given for all densities as dashed-dotted lines in respective colours, the thick dashed lines being results from simulations with soft spheres. Error bars indicate standard deviation on averaging up to 400 sets.

4.5.2 The limit $t \rightarrow 0$ of $C_{\sigma\sigma}$ for Newtonian dynamics

We can now come back to the short time limit of the stress-stress correlation function in the case of Newtonian dynamics. It has been shown [16] that the stress correlation function of hard spheres has two contributions: a δ -function with weight η_δ at the origin and a well behaved bounded curve for the remaining region. We sample the latter part only. However, when it comes to evaluating the viscosity by integrating the entire correlation function, this contribution gives rise to an extra term:

$$\eta = \frac{V}{k_B T} \int_0^\infty dt C_{\sigma\sigma}(t) = \eta_\delta + \frac{V}{k_B T} \int_\delta^\infty dt C_{\sigma\sigma}(t), \quad (4.26)$$

The contribution has been determined theoretically [16] and is given by the expression

$$\eta_\delta = \eta_0 \frac{192}{25\pi} \left(\frac{P\pi}{6k_B T} - \phi \right), \quad (4.27)$$

where P is the pressure and η_0 is the viscosity from kinetic theory, $\eta_0 = \frac{5}{16\sigma^2} \left(\sqrt{\frac{mk_B T}{\pi}} \right)$.

Despite the fact that we can not hope to evaluate the correlation function $C_{\sigma\sigma}$ in the limit of $t \rightarrow 0$, the integral method of determining the viscosity is able to probe η_δ accurately. This is illustrated in figure 4.15, where $\langle \Delta A(t)^2 \rangle$ is shown to converge to a finite value for hard disks — in stark contrast to the behaviour of soft spheres decaying to zero (dashed lines).

Similar to the diffusion coefficient, the viscosity can be calculated via a Green-Kubo relation with the stress correlation function, or by the long-time limit of the integrated stress:

$$\eta = \frac{\beta}{V} \int_0^\infty dt C_{\sigma\sigma}(t) = \frac{V}{2k_B T} \lim_{t \rightarrow \infty} \frac{1}{t} \langle \Delta A(t)^2 \rangle, \quad (4.28)$$

where $\Delta A(t) = \int_0^t \sum_{\alpha < \beta} \sigma^{\alpha\beta}(t') dt'$, with the brackets indicate averaging over time origin for this integral, and V is the volume of the system. In HS, the δ -function in $C_{\sigma\sigma}(t)$ mentioned above gives a contribution to the correlation function of the integrated stress at $t = 0$, equal to η_δ with [8]:

$$\eta_\delta = \eta_0 \frac{192}{25\pi} \left(\frac{P\pi}{6k_B T} - \phi \right), \quad (4.29)$$

where P is the pressure and η_0 is the viscosity from kinetic theory $\eta_0 = \frac{5}{16\sigma^2} \left(\sqrt{\frac{mk_B T}{\pi}} \right)$. Numerically, the integration of the correlation function is noisier and, therefore, the viscosity is usually calculated using the integral of the stress tensor (second equality in equation (4.28)). These different approaches are summarised in Fig. 4.16 where 10 000 independent calculations of $\frac{V}{2tk_B T} \Delta A(t)^2$ have been performed and averaged to obtain the black curve. Note the finite short time limit for HS, which agrees with the theoretical value $2\eta_\delta$ — this is in stark contrast to the decay to zero for SS. A range of viscosities, corresponding to the long time plateaus in Fig. 4.15, were presented in Fig. 3.10 for hard and soft spheres with microscopic ND as a function of $\Gamma/\Gamma_{\text{freezing}}$.

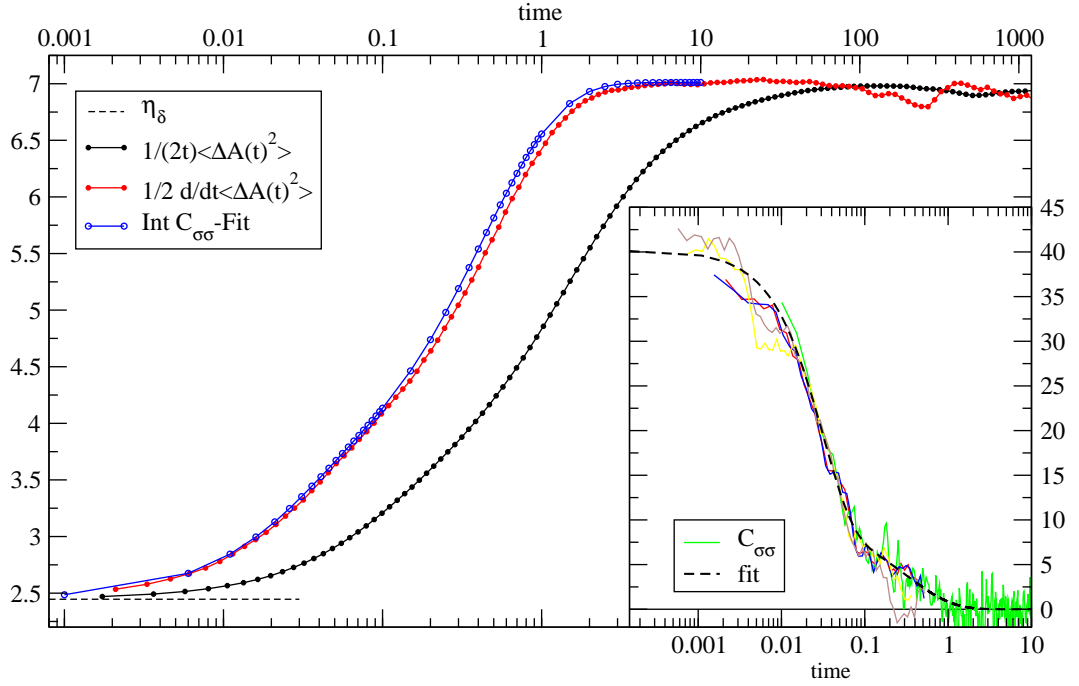


Figure 4.16. Comparing the viscosity integral for a Newtonian system at packing fraction $\phi = 0.494$. The inset shows the stress-stress correlation function that is being approximated (dashed black) for the analytic evaluation of the integral (blue). The comparison with the appropriate derivative of $\langle \Delta A(t)^2 \rangle$ (red) shows good agreement. Applying the integral method demonstrates the convergence of the value of the viscosity for large times (black).

Double-checking the viscosity

Given that we have the correlation function $C_{\sigma\sigma}$ itself, it is tempting to compare a direct integration to the computational method described in equation (4.24). Together with equation 4.25, we find the following identity:

$$\begin{aligned}
 \frac{V}{2k_B T} \frac{d}{dt} \langle \Delta A(t)^2 \rangle &= \frac{V}{2k_B T} \left\langle \frac{d}{dt} \left(\int_0^t dt' \dot{\varrho}_{xy}(t') \right)^2 \right\rangle, \\
 &= \frac{V}{2k_B T} \left\langle \frac{d}{dt} (\varrho_{xy}(t) - \varrho_{xy}(0))^2 \right\rangle, \\
 &= \frac{V}{2k_B T} \langle 2(\varrho_{xy}(t) - \varrho_{xy}(0)) \dot{\varrho}_{xy}(t) \rangle, \\
 &= \frac{V}{k_B T} \langle (\varrho_{xy}(t) - \varrho_{xy}(0)) \sigma_{xy}(t) \rangle, \\
 &= \frac{V}{k_B T} \left\langle \int_0^t dt' \sigma_{xy}(t') \sigma_{xy}(t) \right\rangle, \\
 &= \frac{V}{k_B T} \int_0^t dt' \langle \sigma_{xy}(t') \sigma_{xy}(t) \rangle, \\
 &= \frac{V}{k_B T} \int_0^t dt' C_{\sigma\sigma}(t' - t).
 \end{aligned}$$

In order to evaluate the integral, $\int_0^\infty dt' C_{\sigma\sigma}(t')$, we have fitted an analytic function to the simulation results, as shown in the insets of figures 4.16 and 4.17. For Newtonian dynamics

the function can be fitted using a combination of two stretched exponentials, expressly:

$$C_{\sigma\sigma}(t) \approx \eta_\delta + 10.25 e^{-2.5 x^{0.8}} + 30 e^{-65 x^{1.2}}.$$

For Brownian dynamics, we used our knowledge of the functional form in the limit $t \rightarrow 0$ and two more partial fits (see inset in figure 4.17) to evaluate the integral.

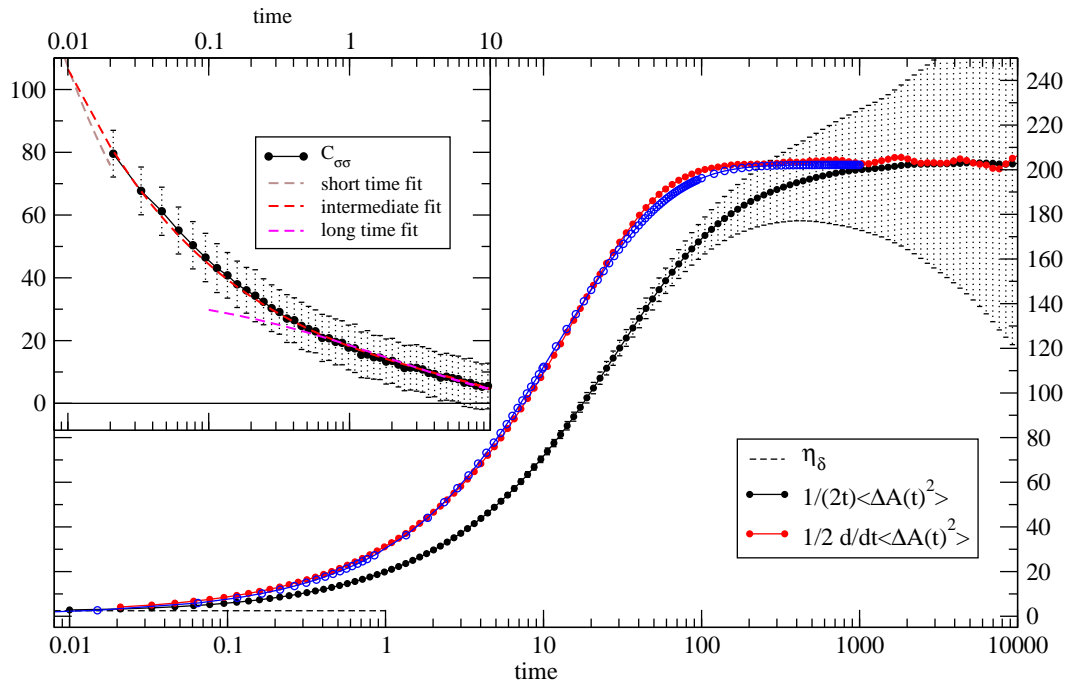


Figure 4.17. Brownian dynamics yields a much higher viscosity and shows also the Newtonian η_δ for times shorter than τ_B . In the inset the various curves that have been used for different sections of correlation function are shown (dashed lines). The integrals show equally good agreement as in the case of Newtonian dynamics (see figure 4.16).

5

Dense colloidal systems under shear

5.1 Shear in the Langevin equation

We would like to implement the simplest shear flow imaginable — with a linear velocity profile. This corresponds to the behaviour of a solvent between two flat plates of which one is moving at some constant (not too high) speed. After a certain period of time one would expect to gain a steady state resembling what is illustrated in figure 5.1, as linear velocity profile. The resulting solvent velocity \mathbf{v}_s can be expressed as

$$\mathbf{v}_\gamma(\mathbf{r}) = \mathbf{\Gamma} \cdot \mathbf{r} = \dot{\gamma} \begin{pmatrix} 0 & 0 & 1 \\ 0 & 0 & 0 \\ 0 & 0 & 0 \end{pmatrix} \cdot \mathbf{r} = \dot{\gamma} z \mathbf{x}, \quad (5.1)$$

which introduces the shear rate, $\dot{\gamma}$, and defines the gradient direction as being along the z-axis and the shear-direction along the x-axis with unit vector $\hat{\mathbf{x}}$.

Returning to the Langevin equation (2.2), there is some need to refine the interpretation of the terms. It is in fact the velocity in the expression $m\zeta\mathbf{v}$ one should take issue with. Clearly the systematic pelting of the colloid by the solvent particles has a different quality now that the solvent has a velocity of its own. It follows that the term as it stands is now a mixture of friction and driving from the flow. The pure friction as we know it should be given by the velocity relative to the solvent flow: $m\zeta(\mathbf{v} - \mathbf{v}_\gamma)$.

Furthermore, the random force, \mathbf{f}_s , is not necessarily isotropic anymore so that for the time being the autocorrelation, $\langle \mathbf{f}_s(t) \mathbf{f}_s(0) \rangle$, may only be written down in the generic form as given in equation (2.3), with the added complication that now the matrix \mathbf{H} may not be a diagonal. This is a severe restriction as we need to specify the autocorrelation in order to find the probability distribution function.

We express the Langevin equation in terms of the relative velocities $\mathbf{v}' = \mathbf{v} - \mathbf{v}_\gamma$ [15] and find,

$$\dot{\mathbf{v}}' = -(\zeta \mathbf{I} + \mathbf{\Gamma}) \cdot \mathbf{v}' + \frac{1}{m} \mathbf{f}_s. \quad (5.2)$$

This can be integrated again as was done in section 2.0.1 to get an equation for the velocities,

$$\mathbf{v}'(t) = e^{-(\zeta \mathbf{I} + \mathbf{\Gamma})t} \cdot \mathbf{v}'_0 + \frac{1}{m} \int_0^t dt' e^{-(\zeta \mathbf{I} + \mathbf{\Gamma})(t-t')} \cdot \mathbf{f}_s(t'). \quad (5.3)$$

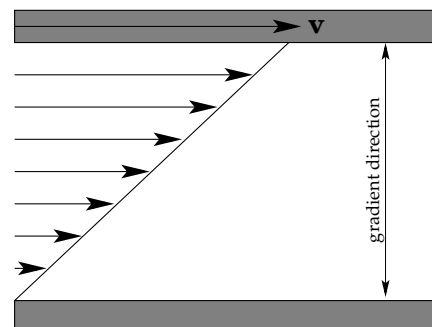


Figure 5.1. Simple shear with linear velocity profile. Top plate moves.

As in the equilibrium case, one is led to postulate for the relative coordinates that the second moment, $\mathbf{v}'(t)$, should obey the equipartition theorem — at least for the steady state. This entails calculating the second moment of the velocities:

$$\begin{aligned} \lim_{t \rightarrow \infty} \langle \mathbf{v}'(t) \mathbf{v}'(t) \rangle &= \mathbf{I} k_B T / m. \\ &= \frac{1}{2m^2 \zeta} \left(\mathbf{H} - \frac{1}{2\zeta} (\mathbf{H} \cdot \mathbf{\Gamma}^T + \mathbf{\Gamma} \cdot \mathbf{H}) + \frac{1}{2\zeta^2} (\mathbf{\Gamma} \cdot \mathbf{H} \cdot \mathbf{\Gamma}^T) \right) \end{aligned}$$

Still, the above result is not yet of much practical value. Some additional observations are needed to progress: \mathbf{H} should be symmetric and, given the simplicity of $\mathbf{\Gamma}$ as written out in equation (5.1), we see that $\mathbf{\Gamma} \cdot \mathbf{\Gamma} \cdot \mathbf{\Gamma}^T = 0$, as well as $\mathbf{\Gamma} \cdot \mathbf{\Gamma}^T \cdot \mathbf{\Gamma}^T = 0$. Considering the simplest possible symmetric solution of the form,

$$\mathbf{H} = \alpha_0 \mathbf{I} + \alpha_2 (\mathbf{\Gamma} + \mathbf{\Gamma}^T),$$

both coefficients can be identified as $\alpha_0 = 2k_B T m \zeta$ and $\alpha_2 = mk_B T$.

As before we are interested in the Langevin equation of the displacements in the overdamped limit. This is equivalent to *relaxing* the momentum in equation (5.2), which then reads

$$\begin{aligned} 0 &= -(\zeta \mathbf{I} + \mathbf{\Gamma}) \cdot \mathbf{v}' + \frac{1}{m} \mathbf{f}_s, \\ \mathbf{v}' &= (\zeta \mathbf{I} + \mathbf{\Gamma})^{-1} \cdot \frac{1}{m} \mathbf{f}_s. \end{aligned}$$

In cases of a $\dot{\gamma} \ll \zeta$, we can further simplify this equation to,

$$\mathbf{v}' = \frac{1}{m\zeta} \mathbf{f}_s,$$

which can be solved to find the equation of the relative displacement:

$$\mathbf{r}'(t) = r_0 + \frac{1}{m\zeta} \int_0^t dt' \mathbf{f}_s(t'). \quad (5.4)$$

With this we have all of the ingredients necessary for applying Chandrasekhar's theorem to find the appropriate probability distribution,

$$P(\mathbf{r}', t | \mathbf{r}'(0), t = 0) = \frac{1}{(4\pi D_0 t)^{\frac{3}{2}}} \exp \left[-\frac{|\mathbf{r}' - \mathbf{r}'(0)|^2}{4D_0 t} \right]. \quad (5.5)$$

which is identical to equation (2.10) of the unsheared case, except for the fact that we are here dealing with the relative displacement \mathbf{r}' . This means that in this approximation \mathbf{r}' is isotropic, while the absolute displacement of the particle is distorted solely by an extra shear term. This can be incorporated easily, given one is prepared to accept the discretisation error on the level of the Brownian timescale, τ_B :

$$\mathbf{r}(\tau_B) = \mathbf{r}'_0 + \tau_B (\mathbf{V}_s + \dot{\gamma} z \mathbf{x}). \quad (5.6)$$

A more careful analysis [15, 32] unearths a non-diagonal matrix in the probability distribution function which leads to some weak correlation of the shear and gradient directions of the order of $\mathcal{O}(\dot{\gamma} \tau_B)$. So far, we can not point to any physical situation where this might have a noticeable effect. For this reason, and the fact that it requires some computational effort, all shear has been implemented using the simple equation (5.6). The detail that complicates matters is the fact that the conventional periodic boundary conditions cease to be valid.

5.2 Computational implications

Despite the fact that the equation of motion (5.6) has only suffered a minor change and is easy to implement, shear requires an entirely independent set of programs. The inconvenience of the periodic boundary conditions not working under shear is the root cause of a substantial number of the changes in the very simulation code, as well as all changes necessary in most of the programs mining the data.

5.2.1 Lees-Edwards boundary conditions

The idea of periodic images has proven to be very useful and all we need do here is to motivate a method of preserving this concept, facing broken symmetry due to shear.

We consider a particle (red) and its image (green) in the neighbouring box in the gradient direction as shown in figure 5.2. After one time step the original particle would leave the box due to the displacements indicated by arrows in gradient and shear directions. As a consequence of shear, both particles have a different velocity with respect to our simulation box as indicated by the different lengths of the displacement in shear direction. With ordinary periodic boundary conditions we know where to place the original (light red) particle when it leaves the box. However, this does not correspond to the position of its image (light green) as it finds its way into the box from above. Clearly the physically correct picture is the latter. The question is then: how to achieve this without needing to keep track of the different velocities and positions of all the images?

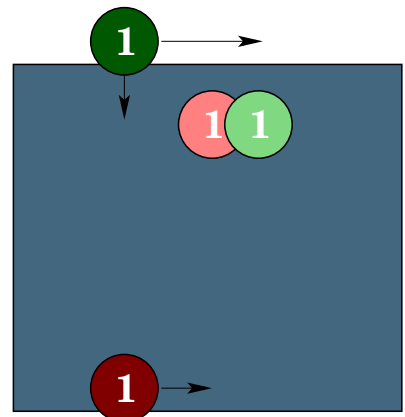


Figure 5.2. *Two choices when reinserting a particle?*

The underlying problem is that shear destroys the translational symmetry of the periodic boundary condition and, as a result, the particle positions in any one of the conventional images differ due to the varying shear rate. This can be resolved by co-moving as an observer with the average shear rate of any one of the image boxes. Seen from this perspective, all boxes revert to being simple images of the original in the rest frame. This procedure is illustrated in figure 5.3, where in the rightmost column we see how the part of the displacement due to the shear flow is attached to the image box as a whole (green arrows) in such a manner that the images boxes themselves are identical. This trick constitutes the key ingredient of the Lees-Edwards boundary conditions.

On the nitty gritty level of computing this means that the rules for reinserting a particle when it crosses the box boundaries are more complicated. In fact, we need to keep track of a new time variable, t_{PBC} , that tells us when the image boxes were last aligned as if ordinary periodic boundary conditions (PBC) applied. If we assume now that a particle will leave the box in gradient direction (that is z) with the next Brownian time step, the rules for the displacements are:

On the nitty gritty level of computing this means that the rules for reinserting a particle when it crosses the box boundaries are more complicated. In fact, we need to keep track of a new time variable, t_{PBC} , that tells us when the image boxes were last aligned as if ordinary periodic boundary conditions (PBC) applied. If we assume now that a particle will leave the box in gradient direction (that is z) with the next Brownian time step, the rules for the displacements are:

$$\begin{aligned}\Delta z &= z_0 + v_z \tau_B \pm L. \\ \Delta x &= x_0 + v_x \tau_B \pm v_\gamma t_{PBC}.\end{aligned}\tag{5.7}$$

The expression, $\pm v_\gamma t_{PBC}$, takes care of the shift of the neighbouring box from which the

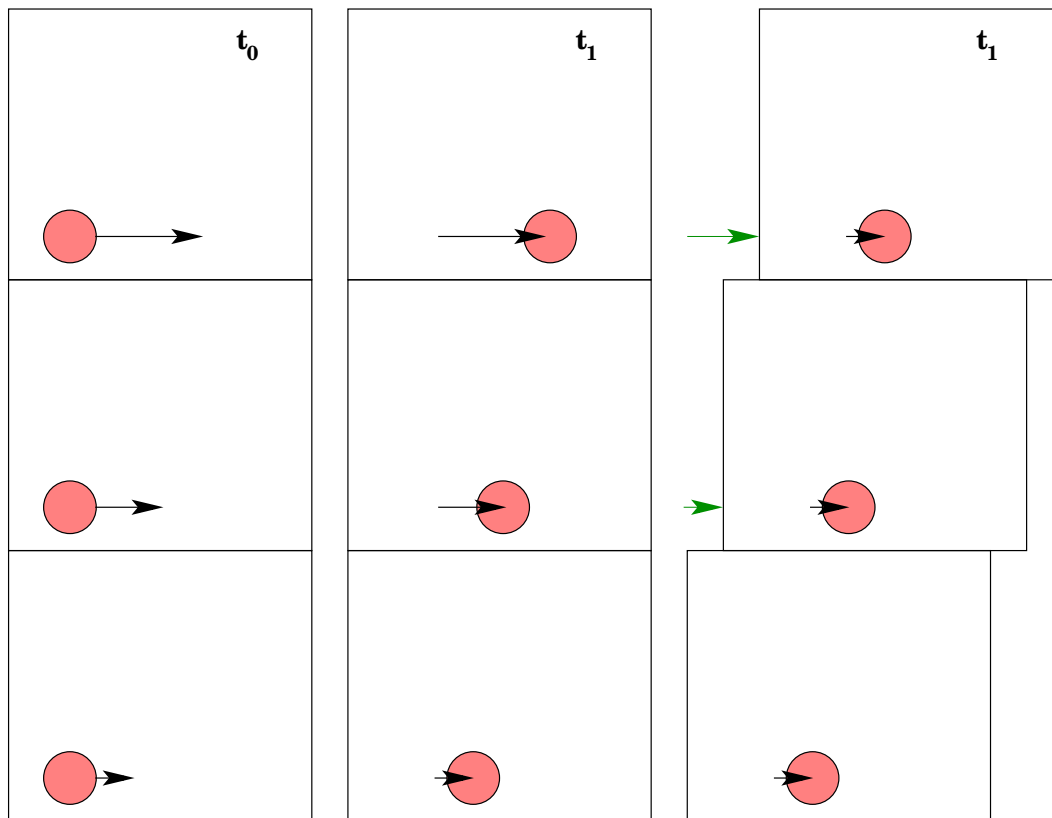


Figure 5.3. Shear breaks the translational symmetry of the periodic boundary condition. After one time step t_1 the positions of one and the same particle differs depending on which image box is considered. Shown are in the middle column three neighbouring images of the simulation box in gradient direction at time t_1 . The solution to saving the periodic images is indicated in the right column: Lees-Edwards or sliding brick boundary conditions.

appropriate image particle would have moved into the original box. As it were, $\pm v_\gamma t_{PBC}$ is precisely the displacement depicted with green arrows in figure 5.3.

Except for triggering this peculiar shift in x-direction, the boundary conditions for the z-coordinate are equivalent to the simple periodic boundary conditions. Any boundary crossings in one of the remaining two directions do not feature any eccentricities and are handled equivalently to standard periodic boundary conditions.

5.2.2 From snapshots to the real world

Particularly when calculating the mean squared displacement (MSD), the following problem arises: how does one find the position of a particle had it not been subjected to the boundary conditions. One might suspect that more information than just the two snapshots, as presented in figure 5.4, is needed. Indeed, we need additional information about the number of times a particle has moved outside the box. This is traditionally achieved with snapshots that are sufficiently close in time in order to betray jumps — due to the application of the boundary conditions — which are large compared to the possible displacements.

Let us assume the following two dimensional scenario. We have two snapshots at some

points in times, t_0 and t_f , and know that the particle in question has moved out of the box in the gradient direction. There are exactly N Brownian time steps (τ_B) between t_0 and t_f and, for the sake of argument, the time when the particle leaves the box, t_c , also coincides with one Brownian time step, that is: $t_c = c\tau_B$, with c as a positive integer.

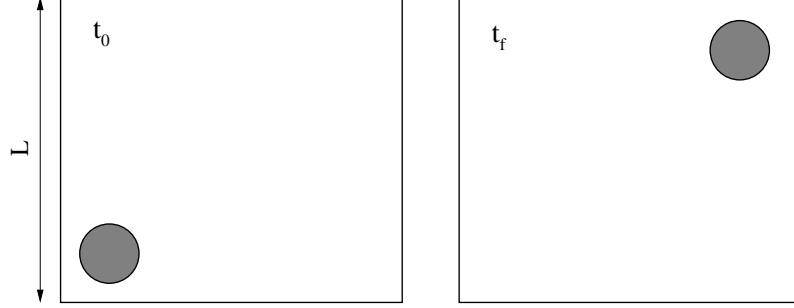


Figure 5.4. Positions of one and the same particle at two distinct times. Snapshots and the information on periodic boundary crossings are needed to reconstruct the extended (real) position of the particle unambiguously.

We can immediately write down the real displacement along the shear direction. This is taking into account one single boundary crossing in gradient direction only:

$$x_f = x_0 + \sum_{i=1}^c \tau_B \dot{x}_i + \sum_{i=c+1}^N \tau_B (\dot{x}_i - \dot{\gamma}L),$$

where the second sum describes the displacement after the particle has entered the *sliding brick* below. As a result, we subtract $\dot{\gamma}L$ from the velocity.

$$\begin{aligned} x_f - x_0 &= \sum_{i=1}^c \tau_B \dot{x}_i + \sum_{i=c+1}^N \tau_B \dot{x}_i - \sum_{i=c+1}^N \tau_B \dot{\gamma}L, \\ \Delta x &= \sum_{i=1}^N \tau_B \dot{x}_i - \sum_{i=c+1}^N \tau_B \dot{\gamma}L, \\ \Delta x &= \sum_{i=1}^N \tau_B \dot{x}_i - (N - c)\tau_B \dot{\gamma}L, \\ \Delta x &= \sum_{i=1}^N \tau_B \dot{x}_i - N\tau_B \dot{\gamma}L + c\tau_B \dot{\gamma}L, \\ \Delta x &= \Delta x_v - \Delta x_s + t_c \dot{x}_s. \end{aligned} \tag{5.8}$$

We have summarised the total random displacement under the label $\Delta x_v \equiv \sum_{i=1}^N \tau_B \dot{x}_i$, as well as the total shear displacement of the neighbouring box as $\Delta x_s \equiv N\tau_B \dot{\gamma}L$.

With Lees Edwards boundary conditions the particle will be reinserted into the box as soon as it strays beyond the boundary. While the gradient coordinate follows simple

periodic boundary conditions, the displacement in shear direction follows from:

$$\begin{aligned}
 x'_f &= x_0 + \sum_{i=1}^c \tau_B \dot{x}_i + t_c \dot{\gamma} L + \sum_{i=c+1}^N \tau_B \dot{x}_i, \\
 \Delta x' &= \sum_{i=1}^N \tau_B \dot{x}_i + t_c \dot{\gamma} L, \\
 \Delta x' &= \Delta x_v + t_c \dot{x}_s.
 \end{aligned} \tag{5.9}$$

Comparing the expressions in equations 5.8 and 5.9, we see that the only difference is the total shear displacement Δx_s . This does not depend on the time at which the particle crossed the box boundary and is easily calculated from the data available. From this short analysis, it becomes apparent that the one-to-one correspondence between the particle position (or one of its images for that matter) inside the box and the *true* position outside remains intact as long as one is able to keep track of how often the particle has taken advantage of the periodic boundary conditions.

This is precisely the crux of the matter. There certainly exist ambiguous situations when one is unable to decide whether a particle has actually moved across half the box or instead tunnelled through the boundary conditions. So from snapshots alone it is impossible to keep track of the boundary crossings, particularly when the time that has elapsed between recorded particle positions becomes large¹. For a truly Gaussian distribution of displacements, this will be ambiguous on any timescale. The situation is further aggravated by the introduction of shear and Lees-Edwards boundary conditions.

As a result, we save two sets of coordinates. One we have become accustomed to call the *extended* set, which depicts the positions as if no boundary conditions had existed and the original set that always *folds* the positions back into the simulations box. Strictly speaking, the latter set is not needed. However, it is convenient as most calculations are done on this set.

5.2.3 Structure factor under Lees-Edwards boundary conditions

We have pointed out in section 4.1.2 how a massive simplification in terms of computing can be achieved by observing that $\langle \rho(\mathbf{q}) \rho(-\mathbf{q}) \rangle = \langle |\rho(\mathbf{q})|^2 \rangle$. Despite the fact that this is generally wrong for a simulation box, the method was salvaged by the fact that the periodic boundary conditions conspired with the periodicity of the Fourier transform rendering any box-sized numerical error void.

This is unfortunately not the case for the Lees-Edwards boundary conditions. As the minimum image occasionally demands use of the coordinates of a particle in a neighbouring box (cf figure 5.5(b)), we can see from equation (5.7), that this position in shear direction now contains a shear term $\pm v \dot{\gamma} t_{PBC}$. This term that corresponds to the last term in equation (5.7) depends on t_{PBC} — a parameter keeping track of the time since the sheared boxes were aligned last.

It is precisely this time dependent term that spells trouble: now that the shear coordinate does not correspond to the position in the original box with an additional term of the size

¹As is the case towards the end of a logarithmic time scale

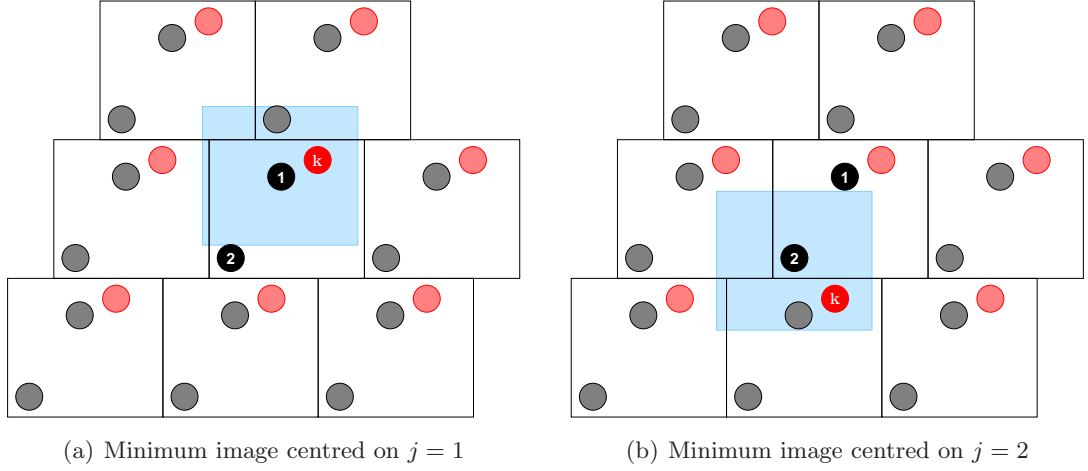


Figure 5.5. *The minimum image in a system with Lees-Edwards boundary conditions. The absolute coordinates of particle k depend on the position of particle j and the shear offset as a function of time.*

of an integer number of box length nL . And with this observation, it becomes clear that

$$\langle \rho(\mathbf{q})\rho(-\mathbf{q}) \rangle \neq \langle |\rho(\mathbf{q})|^2 \rangle.$$

The consequence is that we now have to go back to the definition of the structure factor (5.2.3) and evaluate the exponential, keeping in mind that $\mathbf{r}_k(\mathbf{r}_j, t_{PBC})$ is a function of \mathbf{r}_j and t_{PBC} , resulting in

$$S(\mathbf{q}) = \left\langle \sum_{j < k} \exp [i\mathbf{q} \cdot \{\mathbf{r}_j - \mathbf{r}_k(\mathbf{r}_j, t_{PBC})\}] \right\rangle.$$

This is sketched in figure 5.5, where we used the same configuration as in figure 4.3, however, applying Lees-Edwards boundary conditions. It can be seen in figure 5.5(b), that the horizontal position of the appropriate image of the particle k does in fact propagate through the minimum image as a function of time, while the *sliding brick* moves past the original box.

5.2.4 Density-density correlation function under shear

In a system under shear the density-density correlation function, as given in equation 5.10, requires some amendments if we want to preserve the interpretation of this quantity — specifically the idea that two particles at rest should not decorrelate. Under shear this can only mean that two particles that swim as it were with the flow should not by virtue of the shear decorrelate. As a consequence, the shear needs to be subtracted. One way of achieving this goal is to employ the idea of the advected wavevector [23], introducing a time dependence to the wave vector, $\mathbf{q}(t) = \mathbf{q} - \mathbf{q} \cdot \mathbf{\Gamma}t$, with the shear rate tensor $\mathbf{\Gamma}$, as defined in equation 5.1.

Here we only quote the result as used to calculate the correlation function, $C_{\rho\rho}(\mathbf{q}, t)$. The theory follows from an extension of the definition of the static structure factor, as given in equation (4.5): We introduce the additional dimension of time.

$$C_{\rho\rho}(\mathbf{q}, t, \dot{\gamma}) = \frac{1}{N} \langle \rho_{-\mathbf{q}(0)}(0) \rho_{\mathbf{q}(t)}(t) \rangle. \quad (5.10)$$

Written out explicitly, this turns into

$$C_{\rho\rho}(\mathbf{q}, t, \dot{\gamma}) = \frac{1}{N} \left\langle \sum_j \exp[i\mathbf{q} \cdot \mathbf{r}_j(0)] \sum_k \exp[-i\mathbf{q} \cdot \{\mathbf{r}_k(t) - \dot{\gamma} z_k(t) \hat{\mathbf{x}}t\}] \right\rangle, \quad (5.11)$$

and can again be split into a incoherent (self) and a coherent (distinct) part to give:

$$C_{\rho\rho}(\mathbf{q}, t, \dot{\gamma}) = \frac{1}{N} \left\langle \sum_j \exp[-i\mathbf{q} \cdot \{\mathbf{r}_j(t) - \dot{\gamma} z_j(t) \hat{\mathbf{x}}t - \mathbf{r}_j(0)\}] + \sum_{j \neq k} \exp[-i\mathbf{q} \cdot \{\mathbf{r}_k(t) - \dot{\gamma} z_k(t) \hat{\mathbf{x}}t - \mathbf{r}_j(0)\}] \right\rangle.$$

5.3 Steady state

A sheared system is constantly subjected to external forces by the moving plates. As a result, the sample in the simulation box is not only out of equilibrium but energy is constantly pumped into it and we need some mechanism to take the excess energy out of the system. This is done almost unnoticed by dissipation through the bath which never heats up. It is precisely this helpful arrangement that fuels the hope for some type of equilibrium within the realm of non equilibrium: the *steady state*.

As the name suggests, we would be looking for a state that displays stability with respect to certain quantities despite the constant flux of energy. This is best observed by documenting the transient states during the onset of shear. These will point the way towards a steady state — if existent.

5.3.1 Switch on and waiting time

To illustrate this idea, we want to observe how the mean squared displacement changes, when out of equilibrium the sample is subjected to shear. The beginning of shear at t_0 is marked as *switch on*. We also introduce for this purpose the parameter of the *waiting time* t_w , that denotes how long the system has been under shear since the switch on (figure 5.6).

For the mean squared displacement this means we no longer average over different starting points, but keep them separate and label them, according to the time the first snapshot was taken, with different t_w . This set up is sensitive enough to pick up the transient effect shear has on the suspension, as can be seen in figure 5.7. The differences are most notable in the area where the short time diffusion gives way to the long time diffusion. This time scale — and increased contact with its neighbours — already points towards an effect connected with the structure.



Figure 5.6. t_w defines the time since shearing began.

The message to take away would be: there exists a time scale beyond which the mean squared displacement has reached a steady state.

This is true for $\dot{\gamma}t_w > 1$ (compare grey and brown), but also for the long time diffusion itself: No matter what t_w was if we look at the long time diffusion at any time $\dot{\gamma}(t - t_w) > 1$,

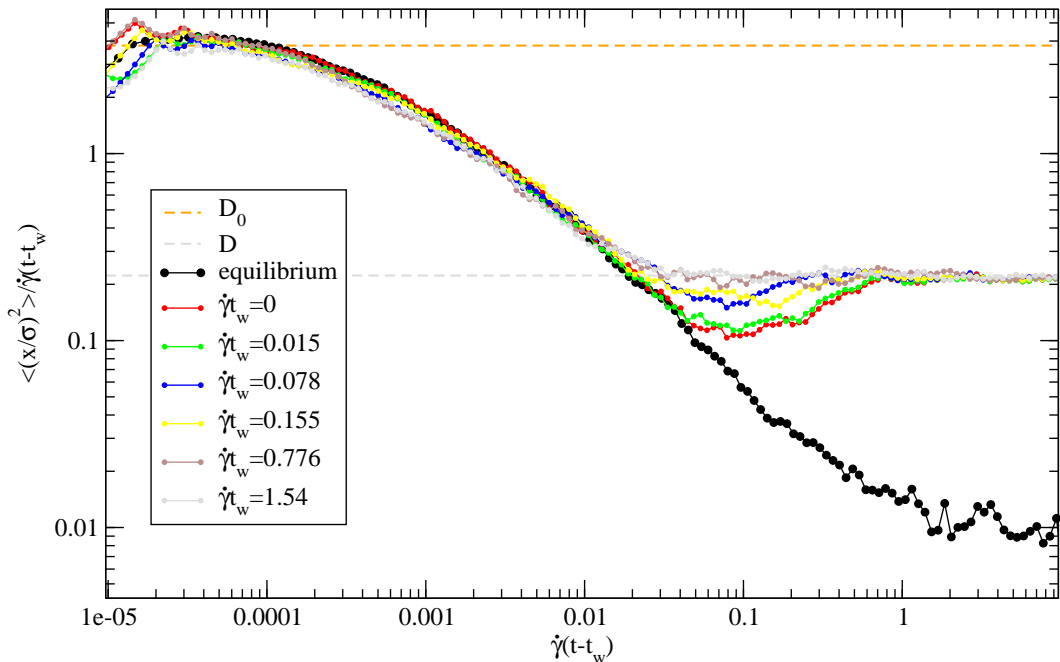


Figure 5.7. The mean squared displacement divided by time according to the different waiting times. Shown is the displacement in neutral direction only of a binary suspension under shear ($\dot{\gamma} = 0.0015$) at high density ($\phi = 0.60$). Large differences are visible at the boundary between short and long time diffusion. Time is given in units of the shear rate such that the value 1 on the time axis denotes precisely the amount of time necessary for neighbouring boxes (in gradient direction) to have drifted one entire box length apart.

we find the same curve. The upshot of this is that we take any system to be in steady state once an amount of time equivalent to the inverse shear rate, $\frac{1}{\dot{\gamma}}$, has elapsed.

This also means that any system under shear, that we want to be in steady state, will have at least run one period of $\frac{1}{\dot{\gamma}}$ before we take data.

5.4 Anisotropy of the radial distribution function

With shear, the symmetry of a fluid is broken and we can not assume isotropy anymore. This fact leaves its fingerprints, for example, in the local structure and can be made visible by examining the pair distribution function $g(\mathbf{r})$. Consequently, we now want a pair distribution function that is sensitive to directions — put in another way: $g(\mathbf{r})$ now depends not only on a scalar but a vector \mathbf{r} .

5.4.1 Projection onto spherical harmonics

The viscosity of a fluid suspension under shear has been described [52] using,

$$\eta = \eta_0 + \frac{5}{2}\phi\eta_0 - \frac{18k_B T \phi^2}{\pi^2 \sigma^6 \dot{\gamma}} \int \frac{xz}{r} \delta(r, \sigma) g(\mathbf{r}) dV. \quad (5.12)$$

This statement collects two contributions to the viscosity of a suspension. On the one hand, there is the hydrodynamic contribution in $\eta_0 + \frac{5}{2}\phi\eta_0$, as calculated by Einstein

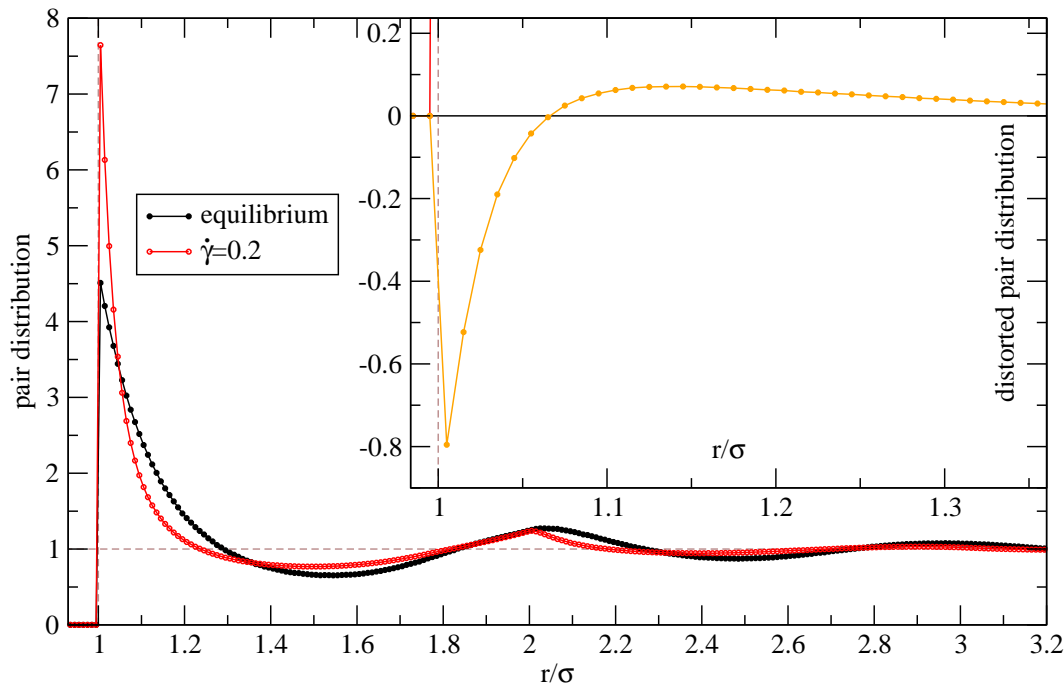


Figure 5.8. The radial distribution function for a mildly dense system at $\phi = 0.45$ in and out of equilibrium. The shear rate is quite high with $Pe = 10$ to illustrate the point that the structure does change considerably. This deviation can be capitalised to determine the viscosity.

[18, 19]. Given the fact that we have decided against hydrodynamic interactions, this low density expansion should end after the first term that describes the viscosity of a single particle in the solvent. In line with alternative formulations [49], our equation for the viscosity then reads,

$$\eta = \eta_0 - \frac{18k_B T \phi^2}{\pi^2 \sigma^6 \dot{\gamma}} \int \frac{xz}{r} \delta(r, \sigma) g(\mathbf{r}) dV. \quad (5.13)$$

We have included equation (5.12) to be able to compare with simulation results from Stratting.

On the other, we need to describe the effect of the interactions. These are captured in the last term on the right hand side, which is in essence the stress tensor component, σ_{xz} , divided by the shear rate, $\dot{\gamma}$. The $\delta(r, \sigma)$ reflects the singular forces in our hard sphere suspension.

The key observation is now that the product of shear direction, x , together with the gradient direction, z , can be rewritten profitably as,

$$\frac{xz}{r^2} = \sin(\theta) \cos(\varphi) \cos(\theta) = \sqrt{\frac{2\pi}{15}} (Y_{2,-1} - Y_{2,1}),$$

where $Y_{l,m}$ are the spherical harmonics. In our case,

$$Y_{2,\pm 1} = \mp \frac{1}{2} e^{\pm i\varphi} \sqrt{\frac{15}{2\pi}} \cos(\theta) \sin(\theta).$$

Profitably, in the sense that the spherical harmonics are an orthonormal set of functions and that is, in itself, very suggestive for the interpretation of the integral in equation (5.13)

as a projection onto $(Y_{2,-1} - Y_{2,1})$. This becomes clear when we write,

$$g(\mathbf{r}) = \sum_l \sum_{m=-l}^l G_{l,m}(r) Y_{l,m}(\theta, \varphi) = \sum_{l,m} G_{l,m}(r) Y_{l,m}.$$

Here $G_{l,m}$ is the amplitude function of some spherical harmonic, $Y_{l,m}$. It is noteworthy that $G_{l,m}$ depends on r only — all angular dependence resides in the spherical harmonics. Furthermore it is useful to remember that,

$$\int d\Omega Y_{l,m}(\theta, \varphi) Y_{p,q}(\theta, \varphi) = \delta(l,p)\delta(m,q)$$

With this arsenal we can tackle the integral in equation (5.13):

$$\begin{aligned} \int \frac{xz}{r} \delta(r, \sigma) g(\mathbf{r}) dV &= \int_0^\pi \sin(\theta) d\theta \int_0^{2\pi} d\varphi \int_0^R r^3 dr \delta(r, \sigma) \frac{xz}{r^2} g(r, \theta, \varphi), \\ &= \iint d\Omega \int_0^R r^3 dr \delta(r, \sigma) \sqrt{\frac{2\pi}{15}} (Y_{2,-1} - Y_{2,1}) \sum_{l,m} G_{l,m}(r) Y_{l,m}, \\ &= \sigma^3 \iint d\Omega \sqrt{\frac{2\pi}{15}} (Y_{2,-1} - Y_{2,1}) \sum_{l,m} G_{l,m}(\sigma) Y_{l,m}, \\ &= \sigma^3 \sqrt{\frac{2\pi}{15}} (G_{2,-1} - G_{2,1}). \end{aligned}$$

In order to keep the notation dimensionally consistent, we normalise this integral with a yet to be defined² volume, V_σ , and introduce a dimensionless *distorted pair distribution function*:

$$\begin{aligned} g_\gamma(\sigma) &= \frac{1}{V_\sigma} \int \frac{xz}{r} \delta(r, \sigma) g(\mathbf{r}) dV, \\ &= \frac{\sigma^3}{V_\sigma} \iint d\Omega \sin(\theta) \cos(\varphi) \cos(\theta) g(\sigma, \theta, \varphi), \end{aligned} \quad (5.14)$$

$$\begin{aligned} &= \frac{\sigma^3}{V_\sigma} \sqrt{\frac{2\pi}{15}} \iint d\Omega (Y_{2,-1} - Y_{2,1}) \sum_{l,m} G_{l,m}(\sigma) Y_{l,m}, \\ &= \frac{\sigma^3}{V_\sigma} \sqrt{\frac{2\pi}{15}} (G_{2,-1} - G_{2,1}), \end{aligned} \quad (5.15)$$

which yields with prefactors:

$$\frac{18k_B T \phi^2}{\pi^2 \sigma^6 \dot{\gamma}} \int \frac{xz}{r} \delta(r, \sigma) g(\mathbf{r}) dV = \frac{18k_B T \phi^2}{\pi^2 \sigma^6 \dot{\gamma}} V_\sigma g_\gamma(\sigma) = \frac{54\phi^2 \eta_0}{P_e} g_\gamma(\sigma).$$

For the viscosity this means that,

$$\eta = \eta_0 \left(1 - \frac{54\phi^2}{P_e} g_\gamma(\sigma) \right). \quad (5.16)$$

²It will take the next section to motivate the ingredients of this volume.

Implementing the projection

While equation (5.15) is a neat result that elucidates how to interpret $g_{\dot{\gamma}}$, it is hardly palatable as a recipe for mining data from a computer simulation for the obvious reason that we need to find $(G_{2,-1} - G_{2,1})$ in any case — and that is nothing other than evaluating equation (5.14). A second point we need to address is how to get to the limit of $g_{\dot{\gamma}}(\sigma)$. In the course of this exploration we will motivate the choice of prefactor in equation (5.15).

The bad news is: there is no way around calculating the integral.

$$\sqrt{\frac{2\pi}{15}} (G_{2,-1} - G_{2,1}) = \iint d\Omega \sin(\theta) \cos(\varphi) \cos(\theta) g(\sigma, \theta, \varphi).$$

Inspecting this equation with an eye for computational needs, the fact that this is a dimensionless integral across a surface begs some attention. From the outset it is clear that $g(\sigma, \theta, \varphi)$ is unattainable and we would like to motivate the typical escape route into some volume in the form of a spherical shell of finite width. So the first problem that presents itself can be rephrased from equation (5.14) as the quest for a function $g_{\dot{\gamma}}(r, \theta, \varphi)$, such that

$$\lim_{r \rightarrow \sigma} g_{\dot{\gamma}}(r, \theta, \varphi) = \frac{\sigma^3}{V_{\sigma}} \iint d\Omega \sin(\theta) \cos(\varphi) \cos(\theta) g(\sigma, \theta, \varphi). \quad (5.17)$$

Given the integral in equation (5.13), containing a $\delta(r, \sigma)$ motivated by the hard sphere interaction, it is not obvious what this integral might mean at some value σ other than the contact value.

On the other hand it is clear that, from a computational point of view, there is no way to evaluate anything like $g(\sigma, \theta, \varphi)$ on a surface with technically no volume. So we must try to unravel this problem, as it were, back to front — that is, we begin with what we can actually calculate in the spirit of section 4.1.1 and that is:

$$g_{\dot{\gamma}}(r, \theta, \varphi) = \frac{1}{V_s} \int_{r-\Delta r}^{r+\Delta r} r'^2 dr' \iint d\Omega \sin(\theta) \cos(\varphi) \cos(\theta) g(r', \theta, \varphi). \quad (5.18)$$

The volume in question here is a spherical shell V_s , defined as the difference of the volumes of two spheres $V_s = \frac{4}{3}\pi((r + \Delta r)^3 - (r - \Delta r)^3)$. If we now take the limit of $r \rightarrow \sigma$ we find that we need to do two things at once. Firstly, we need $\Delta r \rightarrow 0$ and, secondly, we want $r' = \sigma$. The latter can be achieved with a delta function. Meanwhile, we need to pay attention to the normalising volume, V_s , which turns plainly into the surface area A_s .

$$\begin{aligned} g_{\dot{\gamma}}(\sigma, \theta, \varphi) &= \lim_{\Delta r \rightarrow 0} \frac{1}{V_s} \int_{r-\Delta r}^{r+\Delta r} r'^2 dr' \iint d\Omega \sin(\theta) \cos(\varphi) \cos(\theta) g(r', \theta, \varphi), \\ &= \lim_{\Delta r \rightarrow 0} \frac{1}{V_s} \int_{r-\Delta r}^{r+\Delta r} r'^2 dr' \iint d\Omega \sin(\theta) \cos(\varphi) \cos(\theta) g(r', \theta, \varphi) \delta(r', \sigma), \\ &= \frac{\sigma^2}{A_s} \iint d\Omega \sin(\theta) \cos(\varphi) \cos(\theta) g(\sigma, \theta, \varphi). \end{aligned} \quad (5.19)$$

This last line looks very much like what we were aiming for in equation (5.17). What remains to be done is some adjustment of the normalising volumes and surfaces, respectively. By definition $A_s = 4\pi\sigma^2$ and that means that we can make equations (5.17) and (5.19) consistent by demanding $V_{\sigma} = 4\pi\sigma^3$. At the same stroke this explains the prefactors³ to $g_{\dot{\gamma}}$ in equation (5.16).

³Note how this differs from [52], where we find $\frac{18\phi^2\eta_0}{5P_c}$ as a prefactor to g_1 , hence $g_1 = 15g_{\dot{\gamma}}$.

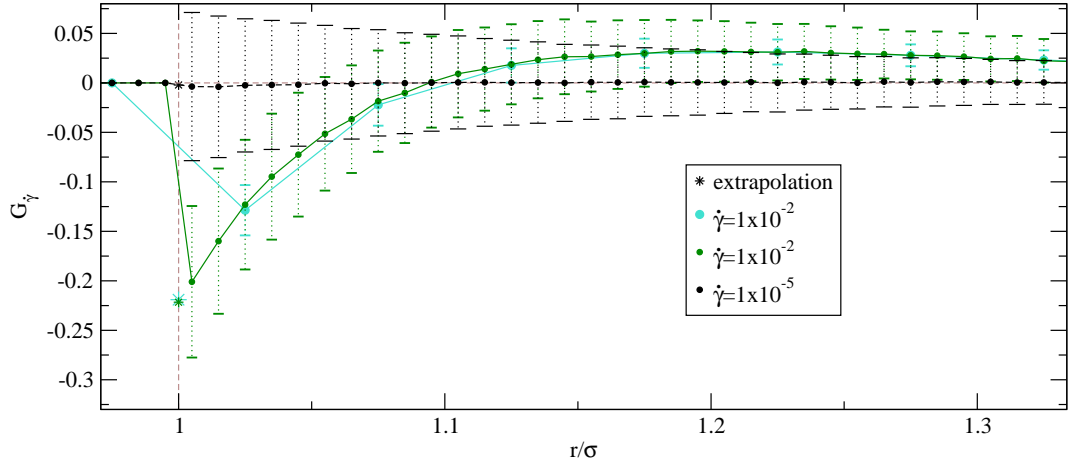


Figure 5.9. *The distorted part of the radial distribution function can be used to calculate the stresses in the fluid. At low shear rates and low densities the distortion is less pronounced and the numerical accuracy reaches its limits. Shown is a system at intermediate density ($\phi = 0.494$) with shear rates $\dot{\gamma} = 0.0001$ and $\dot{\gamma} = 0.01$, respectively. It is obvious that the extrapolation is difficult in both cases.*

Taking advantage of definition (4.3) and returning to equation (5.18) as a starting point — that is: returning to a proper shell volume, V_s — we can find an expression amenable to computer algorithms:

$$\begin{aligned}
 g_{\dot{\gamma}}(r, \theta, \varphi) &= \frac{1}{V_s} \int_{r-\Delta r}^{r+\Delta r} r'^2 dr' \iint d\Omega \sin(\theta) \cos(\varphi) \cos(\theta) g(r', \theta, \varphi), \\
 &= \frac{1}{V_s N \rho} \sum_{ij} \int_{r-\Delta r}^{r+\Delta r} r'^2 dr' \iint d\Omega \sin(\theta) \cos(\varphi) \cos(\theta) \delta(\mathbf{r}_{ij}, \mathbf{r}), \\
 &= \frac{1}{V_s N \rho} \sum_{ij} \int_{r-\Delta r}^{r+\Delta r} dr' \int_0^\pi d\theta \int_0^{2\pi} d\varphi \sin(\theta) \cos(\varphi) \cos(\theta) \delta(r_{ij}, r) \delta(\theta_{ij}, \theta) \delta(\varphi_{ij}, \varphi), \\
 &= \frac{1}{V_s N \rho} \sum_{ij}^{\epsilon V_s} \sin(\theta_{ij}) \cos(\varphi_{ij}) \cos(\theta_{ij}).
 \end{aligned}$$

Caveat: the absence of r in the last line does not mean that the r -dependence has disappeared completely from $g_{\dot{\gamma}}(r, \theta, \varphi)$ — much rather, one should be aware that, through the integration, the sum is now modified to include only pairs within the indicated volume V_s .

Inspecting a double sum over $\sin(\theta_{ij}) \cos(\varphi_{ij}) \cos(\theta_{ij})$, it might be noted that for computational convenience this can be re-expressed in Cartesian coordinates, giving the final formulation for the distorted pair distribution function:

$$g_{\dot{\gamma}}(r, \theta, \varphi) = \frac{1}{V_s N \rho} \sum_{ij}^{\epsilon V_s} \frac{x_{ij} z_{ij}}{r_{ij}^2}. \quad (5.20)$$

The limit $r \rightarrow \sigma$ in practice

We have seen that we need the distorted distribution function in the limit of the contact value — which inevitably involves some extrapolation of the function we described in equation (5.20). Figure 5.9 illustrates the problem for the case of very low as well as moderate shear rates.

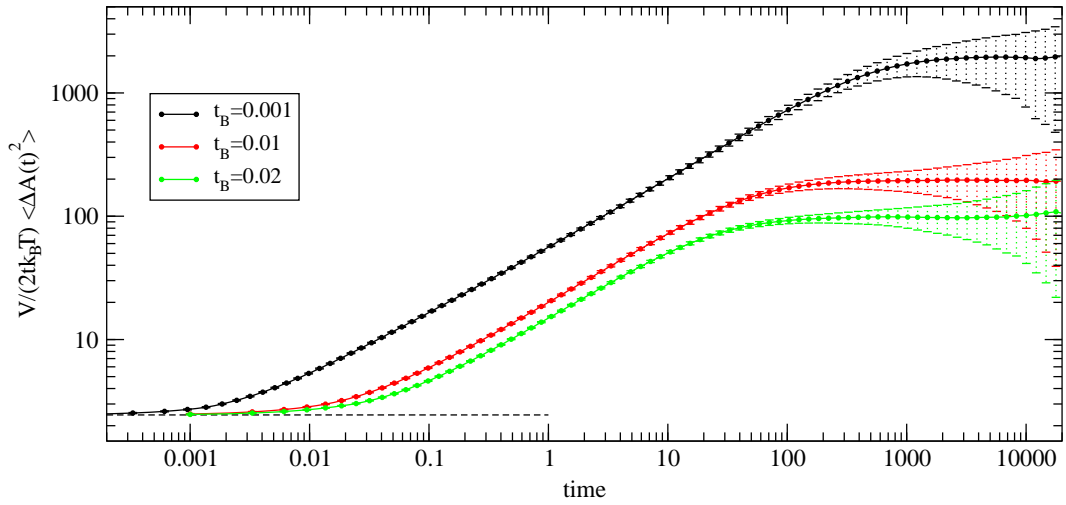


Figure 5.11. The integral method to calculate the viscosity for a monodisperse system at freezing ($\phi = 0.494$). Shown are different levels of τ_B and its effect on the viscosity. A shorter Brownian time scale results in proportionally higher solvent viscosity. Also clearly visible is the return to the Newtonian regime on time scales shorter than τ_B with a constant (dashed line) as short time limit determined by equation (4.29).

suggests an endemic cause, such as the extrapolation method or possibly the equation (5.13) connecting η to a microscopic picture.

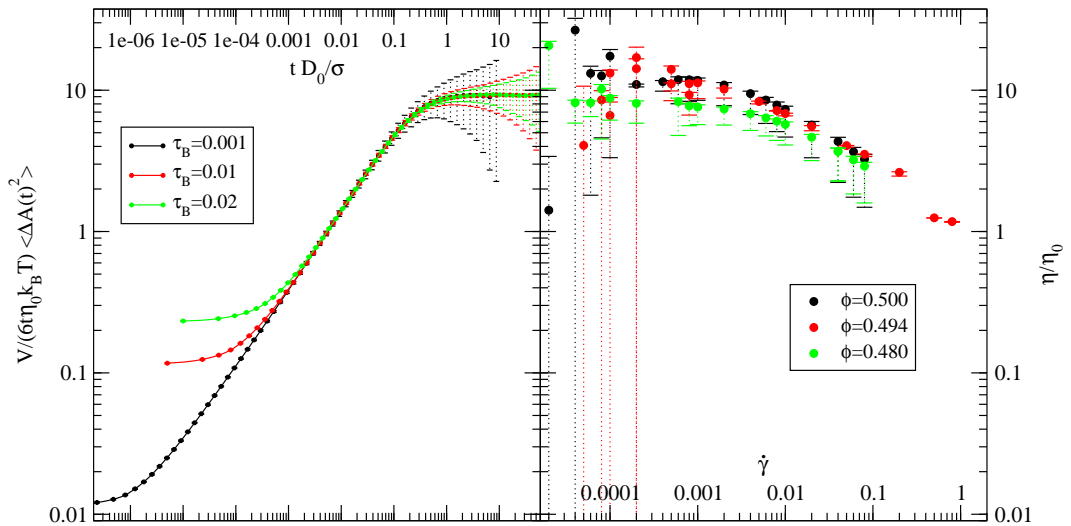


Figure 5.12. The integral method for the viscosity is shown in the left panel for a monodisperse system at freezing ($\phi = 0.494$), in terms of dimensionless quantities redressing the dependency in τ_B in the time axis, as well as the viscosity. This result can now be compared to the method of the distorted distribution function shown in the right panel. The value of the viscosity is read off where both panels meet — corresponding to either the long time limit of the integral method, or the limit of low shear rates in the method using the distorted distribution function. The right panel shows results for three densities.

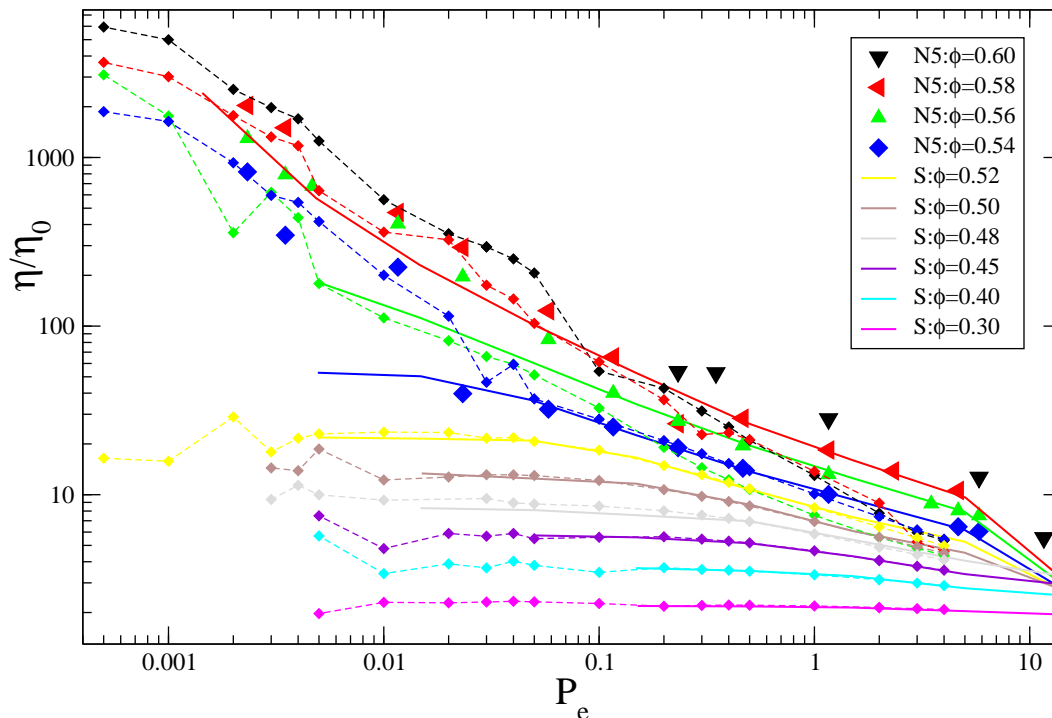


Figure 5.13. *Reproducing Strating’s [52] results (continuous lines): In the regime of high densities, the propensity of monodisperse systems to crystallise makes itself felt. Large symbols represent the results of simulations with $N = 4913$ particles; small symbols (dashed lines) show results for $N = 1000$ particles.*

5.5 Viscosity versus Peclet number

We are now in the position to use the distorted pair distribution function to show the dependence of the viscosity on the shear rate. For this purpose, we will introduce the dimensionless Peclet number $P_e = \frac{\dot{\gamma}\sigma^2}{4D_0}$, relating shear rate and diffusion. Roughly speaking, it indicates which of the two effects is dominant: large P_e means shear dominates, low P_e sees diffusion as the driving effect. For the purposes of our investigation, the short time diffusion D_0 is constant and P_e is essentially a dimensionless measure of the shear rate.

We can now check the results for the monodisperse system at different densities that Strating [52] has presented. We are undoubtedly able to reproduce this curve (including the debated hydrodynamic term) for low densities (see figure 5.13). Difficulties arise at higher densities. This is not entirely unexpected: as high densities in equilibrium inevitably crystallise, it is not unreasonable to expect a similar tendency towards some structural arrangement under shear. It has been known for quite some time that shear might even induce certain ordering phenomena [1] of which the most obvious would be layering.

We can make this point clearer by looking at the local structure by means of the radial distribution function. As an illustrative example we pick out two neighbouring data points in figure 5.13 that display a large difference in viscosity. Such an example can be found in the system at packing fraction $\phi = 0.54$ along the blue curve. In particular the two viscosities for $P_e = 0.023$ (corresponding to $\dot{\gamma} = 0.0004$) and $P_e = 0.011$ (corresponding to $\dot{\gamma} = 0.0002$) seem to be at the crossing point of crystallisation. This frontier is made visible in figure 5.14, where we can see the local structure a short time after the swelling. For both

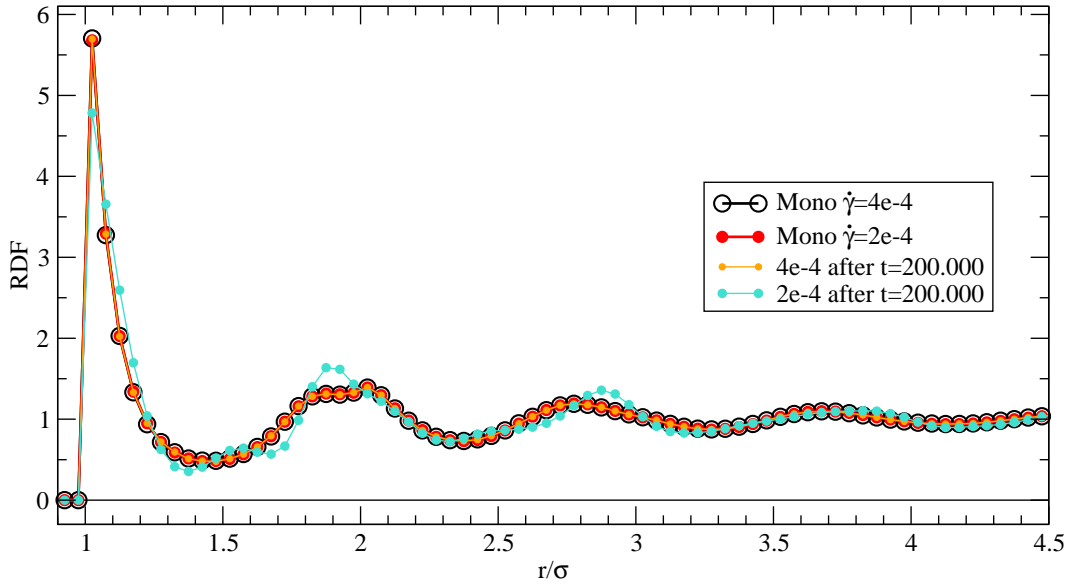


Figure 5.14. The monodisperse pair distribution function at packing fraction, $\phi = 0.54$, shows changes in the structure as a function of time. This shift in structure entails a different viscosity, which makes itself plain in in figure 5.13.

shear rates the structure is identical to the naked eye. When the same sample is inspected at the end of the simulation run (after $t = 200\,000$), we find a different picture. Now the higher shear rate, $\dot{\gamma} = 0.0004$, has managed to maintain the fluid character of the system, while the lesser shear rate $\dot{\gamma} = 0.0002$ did not have the power to fend off the structural rearrangement.

On closer inspection of the data points belonging to $\phi = 0.58$ (red), an even more complex

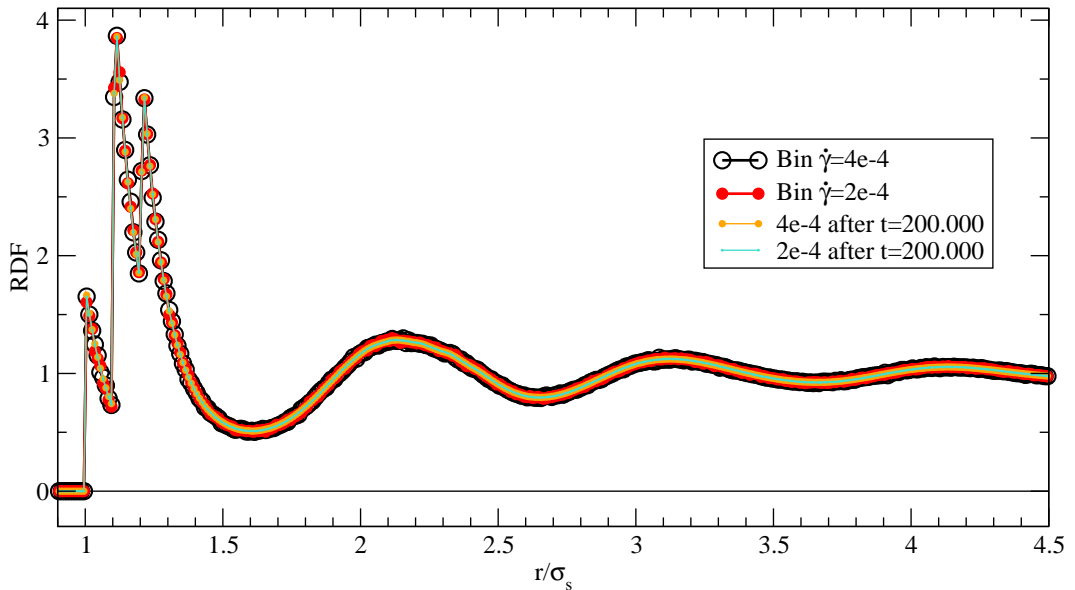


Figure 5.15. The binary system has a more complicated structure at contact due to different combinations of sphere sizes (three first peaks), but has the advantage of displaying no signs of crystallisation for the entire time accessible to our simulations. The length scale has here been scaled to the diameter of the small particles σ_s .

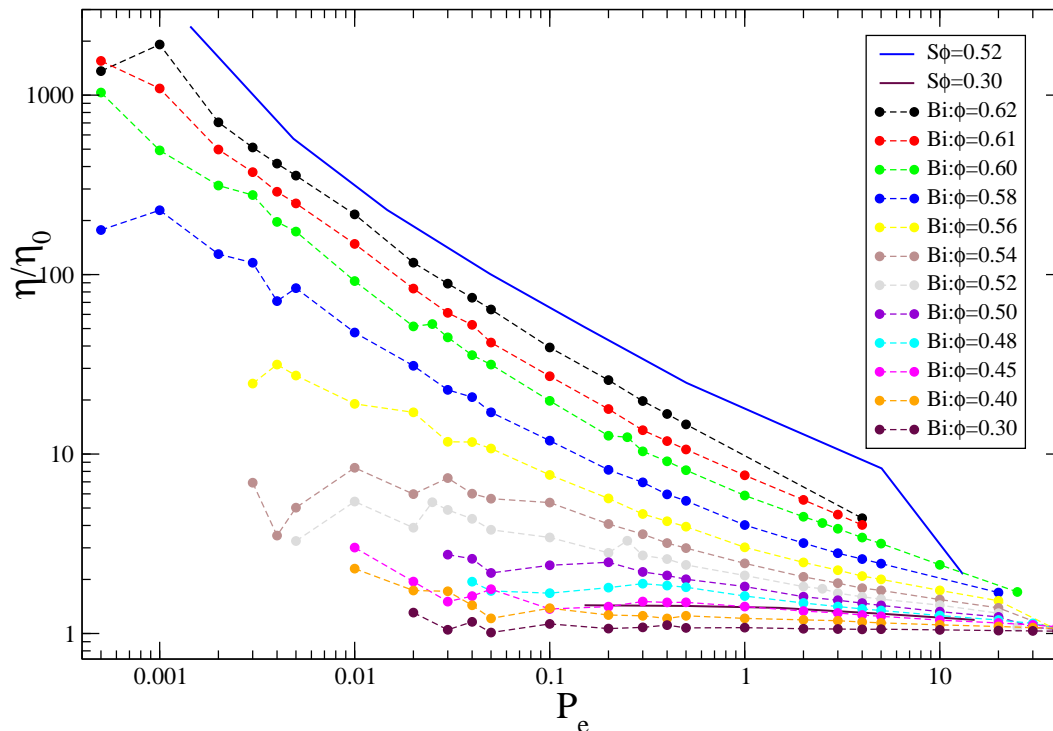


Figure 5.16. A binary system is kept from crystallisation by geometric frustration and the fluid phase is preserved in the steady state. In this system, the flow curves show a qualitatively similar behaviour. Overall, the viscosity is lower. For the sake of comparison, two results (without the hydrodynamic term) from figure 5.13 are indicated with continuous lines.

situation presents itself. At fairly high shear rates ($P_e = 0.2$), there is a marked dip in the viscosity, followed on the way to lower shear rates by a recovery of Strating’s viscosity, only to deviate towards a higher viscosity in continuation towards the low $\dot{\gamma}$ -limit. Although entirely speculative, this may be associated with two distinct phenomena: at high shear rates lane formation might ease the viscous drag, while at the extreme of low P_e we find crystallisation increasing the viscosity — opposite effects due to different ordering processes.

It is also conspicuous that the entire crop of smaller systems with only 1000 particles seem to be affected by larger shear rates more drastically — this again might be interpreted as pointing towards shear induced ordering that might impose itself more readily on a smaller system.

The picture that emerges from these considerations is then the following: It is possible to exploit the time span that it takes for the crystals to form and grow to noticeable sizes to obtain results that appear like results from a fluid system. On the other hand it is certainly debatable whether this really constitutes a fluid system. The fact is that the results obtained in such a manner are not compatible with a system that has reached its steady state under shear, as presented in figure 5.13.

One way to avoid this ambiguity is to use a polydisperse system that successfully frustrates crystallisation. We have chosen the binary system described in section 2.2.1. The radial distribution function shows no sign of structural rearrangements during the course of the simulation — as presented in figure 5.15, the pair distribution does not change appreciably.

The outcome is qualitatively very similar to those employing a monodisperse system

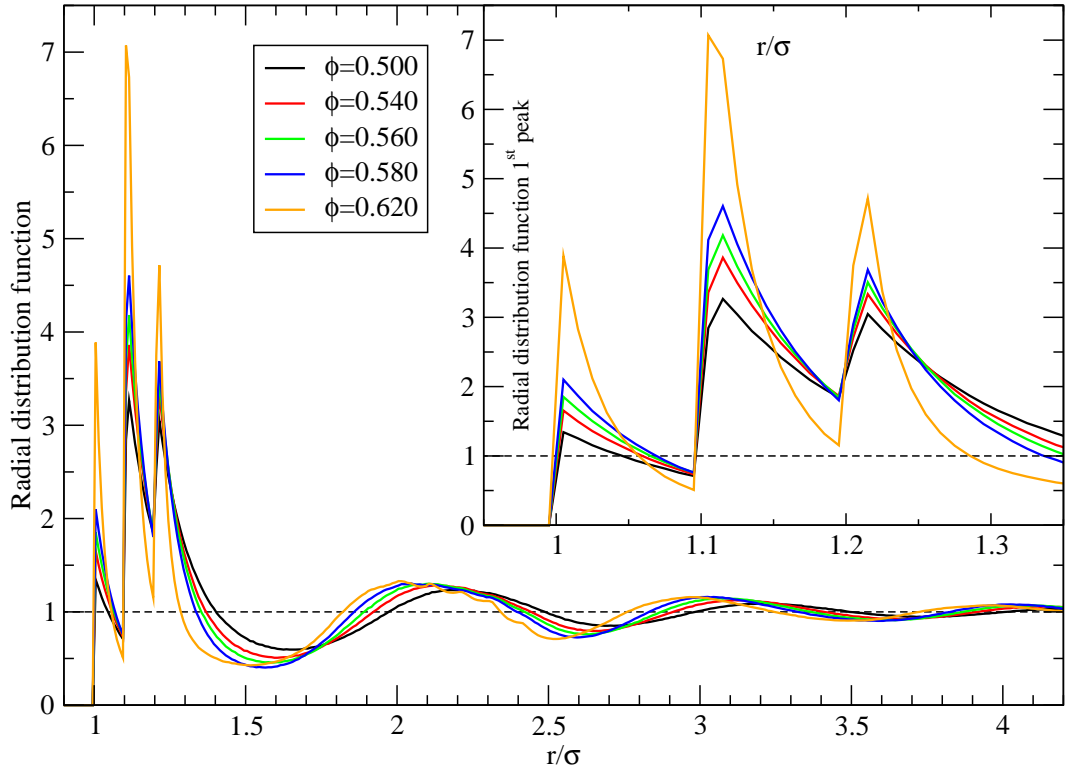


Figure 5.17. Radial distribution function for high densities as indicated. The triptych of the first peak is clearly visible for the binary mixture, as well as the gradual change in local structure as the system progresses to higher densities — in particular, the contact value rises steadily. No long range order is discernible. Shell resolution is $\Delta r = 0.01$. The curves reflect a system after 100 000 time units.

(indicated by the dashed lines in figure 5.16). In general, the binary mixture is less viscous — an effect that is more pronounced the higher the density.

Given the fact that the range of P_e numbers does not stretch as far into the low shear region for the binary case, it is not possible to comment on the emergence of the low shear viscosity plateau, except for densities up to $\phi = 0.52$. What is discernible in this range does, however, confirm the monodisperse picture.

5.6 Towards the glass transition

It is in this chapter that all that we have developed thus far is drawn together to one purpose: In order to reach densities high enough to obtain glass. On the microscopic level, the defining characteristic of such a system is its amorphous structure — that is: it looks like a fluid and has no long range order, despite the fact that its physical properties are rather comparable to that of a solid. In the light of this, it follows naturally that we resort to the standard binary system (section 2.2.1) for this chapter.

The success of this strategy is reflected clearly in figures 5.17 and 5.18, where the local order is strikingly displayed at short range, but disappears completely the further we move to long distances. This is indeed very akin to a fluid that does not show long range order (compare to figure 4.1). The same is true when we approach random close packing with

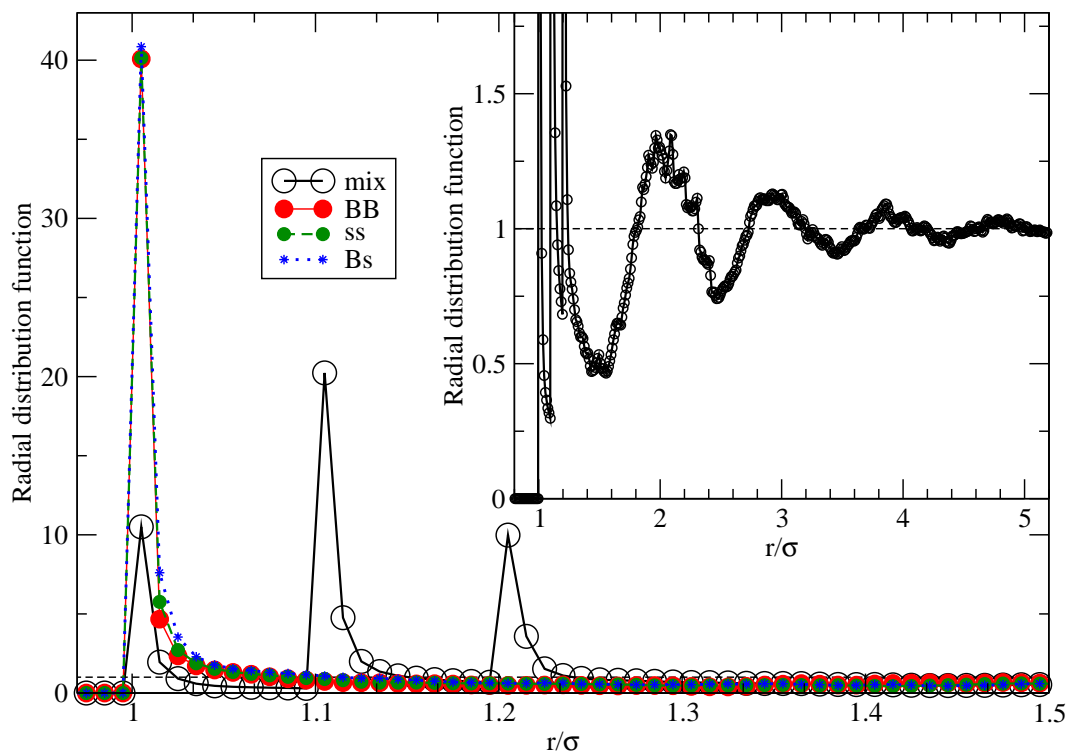


Figure 5.18. Radial distribution function for packing fraction $\phi = 0.640$. Shellwidth and scale is normalised to keep contact at value one. The black curve shows the mixture of any type of colloid. The structure of the second and third neighbour does still exist — even though some enlarging is needed (inset).

$\phi = 0.640$ except that the contact peaks are so large that the structure of the second and third neighbour peaks are relatively invisible. In the inset of figure 5.18 it can be seen that this structure is all but invisible and that even there it decays as the amorphous composition demands. Again we see very clearly the three extremely high contact peaks for the different types of contact: big against big particle (BB), small against small (ss) as well as big in contact with small (Bs). The rise of the first three peaks is directly connected with the approach to random close packing as the number of particles in contact inevitably increases.

The static structure factor (figure 5.19) confirms the amorphous structure but it also betrays another factor that indicates the first hint at the glass transition. For higher densities (orange), the quality of the curve is noticeably worse. Everything else being equal, the average over the same number of sets seems now less effective as for lower densities — more succinctly: the ergodic hypothesis begins to break down. The reduced statistics betray the fact that the system is unable to explore enough of the phase space to deliver a decent crop of independent configurations. In other words: we are in the glass.

We can now turn our attention to the dynamics within the system in order to investigate this inhibition and explore the phase space. The first and obvious place to look is the mean squared displacement (figure 5.20). Again, there is a conspicuous change in the quality of the curves when we reach the packing fraction, $\phi = 0.58$. The set of densities in figure 5.20 can be described as falling roughly into two sets that are generally closer together: the colours black to blue and on the other hand, yellow to magenta. The latter set separates out immediately after the ballistic flight, reflecting the ever decreasing size

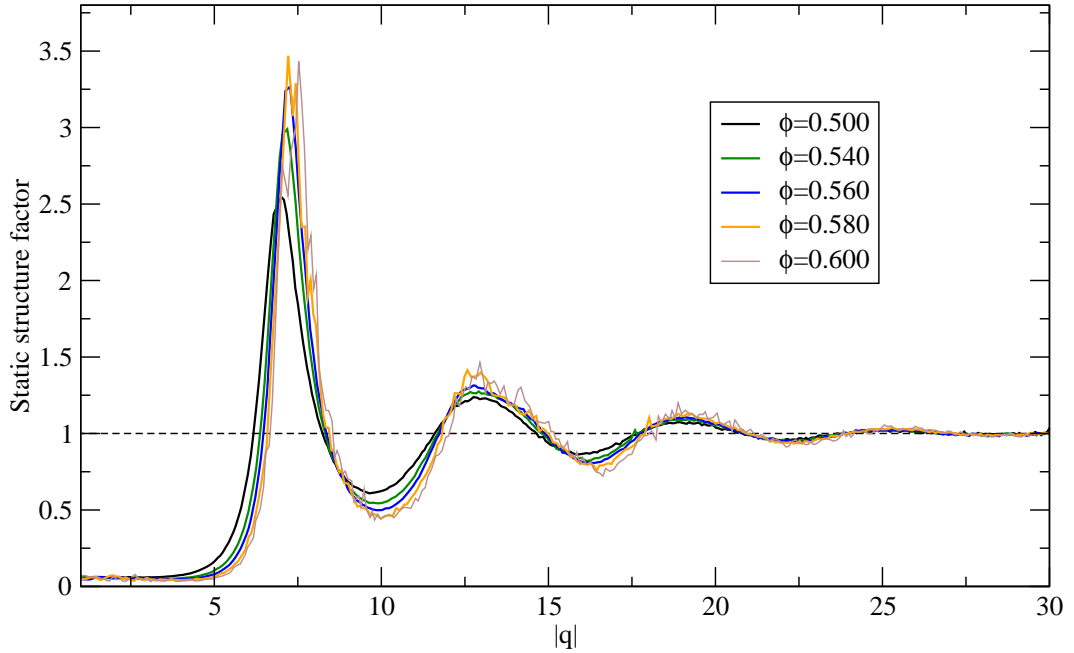


Figure 5.19. The static structure factor at packing fractions around the critical value, $\phi_c = 0.58$, of the glass transition. The loss of statistics betrays the breakdown of the ergodic hypothesis.

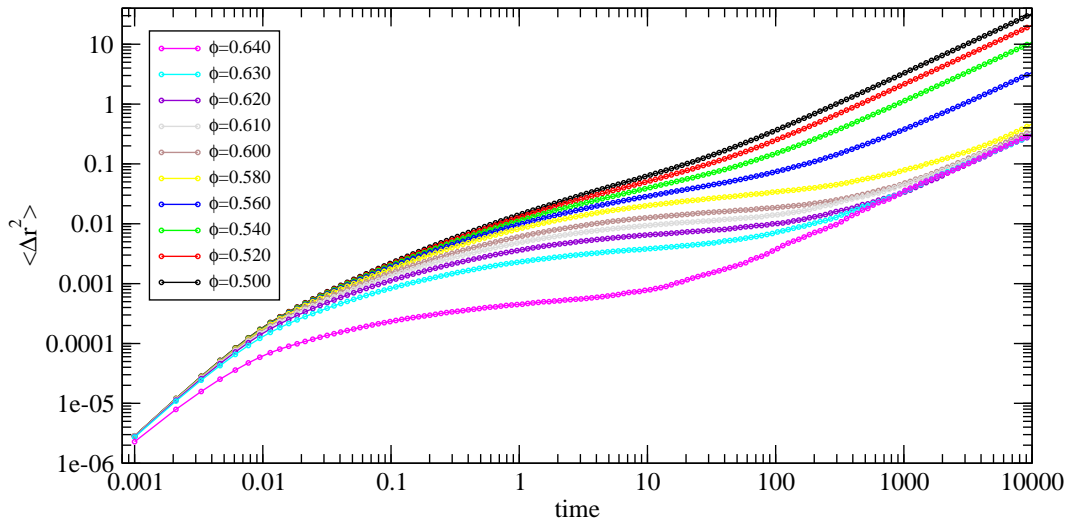


Figure 5.20. Mean squared displacements for a range of high densities. A qualitative difference is visible between $\phi = 0.560$ and $\phi = 0.580$. Even more pronounced is the drop for $\phi = 0.640$ (approaching random close packing).

of the cage. It is this mechanism that may also explain the comparatively large drop in mobility when approaching random close packing — the denser system limits the available space ever more rigorously. The fact that the long time diffusion is nearly equal for all of these systems indicates some process that is common to all of them and that may be related to ageing rather than equilibrium dynamics.

The binary nature of these systems does not lead to a significant difference in mobility for any one of the species. This is shown in figure 5.21 where a separation is only discernible in the region of the cage, suggesting that here the small particle has an advantage due to

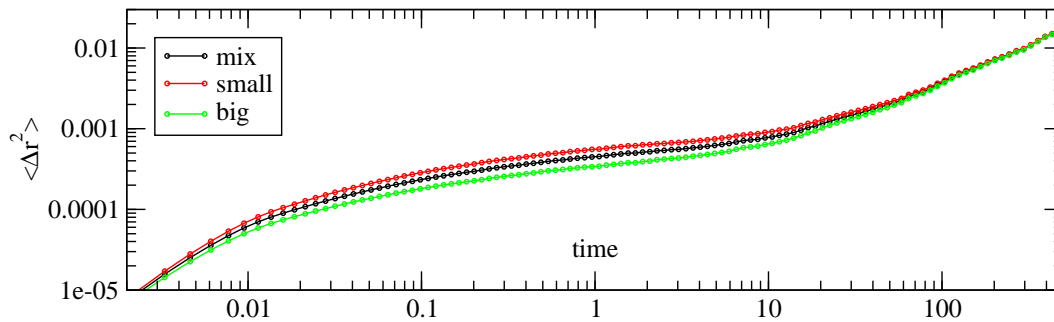


Figure 5.21. Mean squared displacements for $\phi = 0.640$ (approaching close packing) is reached. The mobility has been examined in more detail as all particles (mix) as well as small (red) and big (green) species have been considered separately.

its size. However, as soon the confinement of the neighbours is overcome, no difference in the long time diffusion is visible.

In the remaining pages we will deal with the standard binary system at high densities under shear. The mean squared displacement now shows what is referred to as *Taylor dispersion* in the shear direction. This can be described theoretically [57] by a relation that features essentially a t^3 dependence:

$$\langle (x(t)x(0))^2 \rangle = 2Dt \left[1 + \frac{(t\dot{\gamma})^2}{3} \right]. \quad (5.21)$$

Good agreement of theory and simulation is demonstrated in figures 5.22 and 5.23, where the dashed lines (colours according to shear rate) are the result of equation (5.21). The solid

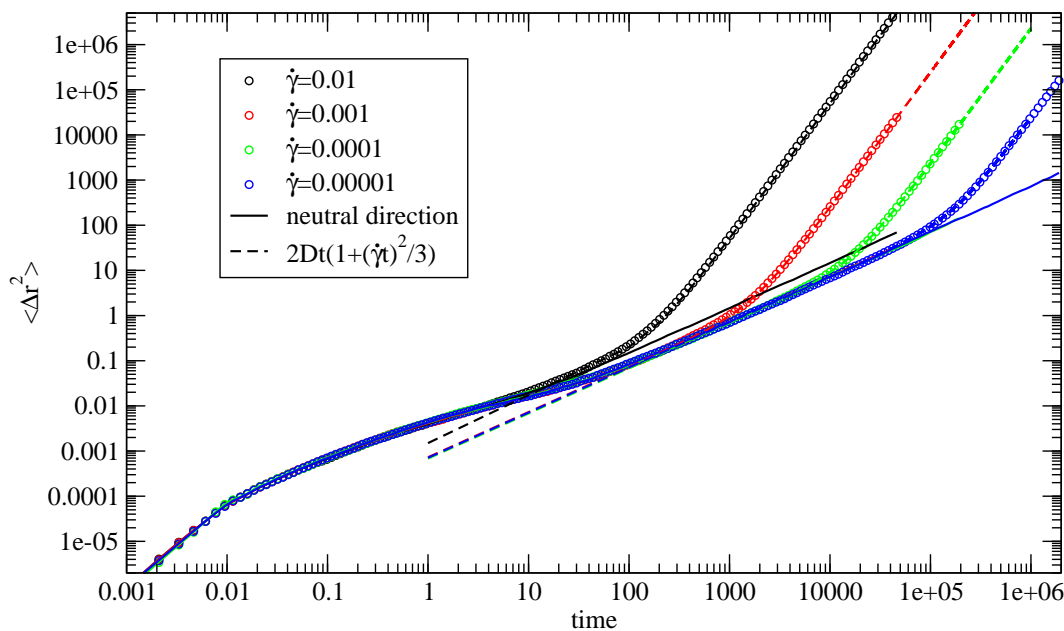


Figure 5.22. Mean squared displacement under shear at $\phi = 0.520$. Here we have split up the displacement according to the directions. The shear direction is in the direction of the flow, while the neutral direction is also parallel to the plates but perpendicular to the flow (as well as the gradient direction). In this last direction all curves collapse. In flow direction Taylor dispersion is observed in accordance with theory.

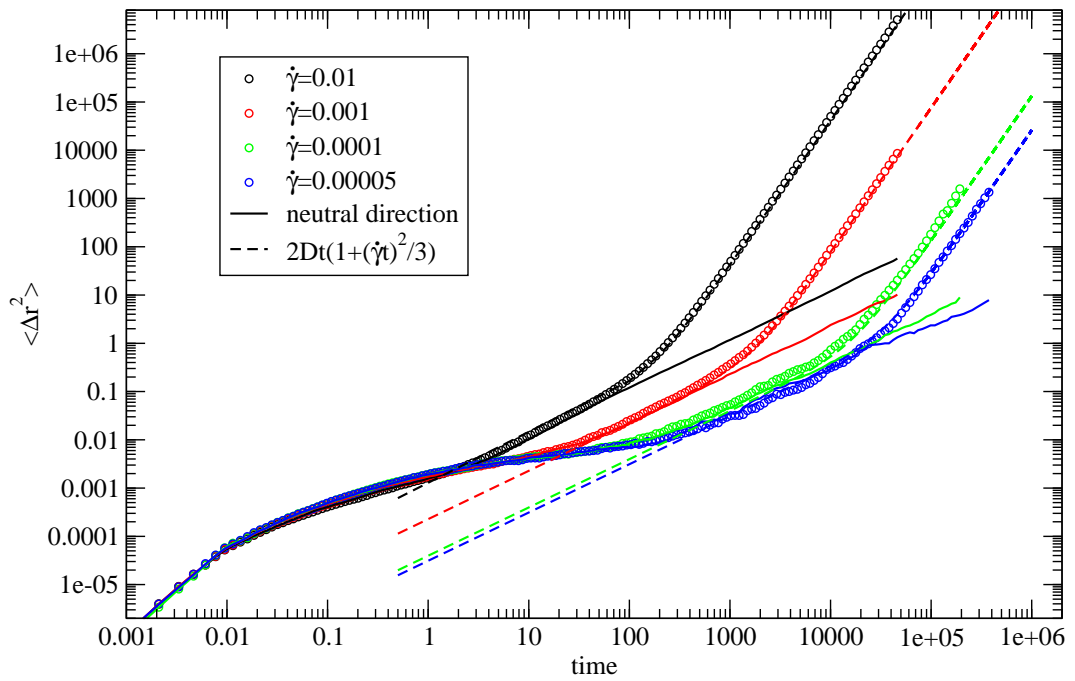


Figure 5.23. Taylor dispersion for systems at the higher packing fraction, $\phi = 0.600$. For the lower shear rates (particularly $\dot{\gamma} = 0.0001$ and $\dot{\gamma} = 0.00005$), there exists a time region between the short and the long time diffusions that may be identified as the cage effect.

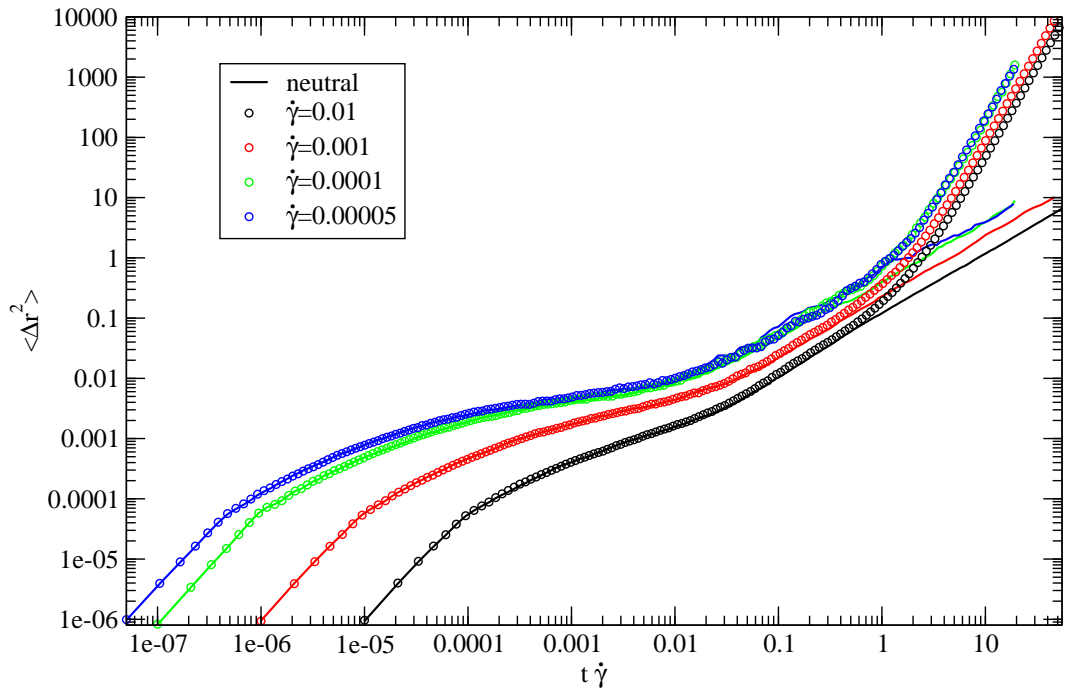


Figure 5.24. Taylor dispersion for a systems at packing fraction, $\phi = 0.600$, with time rescaled and made dimensionless by multiplying with the shear rate, $\dot{\gamma}$. The scaling only brings the lowest shear rates to collapse (dark green and blue).

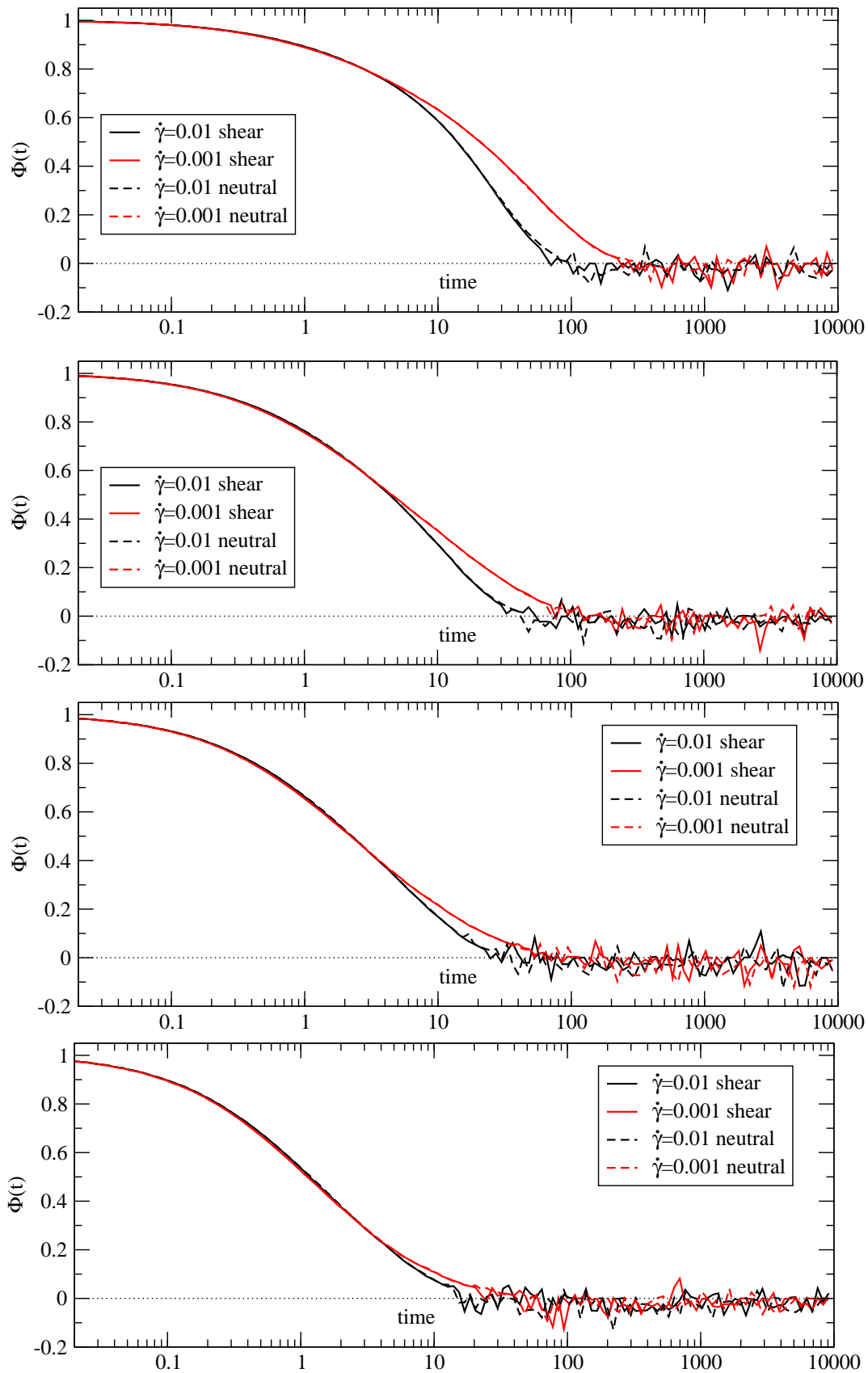


Figure 5.25. Dynamic structure factor for a binary system with a packing fraction of $\phi = 0.52$, shear rates as indicated and wave vectors corresponding to the first two peaks and troughs — $q\sigma = [7.5, 10.2, 12.9, 16.3]$ from top to bottom. Shown are the correlations along the shear direction (solid lines), as well as the neutral direction (dashed lines).

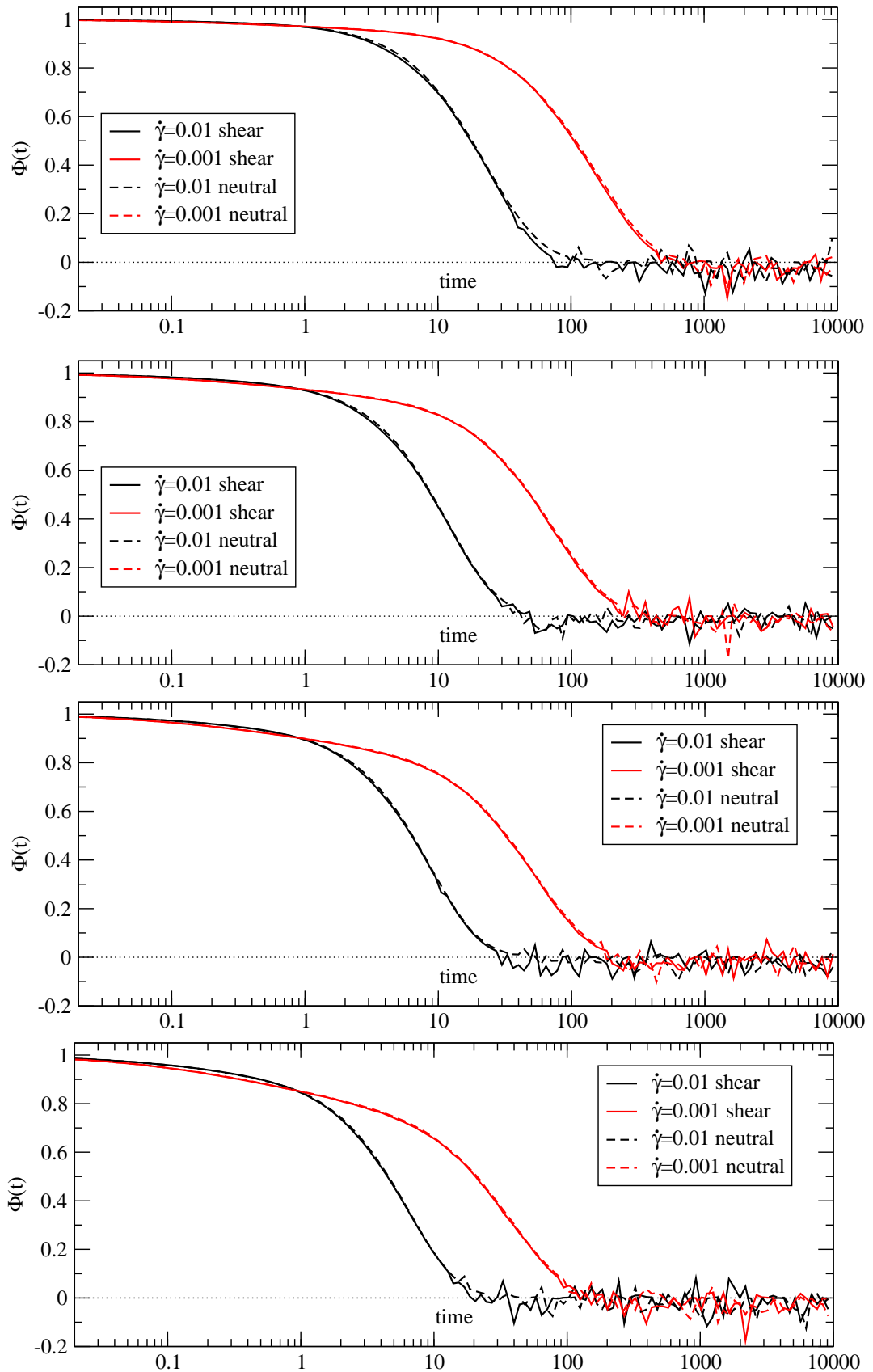


Figure 5.26. At a packing fraction of $\phi = 0.62$, the shear rate has a marked influence on the decay and spreads the final decay out clearly.

lines show the neutral direction in which normal diffusion continues to determine the long time behaviour. Figure 5.23 shows a system at packing fraction, $\phi = 0.60$. Unmistakably a plateau has formed and, in contrast to the system at packing fraction $\phi = 0.52$ in figure 5.22, all shear rates show their own intermediate diffusion before the Taylor diffusion takes off.

We have rescaled the time axis with $\dot{\gamma}$ for the high density at $\phi = 0.60$ in figure 5.24, with the result that only the two smallest shear rates collapse (blue and green), while the curves for $\dot{\gamma} = 0.01$ and $\dot{\gamma} = 0.001$ stay separated. The rationale behind this phenomenon is the assertion that in the glass the diffusion coefficient should become proportional to $\dot{\gamma}$ [22] — with this equation, (5.21) becomes proportional to $\dot{\gamma}t$.

The same should be true for the density density correlation function. However, at $\phi = 0.52$, we are still caught up in the regime of linear response and the shear only mildly contributes to the decorrelation. For figure 5.26, the curves look the part, but the shear rates examined here are high enough to destroy the glass — and with it the scaling.

Even so the influence of shearing is not enough to make the suspension anisotropic. Neither in the fluid phase (figure 5.25) nor at higher densities is the neutral direction distinguishable from the shear direction in $C_{\rho\rho}(\mathbf{q}, t, \dot{\gamma})$. This is also true for the Taylor dispersion where the neutral and shear direction seem to agree up to the very point where the shear does take the particle onto its t^3 -path.

5.7 Open questions

Before we conclude with an inevitably temporary — possibly even preliminary — summary, in the next chapter we would like to list a number of areas where we can see opportunities for further activities.

On a very basic level, that might require changes within the actual programs, there are areas one can always address in the spirit of *faster, higher, stronger*. For our purpose this may be rephrased as *denser* and *longer times*: we may be able to get closer to random close packing under shear, but this would require the combination of swelling and shear. Longer times are not only possible, but also necessary for shear rates smaller than $\dot{\gamma} = 10^{-6}$.

Yet even in the regimes we can currently access there is work left to be done — beyond the mere improvement of admittedly sometimes meagre statistics. The comparison between the integral and distortion method of calculating the viscosities needs to be done at higher densities, where the distorted pair distribution function may be of better quality.

An area begging for further work is the continuation of the simulations around the glass transition. The first task that comes to mind is: verifying the critical density by examining more packing fractions leading up to $\phi = 0.58$. The density correlation functions need to be extended to lower shear rates to be able to test the $\dot{\gamma}$ -scaling. The same can be done for the mean squared displacement at lower shear rates.

And these reflections are but the tip of the iceberg ...

6

Conclusions

Starting from the Langevin equation, we have followed the arguments leading to an algorithm for Brownian dynamics that can reproduce the evolution of the probability density described by the Smoluchowski equation. We have seen that for a sufficiently short Brownian timescale, τ_B , any displacement can be broken down to pair interactions and that the dynamics on this level can be represented faithfully by the algorithm we use. For the opposite limit of τ_B being greater than the entire simulation time, we recover Newtonian dynamics. Building up on this foundation, we have introduced a standard monodisperse system to simulate intermediate densities as well as a particular binary mixture for higher densities.

This proved to be enough to embark on a comparison of the mainly Newtonian dynamics of soft and hard spheres in collaboration with the University of Almeria. We have proposed a scaling of the different systems to the density normalised by the respective freezing point.

Viewed from this perspective, the local structure as well as the pressure still display appreciable differences. On the other hand, our simulations show that the mapping works for the static structure factor, S_q , as well as quantities probing the dynamics of the system — in particular the long time diffusion coefficient D and the stress-stress correlation function $C_{\sigma\sigma}$, including its integral, giving the viscosity η . The simulations confirm an increasingly better match closer to freezing and, as far as the dynamics is concerned, for the limit of long times. This underlines the dominant role the hard core interaction plays in precisely these situations, that is: in the limit of high densities and long times — even for soft spheres.

In the course of this investigation we have introduced the stress tensor for our algorithm. This task is not entirely trivial, not only because of the discontinuous nature of the hard core potential, but also because the algorithm was set up to function on the level of displacements. The forces can therefore only be approximated via a detour through the temperature (kinetic energy) of the system. The results are promising in particular as it was possible to reproduce the short time divergence of the stress correlation function, $C_{\sigma\sigma}$, in Brownian motion as predicted by theory. This corroborates the correct functioning of the dynamics down to the shortest time scales. The same is true for Newtonian dynamics — even though this may be classed as a routine test for the basic algorithm on which Brownian dynamics builds, as the microscopic validity of Newtonian dynamics is, at least in theory, beyond doubt.

With all this in place, the Brownian algorithm has now been adapted to handle shear flow for the first time. This opened up the possibility of calculating the viscosity in a second manner, thus exploiting the distortion of the radial distribution function. We were able to reproduce previously published simulation results on shear viscosity up to the freezing point. Above $\phi = 0.494$, a monodisperse system under shear is prone to crystallisation,

lane formation or any other ordering phenomena, which vindicates our decision to use a binary mixture for these densities. Simulation results for viscosities in the range of densities from $\phi = 0.30$ to $\phi = 0.62$ and Peclet numbers down to $P_e = 0.001$, have been presented for such a system. The viscosity shows a constant value for the limit of low shear rates which coincides with the equilibrium viscosity. As a corollary this meant another test for the method to calculate forces within the system. Agreement is conspicuous.

The simulation with linear shear profiles received further confirmation by reproducing the theoretical results of the Taylor dispersion for a number of densities. Incidentally, it was the mean squared displacement that showed first signs of a glass transition at around $\phi = 0.58$. As a further indication of the emergence of a glass, we take the signature of non ergodicity in the static structure factor. Furthermore, we have produced some preliminary results for the density correlation function at packing fractions of up to $\phi = 0.62$, showing the onset of shear induced decorrelation. The full $\dot{\gamma}$ -dependence has so far only been vindicated by rescaling the timescale of the mean squared displacement at a packing fraction of $\phi = 0.60$, with good agreement for the shear rates below $\dot{\gamma} = 10^{-4}$.

To summarise, the algorithm has been thoroughly tested and performs well under shear and into high densities of up to $\phi = 0.64$. A number of results point towards a glass transition at around $\phi = 0.58$ and it has been confirmed that in the glass shear is the dominant mechanism of relaxation.

6.1 Zusammenfassung in Deutscher Sprache

Mit der Langevin Gleichung als Startpunkt haben wir nachvollzogen, wie sich ein Algorithmus für Brownsche Dynamik erstellen lässt, mit dessen Hilfe die Zeitentwicklung der Wahrscheinlichkeitsdichte gemäß der Smoluchowski-Gleichung beschrieben werden kann. Es kann festgehalten werden, dass auf einer Brownschen Zeitskala τ_B , die klein genug ist, jede Bewegung in paarweise Stöße zerfällt, und dass die Dynamik auf diesem Niveau von dem Algorithmus korrekt abgebildet wird. Für das gegenteilige Extrem, mit τ_B größer als die Simulationszeit, erhalten wir rein Newtonsche Dynamik. Darauf aufbauend haben wir sowohl ein monodisperses Standard-System für mittlere Dichten als auch eine binäre Mischung für höhere Packungsbrüche eingeführt.

Damit hatten wir bereits ausreichend Handwerkszeug, um einen Vergleich zwischen weichen und harten Kugeln in einem gemeinsamen Projekt mit der Universität von Almeria in Angriff zu nehmen. Zu diesem Zweck haben wir eine Skalierung der unterschiedlichen Systeme mittels der auf den Kristallisationspunkt normierten Dichte angewandt. Aus dieser Perspektive präsentiert sich die lokale Struktur sowie auch der Druck als noch immer recht unterschiedlich. Unsere Simulationen zeigen allerdings, dass diese Skalierung in der Tat funktioniert: Für den statischen Strukturfaktor, S_q , und dynamische Größen wie etwa den Diffusionskoeffizienten D oder die Stress-Stress Korrelationsfunktion samt seinem Integral — der Viskosität η . Die Ergebnisse deuten auf eine zunehmend bessere Vergleichbarkeit der Systeme, wenn man sich dem Kristallisationspunkt nähert beziehungsweise für die dynamischen Größen den Limes für lange Zeiten ins Auge fasst. Diese Beobachtung unterstreicht die dominante Rolle der Wechselwirkung der harten Kugeln in just diesen Bereichen der hohen Dichte und des Limes $t \rightarrow \infty$ — sogar für weiche Kugeln.

Im Zuge dieser Untersuchung haben wir auch den Stress Tensor für unseren Algorithmus eingeführt. Diese Aufgabe ist nicht unbedingt trivial, zumal nicht nur der unstete Charakter des Hart-Kugel-Potenzials hier konzeptionelle Probleme bereitet, sondern darüber hinaus auch die Tatsache, dass der verwendete Algorithmus sich im Grunde nur um das Verschieben der einzelnen Teilchen kümmert, ohne auch nur Geschwindigkeiten zu kennen. Die notwendige Impulsänderung konnte daher nur über den Umweg der Temperatur und deren Ausdruck als kinetische Energie annähernd beschrieben werden. Das Ergebnis ist ohne Zweifel ermutigend, besonders weil es damit gelungen ist die Divergenz im Limes $t \rightarrow 0$ der Stress-Korrelations-Funktion samt ihrem Vorfaktor aus der Theorie wiederzugeben. Das ist eine Bestätigung dafür, dass dieser Algorithmus die mikroskopische Dynamik — und in der Tat die Kräfte — bis in kleinste Zeitskalen korrekt widerspiegelt.

Das gleiche gilt auch für die Newtonsche Dynamik. Allerdings bestand hier auch nie ein Zweifel an der — theoretischen — Korrektheit der Vorgehensweise. Mit diesen positiven Signalen im Rücken haben wir den Algorithmus als erste Gruppe so erweitert, dass wir auch Scherung handhaben können. Das hat die Möglichkeit eröffnet die Viskosität auf eine zweite Art zu berechnen, nämlich über die Verzerrung der Paarverteilungsfunktion. Unsere Ergebnisse dazu lassen sich in weiten Teilen mit bereits publizierten Ergebnissen in Deckung bringen. Es ist aber nicht zu übersehen, dass in monodispersen Systemen mit hoher Dichte der Aggregatzustand der Colloide unklar ist. Auch ist für kleine Scherraten eine Zeit der Größenordnung $1/\dot{\gamma}$ notwendig, um einen stationären Zustand zu erreichen. Alles was in der transienten Periode dazwischen geschieht ist unklar — klar ist lediglich, dass es sich nicht mit dem stationären Zustand deckt. Wir können also die monodispersen Ergebnisse bis zur

Dichte des Kristallisationspunktes reproduzieren, alles was darüber liegt legt allerdings den Verdacht nahe, dass sich verschiedene Strukturen im System herausbilden.

Unser Ansatz ist daher, eine binäre Mischung für diese Dichten jenseits des Kristallisationspunktes zu verwenden, die eher geeignet ist derartige Ordnungsphänomene zu unterdrücken. Wir haben Simulationsergebnisse für ein solches System für Packungsbrüche von $\phi = 0.30$ bis $\phi = 0.62$ und Peclet-Zahlen bis hinab zu $P_e = 0.001$ vorgelegt, die das Bild qualitativ bestätigen. Bei niedrigen Dichten ist für niedrige Scherraten recht früh ein konstanter Grenzwert erkennbar, für höhere Dichten fehlen bislang die Daten bei weit niedrigeren Scherraten.

Als Nebeneffekt konnten die Integralmethode, die die Viskosität aus den Kräften berechnet einem weiteren Test unterzogen werden indem sie mit der Viskosität aus der verzerrten Paarverteilungsfunktion verglichen wurde. Bei Packungsbruch $\phi = 0.494$ (Kristallisation) ist die Übereinstimmung im Rahmen des Fehlers durchaus erkennbar.

Eine weitere Bestätigung für den Algorithmus unter Scherung ergab sich durch die Wiedergabe der theoretischen Ergebnisse zum mittleren Verschiebungsquadrat, insbesondere der Taylor-Dispersion bei unterschiedlichen Dichten. Dabei zeigten sich auch die ersten Hinweise, die ein Glas um den Packungsbruch $\phi = 0.58$ andeuteten. Ein weiteres Indiz dafür ist im statischen Strukturfaktor zu erkennen, dessen Kurve bei genau dieser Dichte den Zusammenbruch der Ergodizitätsannahme andeutet. Bei einer Packungsdichte von $\phi = 0.60$ konnte darüberhinaus festgestellt werden, dass bei sehr niedrigen Scherraten die Ergebnisse mit $\dot{\gamma}$ skalieren. Zusammenfassend kann gesagt werden, dass der Algorithmus gründlich und mit positivem Ergebnis für Scherung und Dichten bis $\phi = 0.64$ getestet wurde. Eine Reihe von Ergebnissen deutet den Glasübergang bei einem Packungsbruch um $\phi = 0.58$ an, wo auch eine Bestätigung dafür gefunden werden konnte, dass im Glas der dominante Mechanismus für den Zerfall des Dichte-Dichte Korrelators die Scherung ist.

Bibliography

- [1] B.J. ACKERSON: *Journal of Rheology*, **34**, 553 (1990).
- [2] R. AGRAWAL and D.A. KOFKE: *Phys. Rev. Lett.*, **74**, 122 (1995).
- [3] R. AGRAWAL and D.A. KOFKE: *Molecular Physics*, **85**, 23 (1995).
- [4] B.J. ALDER, D.M. GASS and T.E. WAINWRIGHT: *Journal of Chemical Physics*, **53**, 3813 (1970).
- [5] B.J. ALDER and T.E. WAINWRIGHT: *The Journal of Chemical Physics*, **27**, 1208 (1957).
- [6] H.C. ANDERSEN, J.D. WEEKS and D. CHANDLER: *Phys. Rev. A*, **4**, 1597 (1971).
- [7] J.P. BOON and S. YIP: *Molecular hydrodynamics* (McGraw-Hill, 1980).
- [8] A.C. BRANKA and D.M. HEYES: *Phys. Rev. E*, **69**, 021202 (2004).
- [9] R. BROWN: *Edinburgh New Philosophical Journal*, **July-September 1828**, 358 (1828).
- [10] G. BRYANT, S.R. WILLIAMS, L. QIAN, I.K. SNOOK, E. PEREZ and F. PINCET: *Physical Review E*, **66**, 060501 (2002).
- [11] M.D. CARBAJAL-TINOCO: *The Journal of Chemical Physics*, **128**, 184507 (2008).
- [12] N.F. CARNAHAN and K.E. STARLING: *Journal of Chemical Physics*, **51**, 635 (1969).
- [13] S. CHANDRASEKHAR: *Reviews of Modern Physics*, **15**, 1 (1943).
- [14] B. CICHOCKI and K. HINSEN: *Physica A: Statistical and Theoretical Physics*, **166**, 473 (1990).
- [15] J.K.G. DHONT: *An introduction to the dynamics of colloids* (Elsevier, 1996).
- [16] J.W. DUFTY: *Molecular Physics*, **100**, 2331 (2002).
- [17] A. EINSTEIN: *Annalen der Physik*, **17**, 549 (1905).
- [18] A. EINSTEIN: *Annalen der Physik*, **324**, 289 (1906).
- [19] A. EINSTEIN: *Annalen der Physik*, **339**, 591 (1911).

- [20] G. FOFFI, W. GÖTZE, F. SCIORTINO, P. TARTAGLIA and T. VOIGTMANN: *Physical Review Letters*, **91**, 085701 (2003).
- [21] D.R. FOSS and JOHN F. BRADY: *Journal of Rheology*, **44**, 629 (2000).
- [22] M. FUCHS and M.E. CATES: *Physical Review Letters*, **89**, 248304 (2002).
- [23] M. FUCHS and M.E. CATES: *Faraday Discussions*, **123**, 267 (2003).
- [24] J.-P. HANSEN and L. VERLET: *Phys. Rev.*, **184**, 151 (1969).
- [25] J.P. HANSEN and I.R. MCDONALD: *Theory of simple liquids* (Academic Press, 1986).
- [26] D.M. HEYES: *The Journal of Chemical Physics*, **107**, 1963 (1997).
- [27] D.M. HEYES and P.J. ASTON: *The Journal of Chemical Physics*, **100**, 2149 (1994).
- [28] D.M. HEYES and A.C. BRANKA: *The Journal of Chemical Physics*, **122**, 234504 (2005).
- [29] D.M. HEYES and J.R. MELROSE: *Journal of Non-Newtonian Fluid Mechanics*, **46**, 1 (1993).
- [30] J.H. IRVING and J.G. KIRKWOOD: *The Journal of Chemical Physics*, **18**, 817 (1950).
- [31] A. KASPER, E. BARTSCH and H. SILLESCU: *Langmuir*, **14**, 5004 (1998).
- [32] Y. KATAYAMA and R. TERAUTI: *European Journal of Physics*, **17**, 136 (1996).
- [33] E. LANGE, J.B. CABALLERO, A.M. PUERTAS and M. FUCHS: *The Journal of Chemical Physics*, **130**, 174903 (2009).
- [34] P. LANGEVIN: *C. R. Acad. Sci. (Paris)*, **146**, 530 (1906).
- [35] R.A. LIONBERGER and W.B. RUSSEL: *Journal of Rheology*, **38**, 1885 (1994).
- [36] H. LÖWEN, T. PALBERG and R. SIMON: *Phys. Rev. Lett.*, **70**, 1557 (1993).
- [37] G. NAGELE and J. BERGENHOLTZ: *Journal of Chemical Physics*, **108**, 9893 (1998).
- [38] W. PAUL and D.Y. YOON: *Phys. Rev. E*, **52**, 2076 (1995).
- [39] R. PIAZZA, T. BELLINI and V. DEGIORGIO: *Phys. Rev. Lett.*, **71**, 4267 (1993).
- [40] J.G. POWLES and D.M. HEYES: *Molecular Physics*, **98**, 917 (2000).
- [41] W.H. PRESS, S.A. TEUKOLSKY, W.T. VETTERLING and B.P. FLANNERY: *Numerical recipes in C++* (Cambridge University Press, 2002).
- [42] P.N. PUSEY and W. VAN MEGEN: *Nature*, **320**, 340 (1986).
- [43] D.C. RAPAPORT: *The art of molecular dynamics simulations* (Cambridge University Press, 1995).
- [44] H. REISS and A.D. HAMMERICH: *Journal of Physical Chemistry*, **90**, 6252 (1986).

- [45] M.D. RINTOUL and S. TORQUATO: Phys. Rev. Lett., **77**, 4198 (1996).
- [46] F.J. ROGERS and D.A. YOUNG: Physical Review A, **30**, 999 (1984).
- [47] Y. ROSENFELD: Phys. Rev. A, **24**, 2805 (1981).
- [48] A. SCALA, T. VOIGTMANN and C. DE MICHELE: The Journal of Chemical Physics, **126**, 134109 (2007).
- [49] I.M. SCHEPPER, H.E. SMORENBURG and E.G.D. COHEN: Physical Review Letters, **70**, 2178 (1993).
- [50] H. SENFF and W. RICHTERING: The Journal of Chemical Physics, **111**, 1705 (1999).
- [51] M. VON SMOLUCHOWSKI: Annalen der Physik, **326**, 756 (1906).
- [52] P. STRATING: Physical Review E, **59**, 2175 (1999).
- [53] J.C. VAN DER WERFF, C.G. DE KRUIF, C. BLOM and J. MELLEMA: Phys. Rev. A, **39**, 795 (1989).
- [54] N.G. VAN KAMPEN: *Stochastic processes in physics and chemistry* (Elsevier, 2006).
- [55] R. VERBERG, I.M. DE SCHEPPER and E.G.D. COHEN: Phys. Rev. E, **55**, 3143 (1997).
- [56] M. WATZLAWEK, C.N. LIKOS and H. LÖWEN: Phys. Rev. Lett., **82**, 5289 (1999).
- [57] R. YAMAMOTO and A. ONUKI: Phys. Rev. E, **58**, 3515 (1998).